Catalytic Properties of Nano Ceria in Heterogeneous Catalysis

Jiahui Xu

Linacre College, University of Oxford

A thesis submitted for the degree of Doctor of Philosophy

Inorganic Chemistry Laboratory
University of Oxford

October 2010

Outline

Contents		i
Declaration		ii
Acknowledgements		iii
Abstract		v
Abbreviations		vi
Chapter 1	Introduction	1
Chapter 2	Experimental	48
Chapter 3	Ceria Coated Commercial Ni Catalysts: Methane Steam Reforming for Hydrogen Production Using Low Water/Methane Ratios without Carbon Formation	89
Chapter 4	Size Dependent Oxygen Storage Capacity of Ceria Nanocrystals	124
Chapter 5	The Enhancement for the Oxygen Storage Capacity of Ceria by Metal	163
Chapter 6	Conclusion	200

Declaration

I confirm that this is wholly my own work unless otherwise stated and acknowledged in the thesis.

Jiahui Xu

Acknowledgements

I would first like to thank Professor Tsang for giving me the opportunity to come and study at UK and for all his supervision, encouragement and financial support over the past four years.

Secondly, I would like to extend my gratitude to all the members of the Tsang group, past and present, who have provided much help and support. I would like to thank Dr. Connie Yeung and Dr. Kerry Yu for their expert supervisions in the laboratory. I would specially thanks to Dr. Kerry Yu, Dr. Nadia Acerbi, Dr. Karaked Tedsree and Mr. Thomas Chapman for all the hard work done in the reading proof of this thesis. I will be forever indebted to their painstaking patience, and above all kindness without which it would have been impossible to finish this thesis. Thanks to the rest of the Tsang group, especially, Dr. Adam Kong, Dr. Asun Hurtado, Dr. William Oduro, Dr. Nick Caiulo, Dr. Igor Curcic, Ms. Lin Qiu, Ms Kasia Morawa, and all of whom have helped me along the way, for their support both at the work and in my personal life for these four years.

Also I am very grateful to Dr. Jeffrey Harmer for his help in the electronic paramagnetic resonance (EPR) experiments, Dr. Peter Harris (University of Reading) for his help in Electron Microscopy (TEM, SEM and EDX), Dr. Guoqiang Li and Ms. Fang Li for their work concerning TEM and SAED, Dr. Frederic Meunier and Dr. Jun Ni (Queen's University

Belfast) for collecting DRIFTS data, Dr. Paul Collier and Dr. Sarennah Longworth (Johnson Matthey Catalysts) for their work in XPS, Dr. Christoph Salzmann for Raman training, Dr. Phil Wiseman for XRD training and Dr. Karaked Tedsree for the discussion in FTIR work.

Special thanks to my friends Yuan Liu, Yi Du, Yan Ma, Yitong Li, Qing Shen, Binbin Zhou, Fang Li, Lei Li, Shasha Liu, Shunying Liu, Lili Tian, Hao Wang and Yige Zhou, who have spent a wonderful time with me in UK and given me strong support when my grandmother and father passed away. Thanks to my college advisor Dr. Timothy Vaden and my college mentor Laura Richard who have offered the encouragement, support and confidence.

Finally, a huge thank you goes to my mother for her constant and unwavering support, encouragement and love.

Abstract

There have been many applications of cerium oxide in oxidation catalysis but the understanding of its role in catalysis is rather limited. This research is concerned with the use of nano-size cerium oxide in methane steam reforming reaction. It is found that addition of cerium oxide to the commercial supported Ni catalysts can dramatically reduce the undesirable carbon deposition (through surface oxidation), which is thermodynamically favorable under low steam conditions. In order to understanding the fundamental role of oxidation activity of the cerium oxide, different sizes of nano-crystallined cerium oxides have been carefully prepared by micro-emulsion technique. Their reactivity is clearly shown to be size dependent. We found that ceria particle sizes of lower than 5.1 nm are able to activate molecular oxygen, which accounts for the unprecedentedly reported critical size effect on oxidation. Characterizations by EPR, XPS, TPR suggest that a substantially large quantity of adsorbed oxygen species (O_2^-) is preferentially formed in the small size ceria from air. Also, it is found that the oxygen vacancies are formed in the interface of metal and oxide, and the strength of the metal oxide interaction may influence the formation of the efficient oxygen vacancies, which are responsible for the adsorbed surface oxygen.

Abbreviations

CMP	Chemical Mechanical Planarization
DP	Deposition Precipitation
DRIFTS	Diffuse Reflectance Fourier-Transform Spectroscopy
EDX	Energy Dispersive X-ray Spectroscopy
EG	Ethylene Glycol
EPR	Electronic Paramagnetic Resonance
FID	Flame Ionization Detector
FTIR	Fourier Transform Infrared Spectroscopy
FWHM	Full Width at the Half Maximum
GC	Gas Chromatograph
GHSV	Gas Hourly Space Velocity
GTL	Gas To Liquid
MSR	Methane Steam Reforming
OSC	Oxygen Storage Capacity
PD	Propanediol

SAED	Selected Area Electron Diffraction
SC	Solar Cells
SEM	Scanning Electron Microscopy
SOFC	Solid Oxide Fuel Cell
STM	Scanning Tunneling Microscopy
TCD	Thermal Conductivity Detector
TEM	Transmission Electron Microscopy
TGA	Thermo-Gravimetric Analyzer
TOF	Turnover Frequency
TPR	Temperature Programmed Reduction
TWC	Three-Way Catalysts
WGS	Water Gas Shift
XRD	X-ray Diffraction
XPS	X-ray Photoelectron Spectroscopy
YSZ	Yttria-Stabilized Zirconia

CHAPTER ONE

INTRODUCTION

1.1 Ceria 3

1.1.1 Mining and Production 4

1.1.2 Technical Applications 5

1.1.3 Synthesis Methods 8

1.1.4 Structural Properties 14

1.1.5 Oxygen Storage Capacity 23

1.2 Heterogeneous Catalysis 31

1.2.1 Definition and Kinetics 31

1.2.2 Active Sites 33

1.2.3 Deactivation 34

1.2.4 Encapsulated Metal Catalysts 35

1.3 Scope of Thesis 38

1.3.1 Objectives 38

1.3.2 Outline of Project Achievements 39

1.4 References 40

1.1 Ceria

Ceria, or CeO_2, is ranked as one of the most important rare earth metal oxides used in industry [1]. There are a increasing number of applications being discovered for the utilization of ceria as a promoter for many catalysts to improve activity, selectivity, and thermal stability, as well as its wide ranging use as a bulk and commodity catalyst, and as fuel cell electrodes and photocatalysts, which have resulted in a sharp increase in interest in this metal oxide. Figure 1.1 shows the rapid growth in reports of ceria containing materials in the past several years.

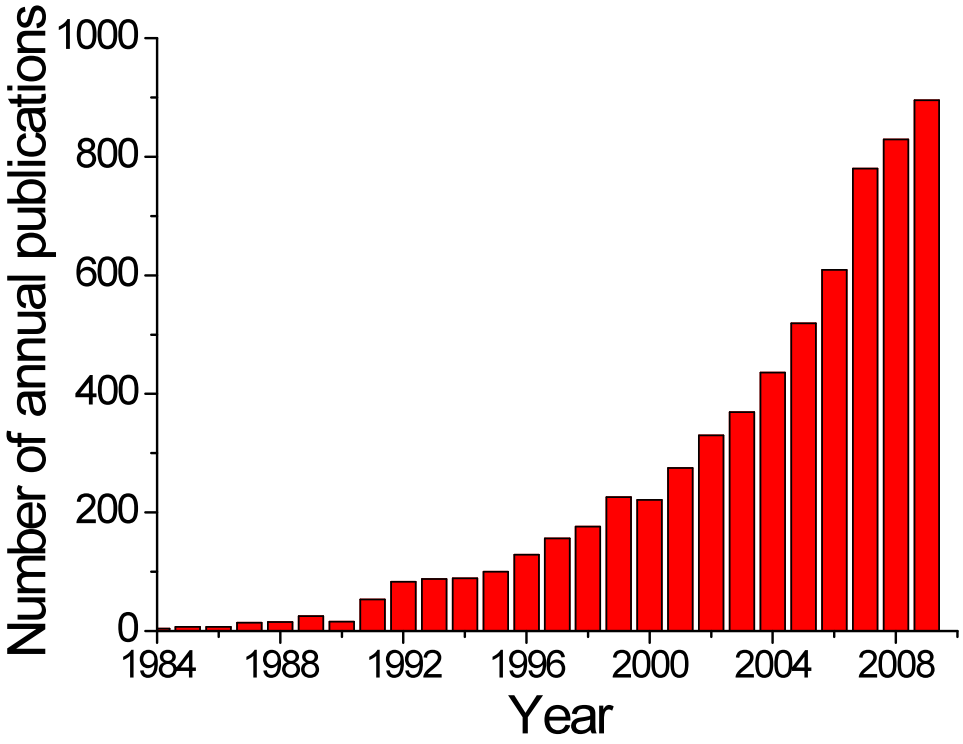

Figure 1.1 The number of articles which contained the keyword "ceria" on the topic from *Web of Knowledge*.

1.1.1 Mining and Production

Cerium accounts for around 0.0046% of the earth's crust. It is found naturally as minerals, including monazite, allanite and bastnasite, alongside other rare elements. The identification and separation of these rare earth elements has proved to be very troublesome, due to their very similar chemical properties [1]. The current separation procedure involves dissolving the above mineral sources in sulfuric acid, and then neutralizing this solution with sodium hydroxide to the point at which the thorium precipitates out as hydroxide. Once the radioactive thorium has been excluded, further reaction with ammonium oxalate produces the rare earth oxalates which can be easily annealed to the oxides. The ceria can be separated from the remainder of the rare earth oxides by being washed with nitric acid due to the insolubility of the nitrate.

Commercial cerium is normally produced by solvent extraction, selective precipitation and ion exchange. The cerium is isolated usually by precipitation as an oxalate, carbonate or hydroxide, which are considered to be the most important precursors for cerium derivatives on a commercial scale. After additional chemical and/or physical treatment, the cerium derivatives are yielded from these compounds, and bulk cerium oxide is, for instance, easily formed by calcining cerium carbonate and/or cerium oxalate.

1.1.2 Technical Applications

Ceria is widely used in areas such as catalysis and chemicals, glass and ceramics, phosphors and metallurgy [1-9]. The applications of ceria related materials are based on a potential redox chemistry involving Ce^{3+} and Ce^{4+}, at high affinity of the element for oxygen and sulf, and adsorption/excitation energy bands associated with its electronic structure.

1.1.2.1 Environmental Catalysis

A major technological application of ceria which is steadily growing in importance is in automobile emissions control. Government regulations continue to lower the acceptable emissions levels of carbon monoxide, hydrocarbons and nitrogen oxides in automotive exhaust fumes. Automotive catalytic converters are a key focus area for examination of catalyst performance. Companies are attempting to reduce the use of precious metals, such as platinum, palladium and rhodium in the catalytic converter to lower costs while meeting increasingly stringent performance standards. One way to achieve lower emissions in a cost effect manner is to utilize co-catalysts to provide good oxygen storage capacity and thermal stability in thinner layers. In terms of this issue, the most important application of ceria in economic and technological terms is its use is as a key “oxygen storage” component in three-way catalysts (TWCs), which accounts for a large part (around one quarter) of the global catalyst market [2], to treat the exhaust gas from automobiles, where ceria contained catalysts are used in the exhaust system to remove the pollutants (mainly NO, CO and hydrocarbons)

simultaneously [1]. For example, the Toyota Motor Corp. has put cerium-zirconium oxide containing automotive TWCs into practical use globally [3].

The control of sulf oxide emissions is becoming increasingly important. Several catalyst additives containing ceria can act as a sulf oxide control agent [4]. Also, ceria containing materials have been applied to the treatment of wastewater which is discharged by the chemical industry. It is through the wet oxidation progress which is carried out under high pressure of oxygen at elevated temperatures to decompose organic pollutants in wastewater, and ceria containing materials are used as catalysts [1].

1.1.2.2 Semiconductor Polishing

As the semiconductor industry continues to progress towards using smaller chip architecture, the need for advanced chemical mechanical planarization (CMP) slurries becomes a requirement that cannot be met by the slurries that already exist. For large-scale, wafer-level fabrication of nanodevices and their integration with silicon technology, the surface of a wafer needs to be perfectly flat and free from defects. Ceria nanoparticles are a key abrasive nanomaterial for the chemical mechanical planarization (CMP) of advanced integrated circuits in what is now a multi-billion dollar market [5].

1.1.2.3 Fuel Cell

Solid oxide fuel cells (SOFCs) have attracted considerable research interest because they offer many advantages as energy conversion devices. Conventional

SOFCs, which use yttria-stabilized zirconia (YSZ) as the electrolytes, are operated at around 1000 ^{o}C. However, this operating temperature presents some disadvantages for commercialization, for example, the long-term stability of the cell and component materials and manufacturing costs. Thus, reduction of the operating temperature for SOFCs may be able to lead to many advantages such as reduced costs, and less time and energy being necessary for start up processes. Undoped and doped ceria exhibit high conductivity at low partial oxygen pressures due to the formation of small polarons (which may come from defects such as oxygen vacancies). Ceria is attracting increasing amounts of interest as a component for SOFC materials at intermediate temperatures (500 – 800 ^{o}C) and these materials show higher conductivity than the conventional SOFC YSZ electrolyte [6].

1.1.2.4 Other Applications

Ceria also participates in new catalysts formulations for water-gas-shift (WGS) reactions [7], hydrocarbon reforming [8] and hydrocarbon oxidation [9]. Within the applications mentioned above, the oxygen storage capacity (OSC) of ceria (oxygen non-stoichiometry) plays an important role. This capacity is directly related to the number of oxygen vacancies from the cycles between Ce^{3+} and Ce^{4+} of the ceria and will be discussed later.

1.1.3 Synthesis Methods

Ceria particles have been synthesized in a range of different sizes, shapes and structures. Most of the dimensional changes of cerium oxides can now be controlled using various synthetic methods. Many techniques have been reported for the efficient production of ceria, such as aerosol pyrolysis [10], the sonication accelerated chemical method [11], homogeneous precipitation [12], thermal decomposition [13], mechanochemical processing [14], the microwave-assisted hydrothermal route [15], and many other methods [16-20]. Here sol-gel and microemulsion, which will be used as the major synthetic methods of this thesis, will be introduced. Both these methods are extensively used to generate ceria nanoparticles due to their fine structure control during the synthesis process.

1.1.3.1 Microemulsion Method

The microemulsion is one of the most powerful methods for obtaining ultrafine nanoparticles. This method is based on the use of reversed micelles as small reactors. The microemulsion is composed of two immiscible liquids (aqueous solution and organic oil) and a surfactant. In water-in-oil microemulsions, nanodroplets of an aqueous phase within the reversed micelles are dispersed in an oil phase. In this method, particles of a defined shape and nano meter size can be prepared in the micelle.

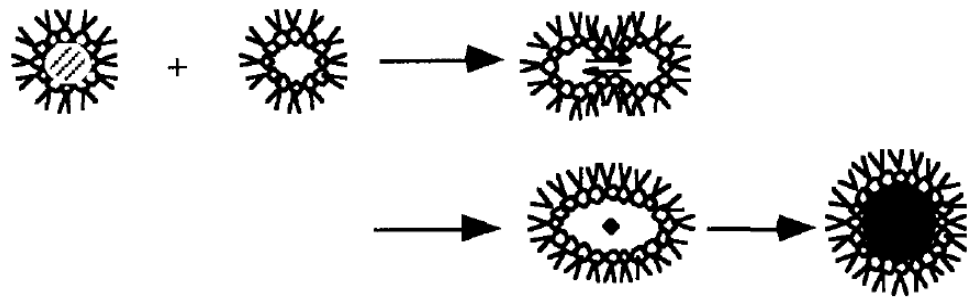

Scheme 1.1. The mechanism for the formation of particles by the microemulsion method [21].

Scheme 1.1 shows a schematic picture of this process. After mixing two microemulsions containing the reactants, the interchange of reactants is carried out during the collision of the nanodroplets in the microemulsions. This interchanging process is very fast and the final size of particles is controlled by the droplet size. Once the particles attain their final size, the surfactant molecules protect against further growth of the particle. The size of the droplets can be controlled normally in the range of 5 - 50nm by varying the microemulsion system itself [21].

In 1997 Masui et al. [22] were the first to report the synthesis of nanometre-sized ceria ultrafine particles prepared by the microemulsion method with a fairly narrow size distribution. The size of the particles was controlled within the vital range under 5 nm and the smallest mean size of ceria was 2.6 nm – the smallest cerium oxide reported since this paper was published. The synthesis of nanosized CeO_2-ZrO_2 was reported later by the same group using the similar method [23], when the amorphous as-prepared ultrafine nanoparticles were obtained. In 1999, Martinez-Arias et al. reported the use of a similar method to synthesize a CeO_2-ZrO_2 mixed oxide [24] with a high surface area (near 100 m^2 g^{-1}). Several factors of the synthesis can affect the morphology and size distribution of the synthesized particles. For example, the type

and the amount of the surfactant, as well as the concentration of reactants all have an effect upon results.

1.1.3.2 Sol-gel Method

The sol-gel method is an important technique that can be used to synthesize many materials in a variety of shapes and forms. This method is especially suited to the synthesis and preparation of ultrafine oxide catalysts at relatively low temperatures. These factors, which may affect the number and properties of the active sites and the reaction kinetics of catalysts, that can be controlled by the sol-gel method, include: (1) high specific surface; (2) controlled pore size distribution; (3) textural stability under the preparation and reaction conditions; (4) an active phase which is at the surface, and not homogeneously distributed into the solid; (5) good and homogeneous dispersion; (6) controlled structural properties; (7) high purity of the catalyst components; (8) easily controlled composition in the preparation of multicomponent catalysts; (9) mechanical properties that accomplish the requirements of the operation conditions; and (10) catalysts that are active for as long as possible without severe deactivation due to chemical or physical blocking of active sites [25].

A sol is a stable colloidal dispersion of small particles suspended in a liquid. The particles are amorphous or crystalline and the particle aggregation is prevented by electrostatic repulsion. The particles in some sols interact to form a continuous network of connected particles called a gel, instead of aggregating to form larger particles. Drying a gel simply by evaporating the interstitial liquid gives rise to capillary forces causing the gel to shrink and causing the formation of cracks as result of the differential stresses generated in the drying gel. The resulting dried gel is

known as a xerogel. When the wet gel is dried under supercritical conditions, the pore and network structure of the gel is maintained even after drying. The resulting gel is called aerogel in this case. These sol-gel materials are frequently applied to the synthesis of catalysts and catalyst supports because they have a large surface area.

A method of producing the sol is to hydrolyze reactive metal compounds, for example, alkoxides, $M(OR)_n$, where M is a metal (e.g. Ce and other rare earths, Al, Ti, Zr, etc.) and R is an alkyl group (e.g. methyl, CH_3, ethyl, C_2H_5, or propyl, C_3H_7). In the sol-gel method, metal alkoxides are generally dissolved in an alcohol (such as methanol, ethanol, or iso-propanol) and the addition of water causes hydrolysis of metal alkoxides.

$$M(OR)_n + n\ H_2O \rightarrow M(OH)_n + n\ ROH \qquad (1.1)$$

This is followed by a series of condensation reactions between hydroxide groups and the overall reaction is represented by the following chemical equation:

$$M(OH)_n \rightarrow MO_{n/2} + n/2\ H_2O \qquad (1.2)$$

It can be seen that this method allows mixed oxide gels to be produced readily by the mixing of their alkoxides solutions prior to hydrolysis.

In 1988, Imoto et al. reported that the cerium oxide with the particle size 4 -5.5 nm was obtained from the cerium chloride in isopropanol with the addition of metallic sodium to form cerium isopropoxide following by dryness and subsequent calcination [26]. More work on the synthesis of CeO_2-ZrO_2 [27] and CeO_2-TiO_2 [28] particles using similar methods has also been reported. For the preparation of ceria-based

oxides, cerium isopropoxide, cerium acetylacetonate, cerium nitrate are used as the precursors. The water necessary for these hydrolysis reactions is either added directly or introduced by means of the hydrated cerium nitrate.

Because the reaction rate of the hydrolysis-condensation based sol-gel method is too fast to control, the non-hydrolytic sol-gel process is used to synthesize various oxides materials [29]. In 2005, Yu et al. reported a large-scale synthesis of uniform sized ceria nano crystals with spherical, wire and tadpole shapes by the non-hydrolytic sol-gel reaction of cerium (III) nitrate and diphenylether in the presence of appropriate surfactants [30]. The ceria nanocrystals were produced on a scale of more than 10 g in a single reaction and the ceria nanowires with an ultra small diameter of 1.2 nm were synthesized.

1.1.3.3 Other Methods

Due to the remarkable size-dependent properties and the technological applications of nano ceria, the synthesis of ultra fine nano ceria has been intensively studied in recent years. Inoue et al. obtained a colloidal solution of 2 nm by solvothermal process [31], and Yin et al. reported the synthesis of 3 nm ceria nanoparticles using sonochemical treatment [32]. Wang et al. prepared the 2.8 nm ceria nanoparticles by the sonochemical and microwave-assisted heating method [33].

Besides size control, different shapes of nano ceria can be obtained by series of synthesis methods such as ceria nanorods [34], ceria nanowires [30], and ceria nanosheets [35]. Figure 1.2 shows examples of significant ceria samples synthesized by different methods.

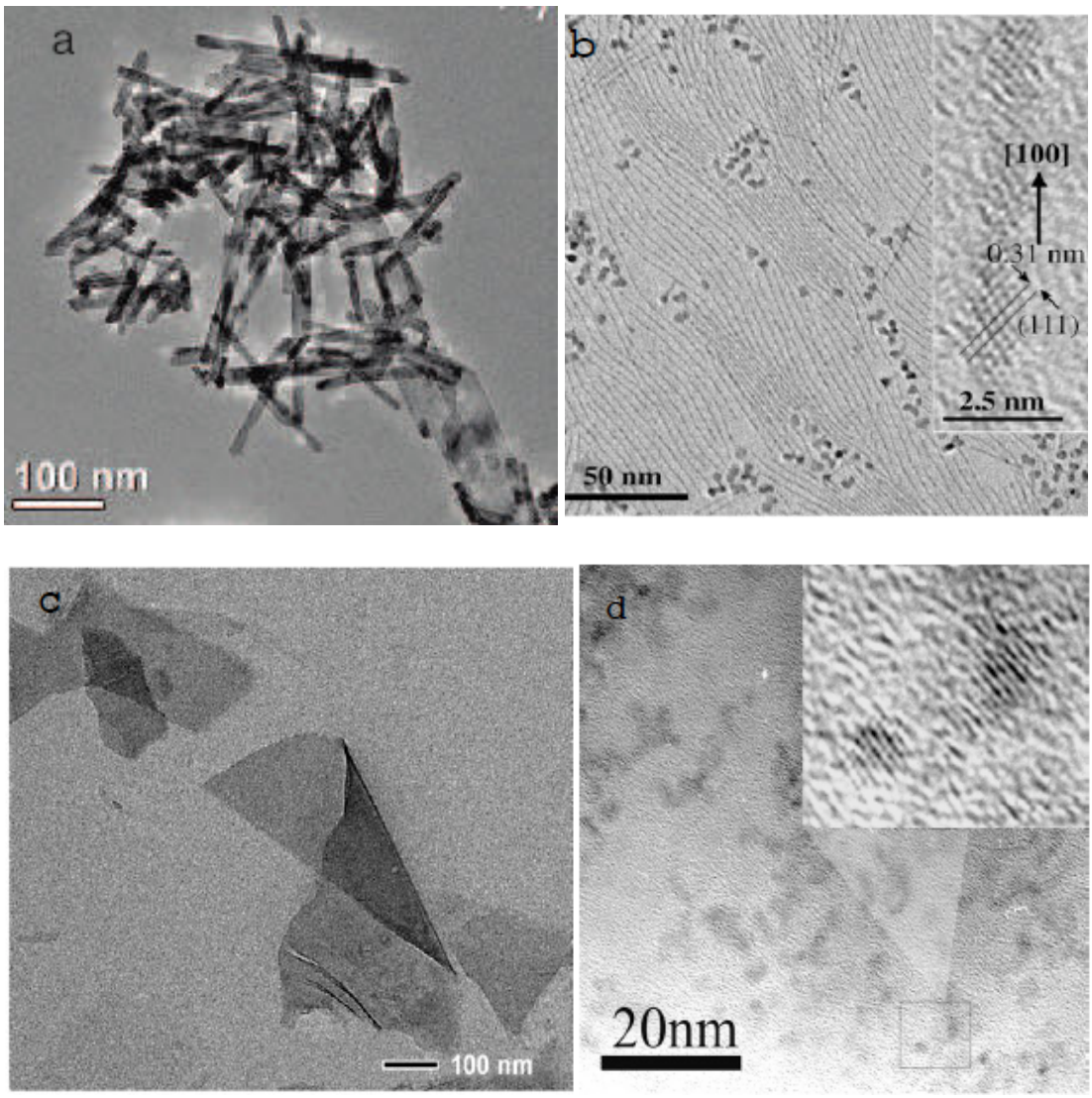

Figure 1.2 (a) Magnified HRTEM of a typical nanorod by a solid based hydrothermal method [34]; (b) TEM images of wire-shaped ceria nanocrystals by sol-gel method, and the inset is the HRTEM image of a wire-shaped nanocrystal [30]; (c) TEM image of a self-folded nanosheet of ceria by an aqueous route [35]; (d) HRTEM images of ceria nanoparticles prepared by microwave irradiation [33].

1.1.4 Structural Properties

1.1.4.1 Crystallite Structure of Ceria

Cerium, with a $4f^2 5d^0 6s^2$ electron configuration, can exhibit both the +3 and +4 oxidation states, and intermediate oxides whose composition is in the range Ce_2O_3 - CeO_2 can be formed. Thermodynamic data indicate that cerium metal is unstable in the presence of oxygen and that Ce_2O_3 and CeO_2 are easily formed. The final stoichiometry is highly dependent on temperature and oxygen pressure. Also, when CeO_2 starts to form, Ce_2O_3 is unstable toward oxidation and is oxidized to CeO_2 [36].

The dioxide CeO_2 crystallizes in the fluorite structure. It has a face-centred cubic unit cell (fcc) with the space group Fm3m (Figure 1.3a) and exposes the most thermodynamically stable (111) surface.

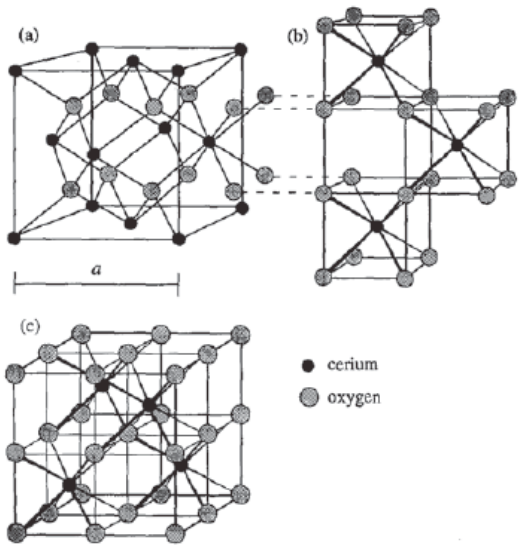

Figure 1.3 The axonometric view of CeO_2 structure, which can be composed as a collection of cubic and cubic centred (cerium in the middle) crystallographic oxygen elements [1].

As illustrated in Figure 1.3, each cerium cation is coordinated by eight equivalent nearest neighbour oxygen anions at the corner of a cube, each anion being tetrahedrally coordinated by four cations. This can be thought of as a cubic close packed (ccp) array of cerium ions with oxygen ions occupying all the tetrahedral holes. Extending the structure by drawing cubes of oxygen ions at each corner reveals the eightfold cubic coordination of each cerium, which alternately occupies the centre of the cube. It is therefore also possible to move the origin and redraw the elementary cell as a primitive cubic array of oxygen ions, in which the eight coordination sites are alternately empty and occupied by a cation. And there are large vacant octahedral holes in the structure, which may be a significant feature to mention the movement of oxygen anions (or oxygen vacancies in opposite direction) through the defect structure.

1.1.4.2 Defects in Ceria

Ceria has been demonstrated to display a strong tendency to form a significant quantity of oxygen defects on its surface under mild conditions. These defects are highly mobile over a range of ceria stoichiometries, indicative of the ease with which they are formed and eliminated producing what is known as a high "oxygen storage capacity" [1].

Ceria crystallizes in the fluorite structure, in which the Ce^{4+} cation is surrounded by eight equivalent O^{2-} ions forming the corner of a cube, with each O^{2-} coordinated to four Ce^{4+}. Defects in ceria can be intrinsic and extrinsic. Intrinsic defects may be present due to thermal disorder and can be created by reaction between the solid and

the surrounding atmosphere (e.g. redox processes), whereas extrinsic defects are formed by either impurities or the introduction of aliovalent dopants.

Intrinsic defects might be generated without involving exchange with the gas phase by the thermal disorder reactions are of the Schottky (Equation 1.3) and Frenkel (Equation 1.4 and 1.5) types, which can be expressed by the Kröger-Vink defect notation as follows:

$$Ce_{Ce} + 2\,O_O \leftrightarrow V''''_{Ce} + 2\,V^{\bullet\bullet}{}_{O}{}^{2-} + CeO_2 \qquad \Delta E = 3.53\ eV \qquad (1.3)$$

$$Ce_{Ce} \leftrightarrow Ce_i^{\bullet\bullet\bullet\bullet} + V''''_{Ce} \qquad \Delta E = 11.11\ eV \qquad (1.4)$$

$$O_O \leftrightarrow O''_i + 2\,V^{\bullet\bullet}{}_{O}{}^{2-} \qquad \Delta E = 3.2\ eV \qquad (1.5)$$

In the above defect reaction, O_O and Ce_{Ce} represent oxygen and cerium at their respective lattice sites, $V^{\bullet\bullet}{}_{O}{}^{2-}$ and V''''_{Ce} indicate respectively oxygen and a cerium vacancy, and $Ce_i^{\bullet\bullet\bullet\bullet}$ and O''_i a cerium and oxygen ion in an interstitial position. The effective charge is indicated by a dot (•) for each positive charge and a prime (′) for each negative charge.

In early work [36-39], there was discussion as to whether these substitutional negative defects were balanced by some of the Ce^{3+} going on interstitial sites as $Ce_i^{\bullet\bullet\bullet}$ or by oxide ions vacancies $V^{\bullet\bullet}{}_{O}{}^{2-}$. Later works using oxygen self-diffusion studies [40-42] in nonstoichiometric CeO_2 appear to show that the behaviour was consistent with the oxygen vacancy model. It is now generally agreed that the main compensation defects in CeO_2 are oxygen vacancies. Thus, the predominant defect category is the Frenkel-type from variation in ΔE in Equation 1.5, which leads to the

formation of pairs of oxygen vacancies and oxygen in interstitial positions.

Generally, these defects are present in low concentration and do not produce any deviation from stoichiometric composition. In ceria, however, a high concentration of defects can be formed by exposure to reducing gaseous atmospheres. Oxygen vacancies are assumed to compensate the holes formed on reduction. If the oxygen is removed, the crystal will end up with an overall positive charge and two electrons need to be introduced for each oxygen ion moved in order to keep the crystal charge neutral. These electrons are associated with two cerium atoms with their charge changed from +4 to +3. The effective charge of the anion vacancies is positive, thus neutralising the negatively charged holes.

To conclude the discussion above, the formation of the oxygen vacancy in ceria can be described as the following reaction:

$$2\,Ce_{Ce} + O_O \leftrightarrow V^{\bullet\bullet}{}_O^{2-} + 2\,Ce'_{Ce} + \tfrac{1}{2}\,O_2 \qquad (1.6)$$

where Ce'_{Ce} is a singly charged cerium atom in a cerium site.

More complex defect chemistry work has been suggested over the course of the development of microscopy technology. In 2005, Esch et al. provided a new insight into ceria (CeO_2) surface in Science magazine, describing and directly showing the immobile oxygen vacancies on the surface of ceria using high-resolution scanning tunneling microscopy (STM) [43, 44]. It was the first time that different types of defects on CeO_2 (111) surface were directly observed (Figure 1.4).

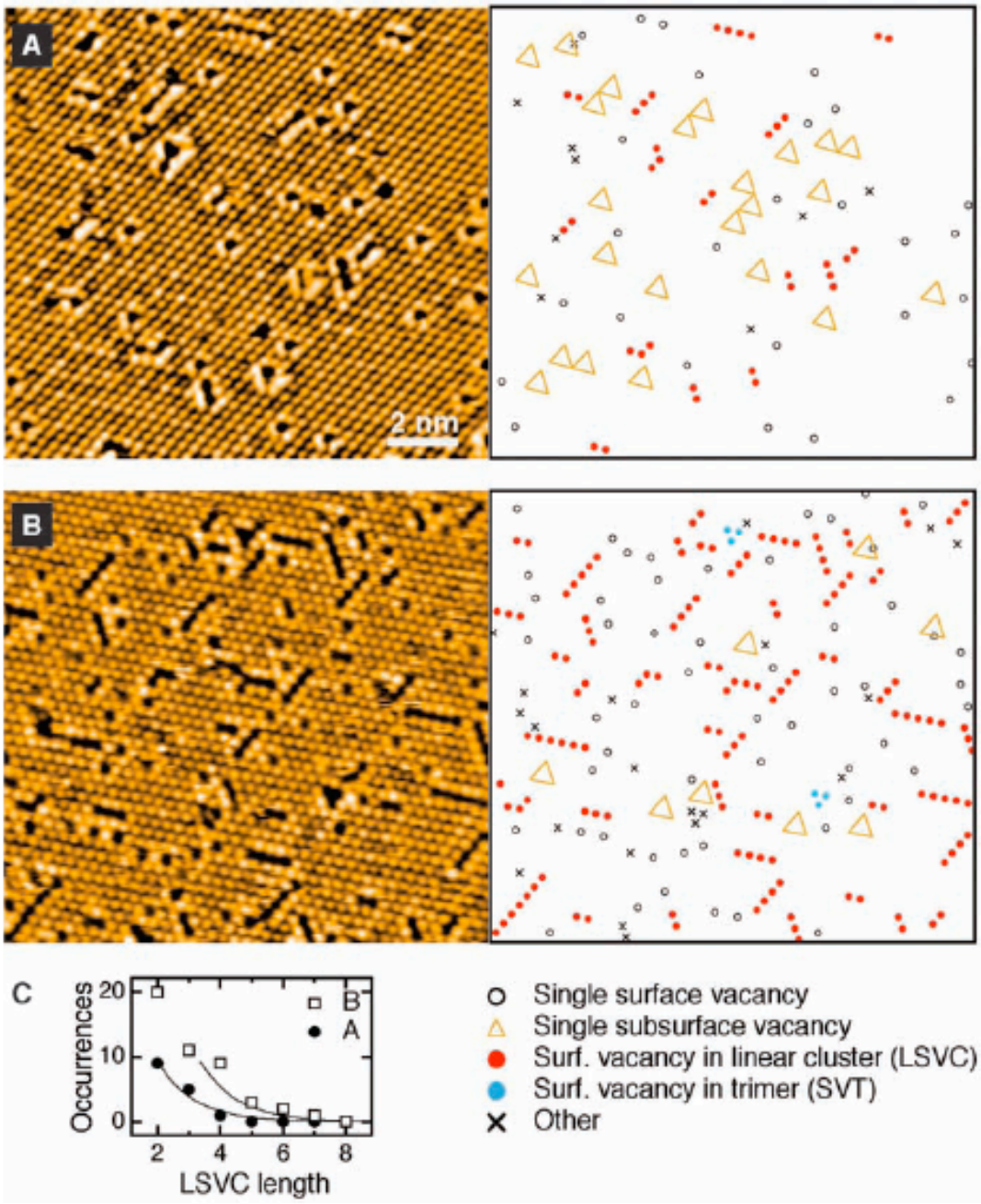

Figure 1.4 (A and B) STM images of the CeO_2(111) surface obtained after 1 min (A) and 5 min (B) of annealing at 900 ^{o}C, with corresponding representations of the observed defects. (C) Histogram of the LSVC distribution as evaluated from (A) (solid circles) and (B) (open squares). The same exponential decay with a rigid shift in defect length can be used to fit both distributions (solid lines). The dominant VCs after prolonged annealing are LSVCs (involving 68% of all O vacancies) and some SVTs (2%); 23% of the O vacancies are single ones. "Other" refers to cases (7%) where the assignment is ambiguous. STM imaging conditions: -3.0 V (sample with respect to tip), 0.3 nA, 300 ^{o}C. [44]

In Figure 1.4, as well as the interactions energy between the defects, three types of vacancies are investigated in the above STM images: single vacancy, linear surface oxygen vacancy cluster and surface oxygen vacancy in trimer cluster. Single vacancies can be distinguished as surface O vacancies and subsurface O vacancies, and they are only coordinated by Ce^{3+} ions. Linear surface oxygen vacancies and trimer surface oxygen vacancies are formed at higher temperatures.

Esch et al.'s work notes the change from Figure 1.4A to Figure 1.4B. After annealing at 900 ^{o}C for 1 and 5 min, the oxygen vacancies are immobile and the linear and trimer oxygen vacancy clusters are formed after the high temperature treatment [44]. On the other hand, Namai et al. reported the highly mobile oxygen vacancies on CeO_2 (111) surface at room temperature [45, 46]. Although the issue of whether the oxygen vacancies remain stationary is still controversial, it is clearly confirmed that there are different types of oxygen vacancies with a significant quantity on the surface of CeO_2.

1.1.4.3 Nano Ceria

Catalysis plays an important part in almost every industrial process and its chemistry occurs at the surface-substrate interface. Hence, a fundamental understanding of the precise nature of the surface chemistry involved allows for the rational design of novel materials for catalysis and other applications such as optical displays, solar panels and corrosion prevention. Many of the most interesting of these effects that can be used advantageously stem from oxygen vacancies and step edges

on the surface of the metal oxide due to the greatly increased reactivity observed. All these features occur on the scale of 10^{-9} m, the so-called nanoscale.

In the water gas shift (WGS, $CO + H_2O \leftrightarrow CO_2 + H_2$) reaction, using a nanoparticulate ceria support as well as co-precipitated gold/ceria on titania surface have shown substantial activity, but surprisingly neither ceria, gold or titania display any activity for the reaction when in the bulk phase [47, 48]. In fact, nanostructured ceria is becoming widely used for different applications in different fields. One such example was presented in 2004, Deluga et al. reported ethanol and ethanol-water mixture converting directly into H_2 with ~100% selectivity and >95% conversion by catalytic partial oxidation with a residence time on rhodium-cerium nanocatalysts of <10 milliseconds [49].

The use of nanostructured CeO_2-based materials can dramatically improve or even create desirable properties due to further enhancement of oxygen storage properties in comparison to micron sized or bulk-like materials [50]. Decreasing the ceria particle size not only increases the oxygen vacancies and surface area but also changes the structural, electronic, and lattice vibrational properties for the development of advanced materials [50-56]. Most of these properties display an apparent variation while the particle size is reduced to < 10 nm.

Due to the improvements in analytical techniques, researchers can now look in detail at the nature and the size of crystallographic planes, as well as the structure and chemical composition of solid nano-catalysts [57]. In studies of nanoscale ceria, size contributions from the structure of the material, for example lattice expansion, have been demonstrated by many independent pieces of theoretical research. X-ray diffraction studies have shown that crystalline ceria nanoparticles have a cubic fluorite type (fcc) structure, but that this structure has large lattice expansions [50, 52,

55]. Figure 1.5a [52] shows the inverse relationship between the lattice parameter and increasing particle size.

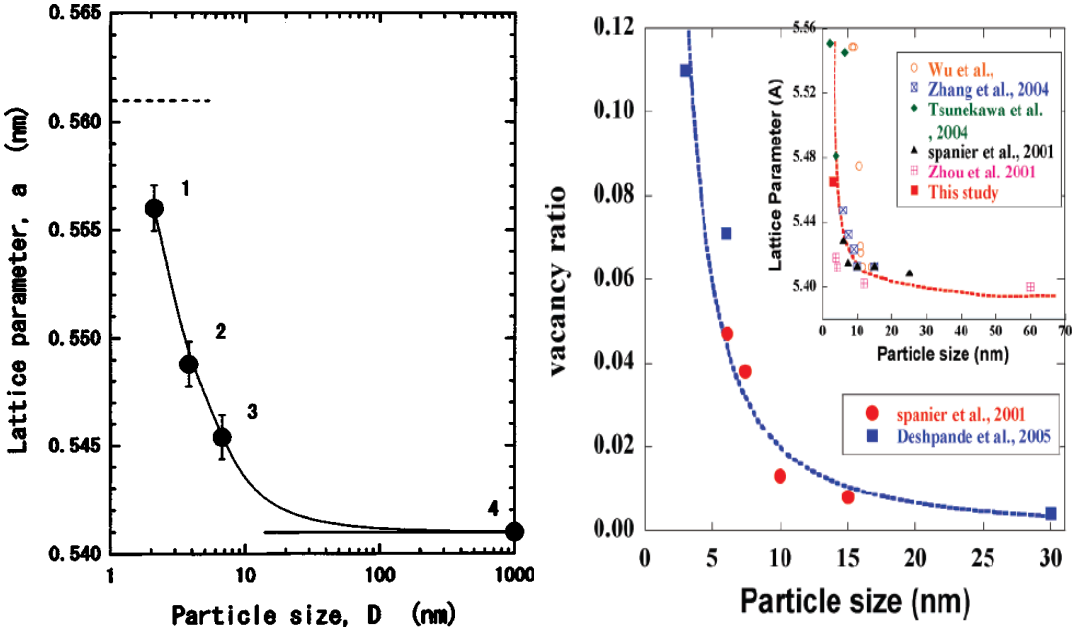

(a) (b)

Figure 1.5 (a) Correlation of particle size and lattice parameter [52]; (b) Correlation between vacancy ratio, lattice parameter (insert) and particle size [58].

This lattice expansion is reported to be a property of the ceria nanocrystals, and is largely confined to the sub-10 nm range [58]. Some authors (mostly those who followed the work of Tsunekawa et al. [59, 60]) presumed that it is the result of the increased concentration of Ce^{3+} and associated oxygen vacancies of ceria nanocrystals. Because, as previously explained, an oxygen vacancy resulting from the removal of an oxygen atom in the crystal of ceria changes the oxidation state of the neighbouring Ce^{4+} to Ce^{3+}. Ce^{3+} has a larger ionic radius than Ce^{4+}. Wang et al. collated a series of vacancy ratios against particle sizes and lattice parameters (Figure 1.5b) [58] in 2007. This is an evidence for this hypothesis. Furthermore, it is now

mostly agreed that the concentration of oxygen vacancies is directly related to the Ce^{4+}/Ce^{3+} redox history of the samples. It has been reported that the increased lattice parameter is indicative of an increased concentration of Ce^{3+} ions [55], and it is subsequently thought to match increased oxygen vacancies. However, there are also a number of conflicting findings within the literature [61]. As a result, even though there is little evidence of a consistent model emerging to explain lattice parameter changes with nanocrystal size ceria, more work is needed to explain the relationship between oxygen vacancies and the lattice expansion of nano ceria. Furthermore, it is still doubtful whether the special oxygen storage capacity (OSC) from nano ceria, which is thought to be the major reason for extremely high activity in most of the catalysis reactions such as WGS reaction happening on the nanoscale ceria based materials, can be connected directly with this kind of lattice expansion or not.

1.1.5 Oxygen Storage Capacity (OSC)

The oxygen storage capacity (OSC) of ceria is related to the tolerable level of oxygen non-stoichiometry, and is a critical issue for ceria related materials when they act as redox catalysts in different fields. For example, Aneggi et al. [62] explained the role of catalytic activity of ceria in soot oxidation as being primarily based on the OSC due to the reduction/oxidation of catalyst oxide analogous to catalytic CO oxidation.

1.1.5.1 Ce^{4+}-Ce^{3+} Redox Cycle

A cursory examination of the OSC for ceria appears to show it to be a very simple concept based on its ability to cycle between Ce^{4+} and Ce^{3+}. The widest application of ceria is in the use of ceria-alumina (zirconia) to disperse Pt(Pd)-Rh for automotive catalysis in vehicles [1]. In automotive catalysis, it is very difficult for the CO and hydrocarbons oxidation to happen simultaneously with the reduction of NO_x. If only precious metals are present in a catalyst, there is a lack of selectivity for oxidation of CO and hydrocarbons using NO_x in the presence of O_2 and the air/fuel ratio also needs to be strictly balanced in the engine to remove all these major pollutants. Nevertheless, under real driving conditions, exhaust gas composition may vary drastically. Hence, ceria is added into this catalytic formulation to buffer exhaust composition through its oxygen storage capacity (OSC) [63].

When O_2 has excessive presence in the exhaust stream, ceria is thought to remove the excess oxygen by oxidizing Ce^{3+} back to Ce^{4+}, while CO and hydrocarbons simultaneous reduce NO_x. On the other hand, when there is an insufficient amount of

NO_x and O_2 in the exhaust stream to oxidize the CO and hydrocarbons, ceria will release the oxygen. This release does not involve the formation of gas phase O_2. However, it has been suggested that the role of ceria in automotive exhaust catalysis is far more complex than this, and subtler than as described above [63-66]. It is argued that if ceria is only a simple oxygen capacitor, it should be possible to determine the OSC of ceria by simply measuring the amount of oxygen that can be removed and added when the catalyst is exposed to alternating CO and O_2 pulses. However, this conflicts with the fact that the CO-O_2 titration method does not properly characterize what happens in a catalytic converter containing ceria [66]. For example, it is well documented that introducing SO_2 into vehicle exhaust leads to lost of the OSC of ceria-base materials. But in experiments with alternating CO-O_2 pulses, these ceria-base catalysts are found to reversibly release much more oxygen after they have been exposed to SO_2 [65]. Obviously, the simple Ce^{4+}-Ce^{3+} redox cycle model is not able to explain all aspect of the OSC of ceria.

1.1.5.2 Oxygen Transfer

Pure ceria is not stable when used in a vehicle exhaust system and it quickly loses its OSC. In practical catalysts, ceria is used in the form of a mixed oxide with zirconia [67-70]. It has been claimed that the deactivation of ceria is due to the loss of surface area. Cuif et al. [70] observed an increase of the preserved surface area of aged oxide with the introduction of 10 at.-% Zr and the maximum stabilization was obtained with 60 at.-% Zr. The incorporation of Zr interestingly improved the OSC. They attributed the improved OSC of the mixed oxide to the increased surface area because the increased surface area may supply the additional reactive oxygen. However, some

people disagree with this surface extension explanation. Sagiura et al. [71] reported that a similar loss of surface area was exhibited in $Ce_xZr_{(1-x)}O_2$ also, but interestingly they found that the catalysts did not lose their OSC and worked rather well.

More studies reported similar results, indicating that the incorporation of zirconium into the CeO_2 lattice would improve the OSC greatly [72-75]. Trovarelli et al. [74] studied the OSC on $Ce_xZr_{(1-x)}O_2$ solid solutions prepared by mechanical milling of the ceria and zirconia. They observed approximately 185 μmol/g of oxygen in the mixed oxide, much more than in pure ceria. The largest OSC of $Ce_xZr_{(1-x)}O_2$ was obtained by Madier et al. [72]. In their work, all $Ce_xZr_{(1-x)}O_2$ oxides had a fluorite-type structure, and the largest OSC was obtained from $Ce_{0.63}Zr_{0.37}O_2$ with a 219 μmol/g of oxygen, 4 times larger OSC than in pure ceria. Furthermore, they also reported that in the case of pure ceria, OSC was restricted to the surface. In contrast to this, the OSC of $Ce_xZr_{(1-x)}O_2$ took place not only at the surface but also in the bulk. They found that the participation of bulk oxygen, e.g. at least one sub-surface oxygen layer, was involved in the oxygen storage process [72]. It is proposed that the formation of structural defects (oxygen vacancies) [76] by the introduction of zirconia should be responsible for such a high amount of extra available oxygen [77]. Hori et al. reported that doping zirconia into ceria might influence oxygen binding in ceria [78] and might cause oxygen transfer between the bulk and surface which would affect the OSC of ceria zirconia oxides.

Besides the introduction of zirconia for supporting the noble metals, rhodium in particular, plays an active role in promoting the OSC of the ceria [79-81]. Furthermore, Kacimi et al. [82] reported that the OSC of ceria could be affected by certain other elements incorporated during the preparation or getting adsorbed during catalysis. The effect of various additives (V, Cr, Mn, Fe, Co, Ni, Cu and Pb) was

studied on the OSC of CeO_2 and Rh/CeO_2 catalysts. In their work, Co, Ni and Cu were found to promote the OSC of both ceria and Rh/CeO_2 while Cu also showed an exceptional effect on improving catalyst stability.

Many authors have compared the activity of noble metals (Pt, Pd, Rh) supported on Al_2O_3 and CeO_2-Al_2O_3 in the CO oxidation reaction, and they found that the promoter effect of ceria on noble metals to be more pronounced for the stoichiometry CO/O_2 mixture than in O_2 excess condition [83-85]. Oh and Eickel clearly illustrated this aspect of the CO oxidation reaction [84].

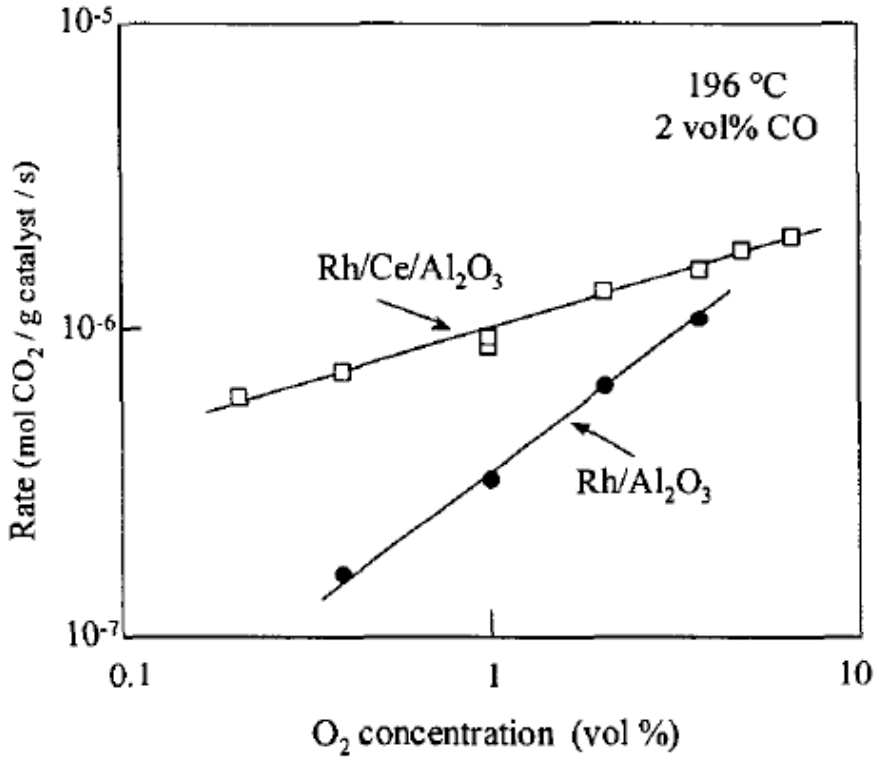

Figure 1.6 Effect of ceria on CO oxidation over Rh catalysts [85].

As shown in Figure 1.6, the rate of CO oxidation dramatically decreases linearly at low O_2 gas concentrations over Rh/Al_2O_3, while the reaction over Rh/CeO_2-Al_2O_3 decreases rather gradually upon the concentration of O_2 decreasing. Thus, with the

presence of ceria, the sensitivity of the reaction rate to gas phase O_2 concentration of the catalysts was decreased. A mechanism involving CO_2 formation via a reaction between CO adsorbed on Rh and surface oxygen derived from the neighbouring ceria particles is proposed. This mechanism implies that an oxygen vacancy is formed by the reaction of CO_{Rh} on O_{Ce}, and that this vacancy is thereafter filled by O_2 adsorption.

The oxygen transfer happening in the ceria related catalysts is generally agreed as the result of the existence of oxygen vacancies in the nonstoichiometric ceria [86-90]. Because of the existence of oxygen vacancies as well as the large vacant octahedral holes in the fluorite-type structure of ceria [91-93], the diffusion of oxygen in nonstoichiometric ceria is much faster than stoichiometric ceria and other oxides. When the availability of oxidant from the gas phase is not constant, a continuous supply of oxygen from the bulk to the surface guarantees a constant concentration of active surface oxidation sites or supplies more available oxygen [94]. Also, the O_2 adsorption on the surface of ceria would be a determining factor of the OSC in most of the catalytic reactions because ceria is the major OSC component of the catalysts and the active sites such as oxygen vacancies contribute to the OSC mainly localized at the ceria surface [95].

Further kinetic studies have confirmed that a bifunctional mechanism exists for CO oxidation over M/CeO_2 (M = Rh, Pt, Pd) implying two types of sites, one for CO adsorption and one another for O_2 adsorption [86, 96-98]. For example, a dual role for ceria in promoting CO oxidation was proposed by Fernandez-Garsia et al. [86] to explain the high activity of their catalysts: ceria would facilitate Pd reduction by CO (and thus CO adsorption) while it provides sites for O_2 adsorption. However, although it is already generally agreed that the higher performances in CO oxidation are

promoted by zirconium oxide doped or metal doped ceria material than pure ceria, the nature and localization of adsorbed O species in CO oxidation over ceria containing catalysts is still a matter of debate.

1.1.5.3 Surface Oxygen Species

Surface oxygen species of ceria are postulated to be kinetically significant intermediates in a number of oxidation reactions, and the study of these species is therefore important for the understanding of the mechanism of oxidation reactions catalyzed by ceria related materials [99-103].

Activation of oxygen on ceria is a necessary prerequisite to the understanding of catalytic properties. Both superoxide and peroxide ions play important roles to redox reaction. Superoxides and peroxides have also been presented as "virtual" intermediates in the complete reoxidation route of nonstoichiometric ceria, where electrons are progressively transferred from the solid to the dioxygen molecules [104]:

$$O_{2gas} \rightarrow O_{2ads} \rightarrow O_{2ads}^{-} \text{(superoxide)} \rightarrow O_{2ads}^{2-} \text{(peroxide)} \rightarrow 2\ O_{ads}^{-} \rightarrow 2\ O_{lattice}^{2-}$$

In 2000, Descorme et al. reported that it was clearly observed that OSC varies as a function of the population of O_2^- species estimated on $Ce_xZr_{(1-x)}O_2$ (Figure 1.7) by the FT-IR Spectroscopy characterization and the following $^{16}O/^{18}O$ isotopic exchange experiment [81].

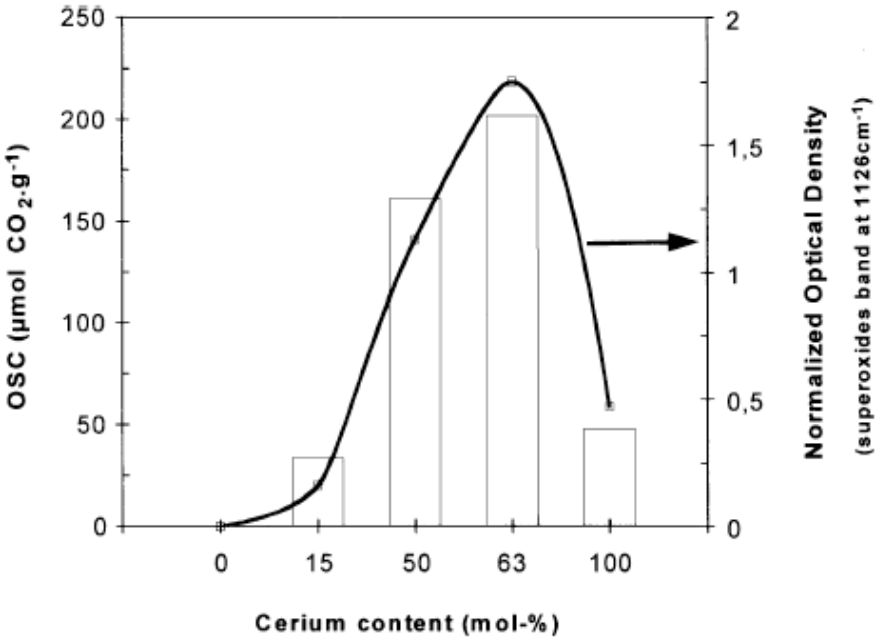

Figure 1.7 Correlation between the oxygen storage capacity at 400 °C and the amount of superoxides formed upon oxygen adsorption at room temperature on a series of preoxidized $Ce_xZr_{(1-x)}O_2$ mixed oxides (x = 1, 0.63, 0.5, 0.15, and 0) [81].

The adsorption of the gaseous dioxygen by the surface oxygen vacancies and the subsequent interaction between the molecular oxygen with a neighbouring reduced cerium (Ce^{3+}) potentially leads to the formation of a number of extremely active surface oxygen species [99]. The type of interaction would determine the reoxidation of Ce^{3+} to Ce^{4+} and the subsequent formation of O_2^- species [104-107]. In a more simplistic approach, this interaction could be presented as the transfer of one electron from the single oxygen vacancy to the dioxygen molecules:

$$Ce^{3+} + V_O + O_2 \rightarrow Ce^{4+} + O_2^- \qquad (1.7)$$

Similarly, the formation of peroxide species (O_2^{2-}) on pre-reduced solids, observed

in some studies [104], could be understood as the result of the reaction of molecular oxygen in the oxygen vacancy with two neighbouring Ce^{3+}. In this case, two electrons are transferred from the solid to the oxygen molecules.

For pure ceria, quantum chemical calculations such as density-functional theory (DFT) methods have been used by several groups [108, 109], to predict the adsorption situation between the molecular oxygen and the pure CeO_2 surface. This work gives the support to the theory that reduced ceria surfaces with oxygen vacancies are energetically more favourable than unreduced surfaces for oxygen adsorption, and can form stable superoxides.

Some thermodynamic description of defects in $Ce_xZr_{(1-x)}O_2$ mixed oxides by Janvier et al. [110] suggested that higher ability of ceria zirconia mixed oxides for oxygen storage could initially be related to the higher concentration of oxygen vacancies at the surface. In such systems, the stabilization at or near the surface of nonstoichiometric defects in high concentration could result in an enhanced ability to activate oxygen as superoxides, which are thought to be initiators of the whole storage process.

Among studies concerning noble metals deposited onto ceria, there is hypothesis that the superoxide and peroxide ions close to the metal-ceria interface might be the true catalytically active species, and the role of metal might be only that of donor/acceptor of electrons [111].

To summarize, it is agreed by most authors that the active oxygen species such as superoxides and peroxides formed on the surface of ceria are related to the active oxygen vacancies present, although more experimental evidence is still needed.

1.2 Heterogeneous Catalysis

1.2.1 Definition and Kinetics

Catalysis is one of the most important technologies with a world market value of greater than US $100 billion per year in the modern world, and it continues to grow rapidly. The word “catalyst”, was first defined in 1836 by Baron J.J. Berzelius, to describe the ability of substances to increase the rate of a chemical reaction without being consumed in the reaction. Although the equilibrium composition of reactants and products is solely determined by thermodynamics, catalysts can greatly affect the rate of the reaction [112].

For a heterogeneous catalysis, the catalysts are present in different phases from the reactants and products and the catalysts are usually solid [112]. The main advantage of using a heterogeneous catalyst is that it is relatively easy to separate the catalyst from the product stream which helps in the creation of continuous chemical processes. More than 90% of the chemical manufacturing processes in the world are controlled by heterogeneous catalysis, including as the production of plastics, energy sources, synthetic fibres, paper products, polymers, pharmaceuticals, modern building materials, agricultural products, and so on [113].

A heterogeneous catalytic reaction involves adsorption of reactants from a fluid phase onto a solid surface; the surface reaction of the adsorbed reactants; and desorption of products into the fluid phase once again. The presence of the catalyst is a platform for the heterogeneous catalysis to take place. A catalytic process can be described by the different parameters such as activity, catalytic reaction rate and selectivity.

The activity can be expressed by the conversion of the reactants into products, or alternatively measured as a turnover frequency (TOF), which is the number of molecules of products formed per unit time per surface atom or per unit surface area of the catalyst.

The catalytic reaction rate (r) for a generic reaction ($A + B \rightarrow C$) is proportional to the concentration of the reactants raised to a power and can be expressed by the rate equation:

$$r = k[A][B] \qquad (1.8)$$

[A] and [B] are the concentrations of the reactants and raised to the first power. The coefficient k is called the rate constant for the reaction and is independent of the concentration but varies with temperature. The rate constant is found experimentally for many reactions, using the Arrhenius equation by plotting ln$k$ against 1/T, where T is the temperature:

$$K = Ae^{-E/RT} \qquad (1.9)$$

Where A is the temperature-independent pre-exponential factor, R is the gas constant and E is the activation energy for the reaction, which is calculated from the gradient of the graph.

The selectivity is defined as the amount of the desired product obtained per amount of consumed reactant and can be expressed as follows:

$$\text{Sel } a_i\% = (a_i/\Sigma a) \times 100 \qquad (1.10)$$

Where a_i is the desired product concentration and Σa is the sum of the products' concentrations. One of the major aims of the catalysis research is to achieve higher selectivity for catalyst based reaction processes.

1.2.2 Active Sites

In order to understand the molecular processes of the heterogeneous catalysis taking place on the surface of a catalyst, the nature of the site promoting the reaction must be defined. Taylor originally put forward the idea of active sites for catalysis in 1925 [114]. There are many different sites on the surface of catalysts, which are distinguishable by their number of nearest neighbours, and various sites will have different characteristics for the reaction [114]. The reactions on the heterogeneous catalysts typically involve interaction between the surface atom and the reactant molecule. The active sites normally come from the active components (metal or metal oxide particles) on supports and these active components are usually nanosized in the range of 1 to 100 nanometres [113].

In supported metal catalysts, the surface of the metal is mainly involved in the catalysis and is linked to the catalytic reactivity. The main advantage of using nanoparticles is to maximize the surface area exposed to the reactants, which lead to higher reactivity. Moreover, the higher the number of metal atoms in contact with the support (leads to higher interface), the better the catalyst performance [113]. In addition, peculiar properties for some metal/metal oxide particles of critical sizes have been observed. For example, the bulk gold is not reactive but nano gold become

catalytically active in very particular size range variously considered to be 2-3 nm [115, 116] or 3-5 nm [117-119] when it presents to the chemical environment as discrete. Furthermore, for metal catalysts, with smaller particle size, there is electronic properties and higher abundance of different types of metal atoms such as edges, corners, terraces, which act as active sites for the structure sensitive reactions [120-122]. However, thermal stability of these nanostructures is limited by their size. The smaller the particle size is, the lower the thermal stability.

1.2.3 Deactivation

Metal catalysts are very susceptible to deactivation in their working environment where they encounter high temperatures and extreme pressure. They are also exposed to surface poisons either from reaction by-products or the atmosphere [113].

Sintering is the major problem for nano catalysts. It makes nanoparticles form as the larger particles under the catalytic reaction conditions and even during the catalyst preparation. Due to a decrease in the number of exposed metal atoms, and the loss of the smallest particles that make them especially reactive in the sintering, catalysts will lose their activity or selectivity. For the supported nano catalysts, the sintering involves a complex chemical and physical phenomenon that makes the understanding of the sintering mechanism difficult [123].

Being poisoned with other compounds or elements can also deactivate catalysts. Poisoning is defined as a loss of catalytic activity due to the chemisorption of impurities on the active sites of the catalyst. Poisons interact irreversibly with the surface active sites of catalysts, thus preventing reactants gaining access to the active site, which results in a decrease or total loss of activity. Solving the deactivation

problem is always one of the major challenges when designing catalysts.

1.2.4 Encapsulated Metal Catalysts

It is important to design catalysts which are highly selective, efficient and specific to a certain type of reaction, as this can facilitate significant savings in manufacturing expenses such as energy consumption and waste production. Recently, in order to achieve nanostructured catalysts with higher activity and thermal stability than those currently available, great attention has been dedicated to the development of novel synthetic methods distinct from traditional methods such as wet impregnations, ionic exchange and thermal decomposition [124]. An innovative and promising approach based on the incorporation of metal nanoparticles into a porous oxide's shell of support in order to inhibit the sintering of the nanoparticles at high temperatures was first demonstrated by our group [125] and the concept was then extensively investigated by Budroni et al. [126]. The porous nature of the support prevents the total occlusion of the nanoparticles, thus favouring the access of the reactants to the catalytic sites. The innovation of this approach relies on the covalent link between the preformed metal nanoparticles and growing support, which accounts for the superior catalytic activity and stability of such materials.

An alternative encapsulating approach to directly coat the metal nanoparticles with a nano porous oxide shell was also reported [127-130] and the thermal stabilization of metal nanoparticles involved in reactions operating at very high temperatures is achieved (ca. 900 ^{o}C). These core-shell nano catalysts are expected to have unique implications in catalysis, which are not present in either shell or core materials [131-133]. The outer shells isolate the catalytically active nanoparticles cores, so the

possibility of sintering the core particles during the high temperature reactions is prevented. Moreover, the particular connection in terms of physical and/or chemical interaction can create synergic effects and the interaction maximizes metal-support interface which is important in catalytic performances.

Due to the lower tendency to oxidize/redissolve during preparation conditions with respect to the other transition metals, encapsulated noble metal based catalysts have been thoroughly investigated. For example, Au, Pd in SiO_2 and TiO_2 core shell materials with very small core particle size about of 1-3 nm were reported [134, 135], to be more stable against the sintering and catalytically active in some reactions. Non-noble metals core-shell materials such as Ag@TiO_2 [136], Ag@SiO_2 [137], Ni@SiO_2 [138], Ni@MgO/Al_2O_3 [139] with improved reactivity were also reported.

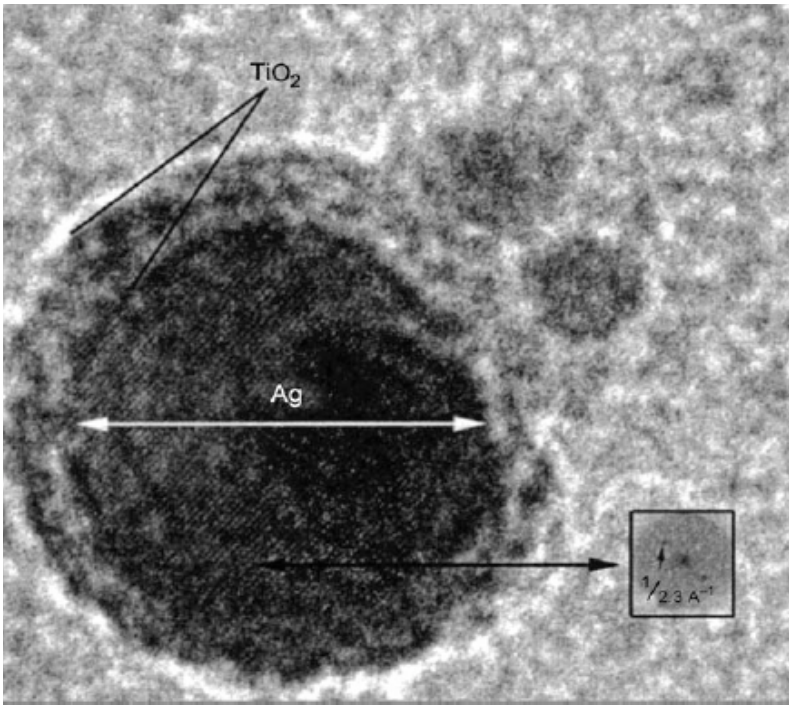

Figure 1.8 HRTEM of Ag@TiO2 showing the crystalline nature of the metallic core and the amorphous nature of the shell [136].

Our group has produced deeply encapsulated Pt in ceria samples by a microemulsion method. CO chemisorption data indicated that even if metal loading used was quite high – up to 5%, the active metallic phase is totally inaccessible but the catalysts were active under water gas shift reaction conditions without any methane formed which was the normal side product of conventional Pt on ceria catalysts from the WGS reaction [140-143]. A similar synthesis method will be used in this thesis.

1.3 Scope of Thesis

1.3.1 Objectives

The oxygen storage capacity is commonly thought to play a critical role when ceria acts as a redox catalyst in different practical fields. Much theoretical research reports that the oxygen vacancy concentration is inversely proportional to the particle size of ceria, especially when particle size is less than 10 nm [52, 58]. However, no direct evidence has been found to correlate smaller particle size with the better oxygen storage capacity of nano ceria. For example, how small the particle should be to produce active oxygen vacancies, and which types of oxygen species relating to the oxygen storage capacity are still unknown. Moreover, even though it has been well established that contact with metal/metal oxide will improve the oxygen storage capacity of ceria, study of the mechanism of this progress is still lacking.

The principal aim of this research is to improve understanding of the formation of active oxygen species by the oxygen vacancies on the surface of nano ceria and their catalytic applications in heterogeneous catalysis reactions. Particular focus will be placed upon (1) the preparation of the novel ceria contained catalysts, and their application in the resistance to the carbon formation over Ni catalysts from the methane steam reforming (MSR) reaction; (2) the identification of the surface oxygen species for the pure ceria; and (3) the selectivity enhancement of glycerol hydrogenolysis reaction by adding ceria.

1.3.2 Outline of Project Achievements

The main work of the project has now been successfully completed and chapter layouts are as follows:

1) A brief review of the recent progress in the fundamental studies of ceria related materials and the introduction of heterogeneous catalysts (Chapter 1).
2) Equipment and methodologies for synthesising, testing and characterising metal/ceria based catalysts (Chapter 2).
3) Catalytic evaluation of Ni/ceria based catalysts prepared via a sol-gel and deposition precipitation was carried out using the MSR reaction. Ni-in-ceria core shell catalysts were prepared successfully with a high resistance to carbon formation in a very low water to methane ratio of 0.25, which is comparable to the industrial water to methane ratio 2.5 (Chapter 3).
4) Detailed characterization of a series of microemulsion prepared nano ceria catalysts were performed. The formation of large amounts of stable superoxides (O_2^-) on the surface of nano ceria (< 5 nm) was, for the first time, investigated at room temperature (Chapter 4).
5) The Ni, Ni/ceria and related samples were applied in the glycerol hydrogenolysis reaction. Pt doped ceria samples were employed to shed light on the mechanism of metal accelerating the OSC of cerium oxide (Chapter 5).
6) Finally, the conclusion of this research and possibilities for future work were summarized (Chapter 6).

1.4 Reference

1. A. Trovarelli, Catalysis by Ceria and Related Materials, Imperial College Press, London, 2002.
2. J. Kaspar, P. Fornasiero, Journal of Solid State Chemistry, 171 (2003) 19-29.
3. M. Sugiura, Catalysis Surveys from Asia, 7 (2003) 77-87.
4. L. Kylhammar, P. A. Carlsson, H. Ingelsten, H. Grönbeck, M. Skoglundh, Applied Catalysis B: Environmental, 84 (2008) 268-276.
5. X. D. Feng, D. C. Sayle, Z. L. Wang, M. S. Paras, Science, 312 (2006) 1504-1508.
6. Y. J. Leng, S. H. Chan, S. P. Jiang, K. A. Khor, Solid State Ionics, 170 (2004) 9-15.
7. R. J. Gorte, S. Zhao, Catalysis Today, 104 (2005) 18-24.
8. A. Trovarelli, Catalysis Reviews, 38 (1996) 439-520.
9. S. Zhao, R. J. Gorte, Applied Catalysis A: General, 277 (2004) 129-136.
10. E. L. Lopez-Navarrete, A. Caballero, A. R. Gonzalez-Elipe, M. Ocana, Journal of Materials Research, 17 (2002) 797-804.
11. K. Niesz, D. E. Morse, Nanotoday, 5 (2010) 99-105.
12. H. Chen, H. Chang, Ceramics International, 31 (2005) 795-802.
13. Y. Wang, T. Mori, J. Li, T. Ikegami, Journal of the American Ceramic Society, 85 (2002) 3105-3107.
14. T. Tsuzuki, J. S. Robinson, P. G. J. McCormick, Journal of Australasian Ceramic Society, 38 (2002) 15.
15. F. Bondioli, A. M. Ferrari, L. Lusvarghi, T. Manfredini, S. Nannarone, L. Pasquali and G. Selvaggi, Journal of Materials Chemistry, 15 (2005) 1061-1066.

16. M. Hirano, Y. Fukuda, H. Iwata, Y. Hotta, M. Inagaki, Journal of the American Ceramic Society, 83 (2000) 1287-1289.
17. S. Yabe et al., Kidorui, 34 (1999) 124.
18. P. Shuk, M. Greenblatt, Solid State Ionics 116 (1999) 217-223.
19. A. Bumajdad, M. I. Zaki, J. Eastoe, L. Pasupulety, Langmuir, 20 (2004) 11223.
20. A. Hartridge, A. K. Bhattacharya, Journal of Physics and Chemistry of Solids, 63 (2002) 441-448.
21. M. A. Lopez-Quintela, H. Rivas, Journal of Colloid Interface Science, 158 (1993) 446-451.
22. T. Masui, K. Fujiwara, K. Machida, G. Adachi, T. Sakata, H. Mori, Chemistry of Materials, 9 (1997) 2197-2204.
23. T. Masui, K. Fujiwara, Y. Peng, T. Sakata, K. Machida, H. Mori and G. Adachi, Journal of Alloys and Compounds, 269 (1998) 116-122.
24. A. Martinez-Arias, M. Fernandez-Garcia, V. Ballesteros, L. N. Salamanca, J. C. Conesa, C. Otero and J. Soria, Langmuir, 15 (1999) 4796.
25. M. Cauqui and J. Rodríguez-Izquierdo, Journal of Non-Crystalline Solids, 147/148 (1992) 724-738.
26. F. Imoto, F. Nanataki, and S. Kaneko, Ceramic Transactions 1 (1988) 204-10.
27. P. Fornasiero, J. Kaspar, V. Sergo, M. J. Graziani, Journal of Catalysis, 182 (1999) 56-69.
28. A. Makishima, M. Asami, K. Wada, Journal of Non-Crystalline Solids, 121 (1990) 310-314.
29. A. Vioux, Chemistry of Materials, 9 (1997) 2292-2299.
30. T. Yu, J. Joo, Y. I. Park, T. Hyeon, Angewandte Chemie International Edition, 44 (2005) 7411-7414.

31. M. Inoue, M. Kimura, T. Inui, Chemical Communications, 11 (1999) 957-958.
32. L. X. Yin, Y. Q. Wang, G. S. Pang, Y. Koltypin, A. Gedanken, Journal of Colloid Interface Science, 246 (2002) 78-84.
33. H. Wang, J. J. Zhu, J. M. Zhu, X. H. Liao, S. Xu, T. Ding, H. Y. Chen, Physical Chemistry Chemical Physics, 4 (2002) 3794-3799.
34. K. B. Zhou, X. Wang, X. M. Sun, Q. Peng, Y. D. Li, Journal of Catalysis, 229 (2005) 206-212.
35. T. Yu, B. Lim, Y. Xia, Angewandte Chemie, 122 (2010) 4586-4589.
36. C. J. Kevane, Physical Review, 133 (1964) A1431-A1436.
37. P. Kofstad, A. Z. Hed, Journal of the American Ceramic Society, 50 (1967) 681-682.
38. R. N. Blumenthal, P. W. Lee, R. J. Panlener, Journal of the Electrochemical Society, 118 (1971) 123-129.
39. B. Iwasaka, T. Katsura, Bulletin of the Chemical Society Japan, 44 (1971) 1297-1301.
40. B. C. H. Steele, J. M. Floyd, Proceedings of the British Ceramic Society, 19 (1971) 55-76.
41. I. V. Vinokurov, Neorgan. Mater., 6 (1970) 31.
42. I. V. Vinokurov, V. A. Ioffe, Soviet. Phys. Solid State, 11 (1969) 207.
43. C. T. Campbell, C. H. F. Peden, Science, 309 (2005) 713-714.
44. F. Esch, S. Fabris, L. Zhou, T. Montini, C. Africh, P. Fornasiero, G. Comelli, R. Rosei, Science, 309 (2005) 752-755.
45. Y. Namai, K. Fukui, Y. Iwasawa, Catalysis Today 85 (2003) 79-91.
46. Y. Namai, K. Fukui, Y. Iwasawa, The Journal of Physical Chemistry B 107 (2003) 11666-11673.

47. J. B. Park, J. Graciani, J. Evans, D. Stacchiola, S. Ma, P. Liu, A. Nambu, J. F. Sanzc, J. Hrbek, J. A. Rodriguez, PNAS, 106 (2009) 4975-4980.
48. J. A. Rodriguez, S. Ma, P. Liu, J. Hrbek, J. Evans, M. Pérez, Science, 318 (2007) 1757-1760.
49. G. A. Deluga, J. R. Salge, L. D. Schmidt, X. E. Verykios, Science, 303 (2004) 993-997.
50. X. D. Zhou, W. Huebner, Applied Physics Letters, 79 (2001) 3512.
51. A. Tschope, D. Schaadt, R. Birringer, J. Y. Ying, Nanostructured Materials, 9 (1997) 423-432.
52. S. Tsunekawa, S. Ito, Y. Kawazoe, Applied Physics Letters, 85 (2004) 3845.
53. L. Wu, H. J. Wiesmann, A. R. Moodenbaugh, R. F. Klie, Y. Zhu, D. O. Welch, M. Suenaga, Physical Review B, 69 (2004) 125415.
54. F. Zhang, Q. Jin, S. W. Chan, Journal of Applied Physics, 95 (2004) 4319-4326.
55. S. Deshpande, P. Patil, S. V. Kuchibhatla, S. Seal, Applied Physics Letters, 87 (2005) 133113.
56. J. E. Spanier, R. D. Robinson, F. Zhang, S. W. Chan, I. P. Herman, Physical Review B, 46 (2001) 245407.
57. S. C. Tsang, K. Tedsree, Environmental Nano Technologies, 2010, 34-39.
58. C. F. Wang, J. N. Wang, Z. M. Sheng, The Journal of Physical Chemistry C, 111 (2007), 6303-6307.
59. S. Tsunekawa, R. Sivamohan, S. Ito, A. Kasuya, T. Fukuda, Nanostructured Materials, 11 (1999) 141-147.
60. S. Tsunekawa, R. Sahara, Y. Kawazoe, K. Ishikawa, Applied Surface Science, 152 (1999) 53-56.
61. L. Chen, P. Fleming, V. Morris, J. D. Holmes, M. A. Morris, The Journal of

Physical Chemistry C, 114 (2010) 12909–12919.

62. E. Aneggi, C. de Leitenburg, G. Dolcetti, A. Trovarelli, Catalysis Today, 114 (2006) 40-47.
63. R. J. Gorte, AIChE Journal, 56 (2010) 1126-1135.
64. R. Möller, M. Votsmeier, C, Onder, L. Guzzella, J. Gieshoff, Applied Catalysis B: Environmental, 91 (2009) 30-38.
65. T. Luo, R. J. Gorte, Catalysis Letters, 85 (2003) 139-146.
66. J. S. Hepburn, A. Dobson, H. S. Gandhi, SAE paper 942071 (1994).
67. C. Janvier, M. Pijolat, F. Valdivieso, M. Soustelle, C. Zing, Journal of the European Ceramic Society, 18 (1998) 1331-1337.
68. G. Colon, F. Valdivieso, M. Pijolat, R. T. Baker, J. J. Calvino, S. Bernal, Catalysis Today, 50 (1999) 271-284.
69. G. Colon, M. Pijolat, F. Valdivieso, R. T. Baker, S. Bernal, Adv. Sci. Tech. 16 (1999) 605.
70. J. P. Cuif, G. Blanchard, O. Touret, A. Seigneurin, M. L. Marczi, E. Quemere, SAE paper 970463 (1994).
71. M. Sugiura, M. Ozawa, A. Suda, T. Suzuki, T. Kanazawa, Bulletin of the Chemical Society Japan, 78 (2005) 752-767.
72. Y. Madier, C. Descorme, A. M. Le Govic, D. Duprez, The Journal of Physical Chemistry B, 103 (1999) 10999-11006.
73. T. Murota, T. Hasegawa, S. Aozasa, H. Matsui, M. Motoyama, Journal of Alloys and Compounds, 193 (1993) 298-299.
74. A. Trovarelli, F. Zamar, J. Llorca, C. de Leitenburg, G. Dolcetti, J. T. Kiss, Journal of Catalysis, 169 (1997) 490-502.
75. E. Finocchio, M. Daturi, C. Binet, J. C. Lavalley, F. Fally, V. Perrichon, H.

Vidal, J. Kaspar, M. Graziani, G. Blanchard, Studies in Surface Science and Catalysis, 121 (1999) 257.

76. G. Vlaic, P. Fornasiero, S. Geremia, J. Kaspar, M. Graziani, Journal of Catalysis, 168 (1997) 386-392.
77. S. Rossignol, C. Micheaud-Especel, D. Duprez, Studies in Surface Science and Catalysis, 130D (2000) 3327.
78. C. E. Hori, H. Permana, K. Y. S. Ng, A. Brenner, K. More, K. M. Rahmoeller, D. Belton, Applied Catalysis B: Environmental, 16 (1998) 105-117.
79. H. C. Yao, Y. F. Yu Yao, Journal of Catalysis, 86 (1984) 254-265.
80. P. Loof, B. Kasemo, K. E. Heck, Journal of Catalysis, 118 (1989) 339-348.
81. C. Descorme, Y. Madier, D. Duprez, Journal of Catalysis, 196 (2000) 167-173.
82. J. Kacimi, J. Barbier Jr., R. Taha, D. Duprez, Catalysis Letters, 22 (1993) 343-350.
83. R. K. Herz, J. B. Kiela, J. A. Sell, Industrial & Engineering Chemistry Research, 22 (1983) 387-396.
84. S. H. Oh, C. C. Eickel, Journal of Catalysis, 112 (1988) 543-555.
85. J. G. Nunan, H. J. Robota, M. J. Cohn, S. A. Bradley, Journal of Catalysis, 133 (1992) 309-324.
86. M. Fernandez-Garcia, A. Martinez-Arias, L. N. Salamanca, J. M. Coronado, J. A. Anderson, J. C. Conesa, J. Soria, Journal of Catalysis, 187 (1999) 474-485.
87. J. Barbier Jr, D. Duprez, Applied Catalysis B: Environmental, 3 (1993) 61-83.
88. M. Fernandez-Garcia, A. Martinez-Arias, A. Iglesias-Juez, A. B. Hungria, J. A. Anderson, J. C. Conesa, J. Soria, Applied Catalysis B: Environmental, 31 (2001) 39-50.
89. C. Serre, F. Garin, G. Belot, G. Maire, Journal of Catalysis, 141 (1993) 9-20.

90. P. Bera, K. C. Patil, V. Jarayam, G. N. Subbanna, M. S. Hedge, Journal of Catalysis, 196 (2000) 293-301.

91. D. J. M. Bevan, J. Kordis, Journal of Inorganic and Nuclear Chemistry, 26 (1964) 1509-1523.

92. P. Knappe, L. Eyring, Journal of Solid State Chemistry, 58 (1985) 312-324.

93. S. P. Ray, D. E. Cox, Journal of Solid State Chemistry, 15 (1975) 333-343.

94. M. Boaro, C. de Leitenburg, G. Dolcetti, A. Trovarelli, Journal of Catalysis, 193 (2000) 338-347.

95. R. Taha, D. Duprez, N. Mouaddib-Moral, C. Gauthier, Studies in Surface Science and Catalysis, 116 (1998) 549-558.

96. G. S. Zafiris, R. J. Gorte, Journal of Catalysis, 143 (1993) 86-91.

97. T. Bunluesin, E. S. Putna, R. J. Gorte, Catalysis Letters, 41 (1996) 1-5.

98. R. H. Nibbelke, M. A. J. Campman, H. B. J. Hoebink, G. B. Marin, Journal of Catalysis, 171 (1997) 358-373.

99. V. V. Pushkarev, V. I. Kovalchuk, J. L. d'Itri, The Journal of Physical Chemistry B, 108 (2004) 5341-5348.

100. P. J. Gellings, H. J. M. Bouwmeester, Catalysis Today, 58 (2000) 1-53.

101. J. L. Dubois, C. J. Cameron, Applied Catalysis A: General, 67 (1990) 49-71.

102. J. Haber, W. Turek, Journal of Catalysis, 190 (2000) 320-326.

103. J. H. Lunsford, Angewandte Chemie International Edition, 34 (1995) 970.

104. J. Soria, A. Martinez-Arias, J. C. Conesa, Journal of the Chemical Society, Faraday Translations, 91 (1995) 1669-1678.

105. X. Zhang, K. J. Klabunde, Inorganic Chemistry, 31 (1992) 1706-1709.

106. J. M. Rojo, J. Sanz, J. Soria, J. L. G. Fierro, Z Physik Chem NF, 152 (1987) 149-158.

107. A. Martinez-Arias, J. M. Coronado, J. C. Conesa, J. Soria, Rare Earths (R. Saez Puche and P. Caro eds.), Complutense, Madrid, 299-315, 1997.

108. Y. M. Choi, H. Abernathy, H. T. Chen, M. C. Lin, M. Liu, Chem Phys Chem, 9 (2006) 1957-1963.

109. H. Y. Li, H. F. Wang, X. Q. Gong, Y. L. Guo, Y. Guo, G. Z. Lu, P. Hu, Physical Review B, 79 (2009) 193401.

110. C. Janvier, M. Pijolat, F. Valdivieso, M. Soustelle, Solid States Ionics, 127 (2000) 207-222.

111. A. Bielanski, J. Haber, Oxygen in Catalysis: Chemical Industries, Vol 43 Marcel Dekker, New York, 132-139, 1991.

112. J. M. Thomas, W. J. Thomas, Principles and Practice of Heterogeneous Catalysis, VCH Publishers Inc., New York, USA, 1996.

113. L. De Rogatis, M. Cargnello, V. Gombac, B. Lorenzut, T. Montini, P. Fornasiero, ChemSusChem, 3 (2010), 24-42.

114. H. S. Taylor, Proc. R. Soc., A108 (1925) 105-111.

115. D. Thompson, Gold Bull. (London, U.K.), 32 (1999) 12-19.

116. M. Valden, X. Lai, D. W. Goodman, Science, 281 (1998) 1647-1650.

117. G. C. Bond, Gold Bull. (London, U.K.), 34 (2001) 117-119;

118. B. E. Salisbury, W. T. Wallace, R. L. Whetten, Chemical Physics, 262 (2000) 131-141.

119. D. Thompson, Gold Bull. (London, U.K.), 31 (1998) 111-118.

120. B. Coq, F. Figueras, Coordination Chemistry Review, (178-180) 1998 1753-1783.

121. C. R. Henry, Applied Surface Science, 164 (2000) 252-259.

122. M. Che, C. O. Bennett, Advances in Catalysis, 36 (1989) 55-172.

123.J. A. Farmer, C. T. Campbell, Science, 329 (2010) 933-936.

124.J.M. Campelo, D. Luna, R. Luque, J. M. Marinas, A. A. Romero, ChemSusChem, 2 (2009) 18-45.

125.K. M. K. Yu, D. Thompsett, S. C. Tsang, *Chem. Commun.* 2003, 1522-1523.

126.G. Budroni, A. Corma, Angewandte Chemie, 118 (2006) 3406-3409; Angewandte Chemie International Edition, 45 (2006) 3328-3331.

127.T. Montini, A. M. Condo, N. Hickey, F. C. Lovey, L. De Rogatis, P. Fornasiero, M. Graziani, Applied Catalysis B: Environmental, 73 (2007) 84-97.

128.P. Fornasiero, T. Montini, L. De Rogatis, in Diffusion and Reactivity Solids (Ed. J. Y. Murdoch), Nova Science Publishers, 65-109, 2007.

129.T. Montini, L. De Rogatis, V. Gombac, P. Fornasiero, M. Graziani, Applied Catalysis B: Environmental, 71 (2007) 125-134.

130.L. De Rogatis, T. Montini, M. F. Casula, P. Fornasiero, Journal of Alloys and Compounds, 451 (2008) 516-520.

131.C. J. Zhong, M. M. Maye, Advanced Materials, 13 (2001) 1507-1511.

132.F. Caruso, Advanced Materials, 13 (2001) 11-22.

133.G. A. Somorjai, R. M. Rioux, Catalysis Today, 100 (2005) 201-215.

134.R. W. J. Scott, O. M. Wilson, R. M. Crooks, Chemistry of Material, 16 (2004) 5682-5688.

135.H. Wu, Z. Liu, X. Wang, B. Zhao, J. Zhang, C. Li, Journal of Colloid Interface Science, 302 (2006) 142-148.

136.I. Pastoriza-Santos, D. S. Koktysh, A. A. Mamedov, M. Giersig, N. A. Kotov, L. M. Liz-Marzan, Langmuir, 16 (2000) 2731-2735.

137.T. Hirakawa, P. V. Kamat, Journal of the American Chemistry Society, 127 (2005) 3928-3934.

138. N. L. V. Carreno, E. R. Leite, E. Longo, P. N. Lisboa-Filho, A. Valentini, L. F. D. Probst, W. H. Schreiner, Journal of Nanoscience and Nanotechnology, 2 (2002) 491-494.

139. N. L. V. CarreÇo, A. R. C. Lima, A. L. E. B. Soledade, A. E. Longo, A. E. R. Leite, A. Barison, B. A. G. Ferreira, A. Valentini, L. F. D. Probst, Journal of Nanoscience and Nanotechnology, 3 (2003) 516-520.

140. C. M. Y. Yeung, S. C. Tsang, The Journal of Physical Chemistry C, 113 (2009) 6074-6087.

141. C. M. Y. Yeung, S. C. Tsang, Catalysis Letters, 128 (2009) 349-355.

142. C. M. Y. Yeung, F. Meunier, R. Burch, D. Thompsett, S. C. Tsang, The Journal of Physical Chemistry B, 110 (2006) 8540-8543.

143. C. M. Y. Yeung, K. M. K. Yu, Q. J. Fu, D. Thompsett, M. I. Petch, S. C. Tsang, Journal of the American Chemistry Society, 127 (2005) 18010-18011.

CHAPTER 2

EXPERIMENTAL

2.1 Introduction 52

2.2 Catalysts Preparation 53

2.2.1 Ceria Modified Ni Catalysts 54

2.2.2 Pure Ceria Nanoparticles 55

2.2.3 Platinum Modified Ceria 56

2.3 Catalyst Characterization 58

2.3.1 X-ray Diffraction (XRD) 58

2.3.2 Electron Microscopy (EM) 62

2.3.3 X-ray Photoelectron Spectroscopy (XPS) 68

2.3.4 Temperature Programmed Reduction (TPR) 70

2.3.5 Electronic Paramagnetic Resonance (EPR) 72

2.3.6 Fourier Transform Infrared Spectroscopy (FTIR) 75

2.3.7 Diffuse Reflectance Fourier-Transform Spectroscopy (DRIFTS) 77

2.3.8 Thermo-Gravimetric Analyzer (TGA) 78

2.3.9 Raman Spectroscopy 79

2.4 Catalytic Testing 82

2.4.1 Methane Steam Reforming (MSR) 82

2.4.2 Hydrogenolysis of Glycerol 85

2.5 References 89

2.1 Introduction

In this chapter, catalyst preparation methods and procedures will be introduced. This includes a detailed description of the preparation of ceria modified commercial Ni catalysts prepared by deposition precipitation and sol-gel methods, pure nano ceria particles with different sizes by the microemulsion method, and Pt doped ceria materials by microemulsion, co-microemulsion, and wet-grinding methods. The characterization techniques performed on these prepared catalysts will be addressed in terms of principles and experimental methods. Finally, catalytic testing facilities and analytical methods used to probe the methane steam reforming reaction and glycerol hydrogenolysis reaction are described.

2.2 Catalysts Preparation

2.2.1 Ceria Modified Ni Catalysts

The catalyst 65%Ni/SiO_2/Al_2O_3 (NSA) was bought from Aldrich with a 65% nickel loading and a surface area of 190 m^2/g. Four samples, namely NSAC-CN, NSAC-CNP, NSAC and NSAC-M2 constitute ceria modified NSA samples.

2.2.1.1 Deposition Precipitation

NSAC-CN and NSAC-CNP were ceria modified NSA samples produced by the deposition precipitation method with the molar ratio (Ce/Ni) of 1/2. Typically NSAC-CN was synthesized by first placing 4.25 g NSA in 100 mL distilled water with constant stirring at 200 rpm in a beaker. A pH meter was then inserted into the vessel followed by adding a precursor solution containing 1.94 mL of water-soluble cerium (IV) nitrate (prepared in 20 mL distilled water and 0.5 g of nitric acid such that Ce (IV) existed as a negatively charged complex). A solution containing 0.5 M sodium carbonate was then added dropwise to the mixture until precipitation occurred within the catalytic pores, usually at pH 7.5 ± 0.5. The mixture was filtered using Whatman 540 (90 mm) filter paper and the solid obtained was washed several times with distilled water to remove the sodium ions (derived from the base). Finally, the material was dried at 105 ^oC for 4 h and then calcined at 500 ^oC for 2 h. The

NSAC-CNP sample was synthesized using a similar procedure as previously described but with the co-addition of 20 g of 5 wt% solution of a co-polymer of acrylamide and the methyl chloride quaternary salt of 2-(dimethylamino)ethyl acrylate (alkalized with a few drops of 35% ammonia solution) prior to addition of sodium carbonate solution. These polymer species are known to be strongly adsorbed onto the solid oxide support by the electrostatic attraction between the positively charged quaternary ammonium groups of the adsorbate and the negatively charged surface silanol groups at the support. The presence of an excess of quaternary ammonium groups imparts an overall positive charge to the polymer-covered support surface. Hence this polymer reversed charge pre-treatment [1] is expected to be more effective at attracting the negatively charged complex of Ce (IV).

2.2.1.2 Sol-gel

Two samples, namely NSAC and NSAC-M2, were synthesized by a modified sol-gel method. Typically, for the NSAC synthesis, 0.5 g NSA was mixed with 1.2g Ce (IV) isopropoxide (Sigma-Aldrich) which was pre-dissolved in 5.5 mL pyridine (A.R.). 5 mL water was then gradually added into the mixture (the molar ratio of Ce/Ni was set at 1/2). The mixture was stirred at room temperature for 24 hrs before being centrifuged (× 1000 rpm) for 20 min. The supernatant liquid was decanted and the residue was washed with ethanol four times undergoing centrifuge treatment between each washing. Finally, the solid product was left to dry overnight and

calcined in air prior to being gently ground to a powdered form. Similarly, NSAC-M2 was synthesized with the same procedure but using the molar ratio of Ce/Ni of 2/1.

2.2.2 Pure Ceria Nanoparticles

The ceria nanoparticles (MCE) were synthesized based on a modified microemulsion method reported by Masui *et al* [2]. One microemulsion containing 1-10 g aqueous phase solutions (0.025 M to 0.5 M) of cerium (III) nitrate hexahydrate (sigma-aldrich) was prepared. 29g/58g organic solvent (n-Heptane, > 99%, Fisher) was used to yield different water to oil ratios. 19g/38g Triton® X-100 (Aldrich) and 15g/30g 1-hexanol (> 99%, Aldrich) were included as a surfactant and co-surfactant, respectively. Another microemulsion, which contained 5 g tetramethylammonium hydroxide pentahydrate (25 wt.-% in water, Sigma-Aldrich), with 29g/58g n-Heptane, 19g/38g Triton® X-100 and 15g/30g 1-hexanol, was prepared separately. Each microemulsion was stirred for 4 hrs to ensure the mixture was homogenous.

In the second stage, both microemulsions were mixed together, and then stirred at 40 ^{o}C for 24 h. After 24 h, the liquid was centrifuged, decanted and the resulting precipitate rinsed thoroughly (four times) with ethanol. The solid obtained was first dried at room temperature, then at 80 ^{o}C for another 24 h and finally calcined in air for 2 h at 500 ^{o}C using a 2 ^{o}C/min ramp. The final samples are designated as MCE-x. The samples were kept in nitrogen filled dry box after calcinations in order to reduce contamination by the carbonate phase formed from the reaction with carbon dioxide

in the air.

2.2.3 Platinum Modified Ceria

2.2.3.1 Microemulsion

The MPC samples (microemulsion prepared Pt/CeO_2 samples) were synthesized by a similar technique as the MCE samples.

A Pt doped ceria sample namely MPC02 (1.25 at.-% Pt/ceria), was synthesized by the following method: One microemulsion containing 1 g aqueous phase solutions containing appropriate amount of $(NH_4)_2Pt(NO_3)_6$ (Sigma-Aldrich) was prepared in 29 g n-Heptane, 19 g Triton® X-100 and 15 g 1-hexanol and stirred for 4 h, 1 g 0.1 M sodium borohydride aqueous solution was added and stirred for another 2 hrs to form Pt^0 before adding 5 g 1 M cerium (III) nitrate hexahydrate. After the mixture was stirred overnight, 5 g tetramethylammonium hydroxide pentahydrate (25 wt.-% in water) was added and the reaction mixture was aged for 6 days with constant stirring. After the aging step, the reaction mixture was centrifuged to collect the product. The product was then washed with an EtOH/DI water mixture and centrifuged at least four times to remove any surfactant and sodium salts. The solid product obtained was dried in the air and then in an oven at 80 ^oC overnight.

2.2.3.2 Co-microemulsion

Another Pt doped ceria sample namely MPC06 (1.25 at.-% Pt/ceria), was prepared by the similar co-microemulsion technique as reported [3]. One microemulsion containing 1 g aqueous phase solutions with the appropriate amount of $(NH_4)_2Pt(NO_3)_6$ (Sigma-Aldrich) was prepared in 29 g n-Heptane, 19 g Triton® X-100 and 15 g 1-hexanol and stirred for 4 h. 0.22 g sodium hydroxide predissolved in 5.78 g DI water was then added and stirred for another 2 h before adding 5 g 1 M cerium (III) nitrate hexahydrate. The reaction mixture was aged for 6 days with constant stirring. Then the mixture was centrifuged, washed with an EtOH/DI water mixture and dried in the air and then in the oven. MPC09 (0.4 wt.-% Pt/ceria) was synthesized by the same method with 1 g aqueous solution containing reduced amount of $(NH_4)_2Pt(NO_3)_6$.

2.2.3.2 Wet-grinding

One more Pt doped ceria sample, namely PC03 (1.25 wt.-% Pt/ceria), was prepared by the following wet-grinding method: The commercial nano ceria (Johnson Matthey, namely JMCE) and $(NH_4)_2Pt(NO_3)_6$ solution were mixed together. Then a stoichiometric quantity of sodium borohydride was added to the Pt aqueous solution to form Pt^0. The solution was stirred overnight, and then dried by heating up to 80 ^oC in air, and finally calcined in air for 2h at 500 ^oC using 2 ^oC/min ramp.

2.3 Catalyst Characterization

Many different techniques have been used to probe the redox state of ceria and related oxide systems both in the presence and absence of a supported metal phase: EM (SEM, TEM, EDX, SAED), EPR, XPS, FTIR spectroscopy and chemical techniques including temperature programmed reduction (TPR). All these techniques provide interesting pieces of information, fitting together to build an accurate description of the system.

2.3.1 X-ray Diffraction (XRD)

2.3.1.1 Aim

X-ray diffraction (XRD) is routinely used in heterogeneous catalysis as X-ray diffraction patterns reveal the identity and crystallite size. In addition, because XRD patterns yield *d*-spacing and unit cell information, an insight into the atomic constituents of the species can be obtained [4].

2.3.1.2 Principle [5]

An X-ray diffractometer consists of an X-ray generator, a goniometer, a sample holder and an X-ray detector. The most commonly employed instruments to generate

X-rays are X-ray tubes, which generate X-rays by bombarding a metal target with high electron energy (10 - 100 keV) that knock out core electrons.

When an X-rays beam strikes an ordered crystal surface at the angle θ, a portion is elastically scattered by the electrons of the layer of atoms at the surface. The non scattered portion of the beam penetrates to the second layer of atoms where again a fraction is scattered, and the remainder passes on to the third layer and so on. The requirements for X-ray diffraction are: a) The scattering centres must be spatially distributed in a highly regular way; b) The spacing between layers of atoms must be roughly the same as the wavelength of the radiation.

In 1912, W.L. Bragg treated the diffraction of X-rays by crystals as shown in Figure 2.1.

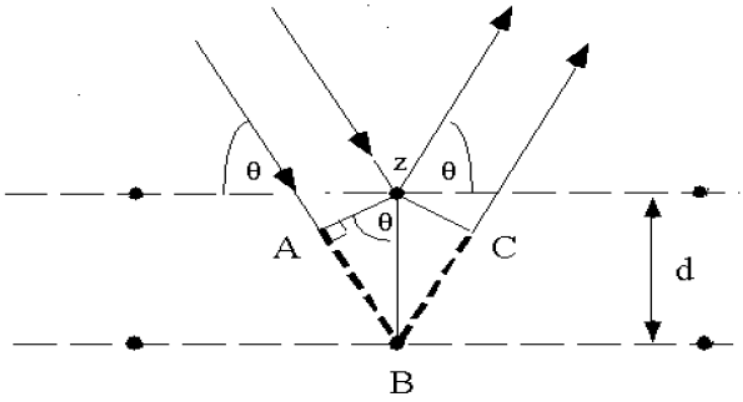

Figure 2.1 Diffraction of X-rays by a crystal

Bragg's Law:

A narrow beam of radiation strikes the crystal surface at angle θ; scattering occurs as a consequence of interaction of the radiation with the electrons of atoms

located at *Z* and *B* (Figure 2.1). If the distance:

$$AB + BC = n\lambda \qquad (2.1)$$

where n indicates the order of the reflection and λ is the X-ray wavelength. The scattered radiation will be in phase at *ZC*, and the crystal will appear to reflect the X-radiation.

$$AB = BC = d\sin\theta \qquad (2.2)$$

d is the interplanar distance of the crystal. Therefore, the conditions for the constructive interference of the beam at angle are

$$n\lambda = 2\, d\sin\theta;\ n = 1,2,\ldots \qquad (2.3)$$

The equation 2.3 is called *Bragg's equation*. X-rays appear to be reflected from the crystal only if the angle of incidence satisfies the condition that

$$\sin\theta = n\lambda/2d \qquad (2.4)$$

At all different angles, destructive interference occurs.

For diffraction in very small crystals, diffraction lines become broader as the

crystal size decreases. As Bragg's law gives the condition for constructive interference, at θ values slightly higher than the Bragg angle, each plane gives a "lag" in the diffracted beam. For many planes, this ends up cancelling out and thus the net diffraction is zero. In small crystals, there are relatively fewer planes, so there is a "remanent" diffraction. This phenomenon provides an experimental method for determine the average particle size by the Scherrer equation reported below:

$$t = K\lambda/\beta\cos\theta_B \qquad (2.5)$$

where β is the full width at the half maximum (FWHM) of the peak, t is thickness of the crystal in the direction perpendicular to the diffracting planes, θ_B is the Bragg angle and K is a constant. Micro or nano crystallites give diffraction peaks which are broadened because there are fewer planes producing a particular Bragg diffraction, hence the destructive interference is not complete [6]. From X-ray diffraction data the crystal structure of a compound can be refined using Rietveld method. This is a widely recognized structural analysis technique in powder crystallography. XRD cannot typically detect crystallites with a size below 2 nm [7].

2.3.1.3 Experiments

Powder XRD patterns were recorded on a Siemens D5000 high-resolution X-ray powder diffractometer using Cu$K\alpha$ radiation. And the phase identification of catalysts

was carried out by comparing the collected diffraction patterns with the published files from the International Centre for Diffraction Data (JCPDS-1996). The particle size and distribution were determined by the Scherrer equation from the most intense XRD peaks and instrumental peak broadening has been taken into account using a crystal of silicon as a reference. Also, the collected XRD data of pure ceria samples were analyzed and refined by Rietveld method using data up to 125 degree in 2θ.

2.3.2 Electron Microscopy (EM)

2.3.2.1 Aim

Electron Microscopy is a primary analytical tool for the direct observation, manipulation and understanding of the building blocks of material. It reveals the surface topology of the heterogeneous catalyst and also plays an important role in determining the size of the metal particles in order to study any size effects on the catalytic reaction. When coupled with some spectroscopic and diffraction techniques it can give a greater understanding of the chemical composition on the surface of the catalyst system leading to a complete picture of a sample both locally and as a bulk [8].

2.3.2.2 Transmission Electron Microscopy (TEM)

TEM is the best technique for directly investigating the local structure and chemical environment of heterogeneous catalysts at the atomic scale, for example, to determine if the particles are supported or to provide information to whether there is sufficient contrast between particles and the support. It is also used to determine the particle size and distribution, and it is even possible to learn about the defect structure of oxide lattices (HRTEM) [9].

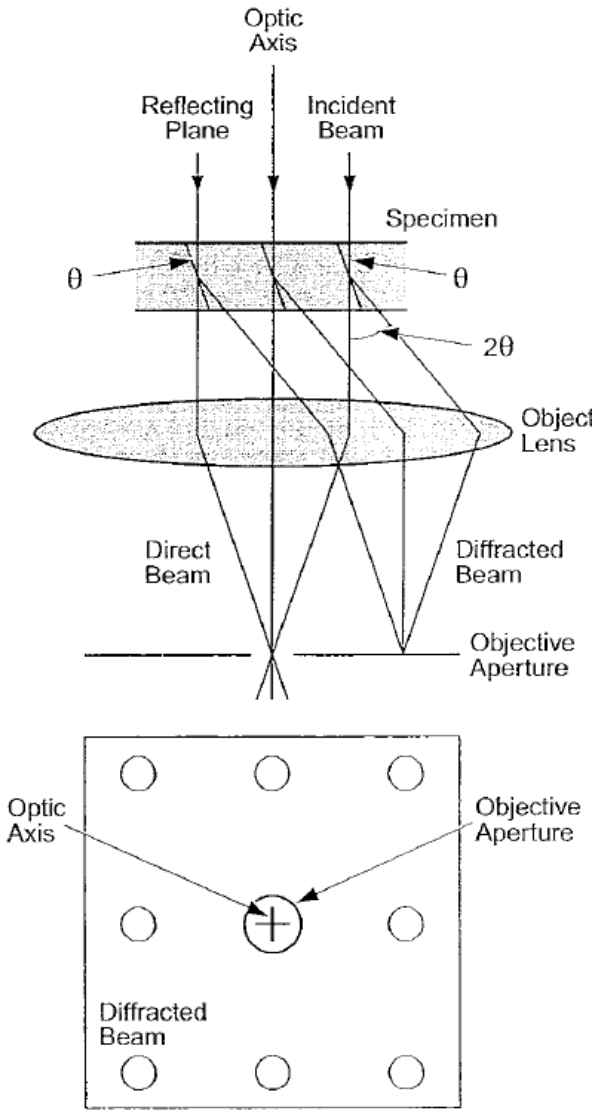

Figure 2.3 TEM image diagram [9]

In TEM (Figure 2.3), electrons are accelerated to high velocity by a series of accelerating plates and then transmitted through the sample. Normally the incident and scattered electrons are referred to as electron beams. The electrons are generated by an electron gun and focused under electromagnetic lenses, with the condenser and the objective, to form the image of the sample. Then other lenses in the system magnify the image. The unscattered and scattered electrons are focused with the objective lenses in the back-focal plane where the diffraction pattern is formed. After passing through this plane the scattered and unscattered waves interfere to form an intermediate image plane. The projection lenses are focused either on the diffraction pattern or on the intermediate image to give the final diffraction pattern or image on a fluorescent screen. The image is a projection of the structure on the plane perpendicular to the electron beam.

2.3.2.3 Scanning Electron Microscopy (SEM)

The scanning electron microscope (SEM) is one of the most widely used electron beam instruments. The main difference between SEM and TEM is that SEM sees contrast due to topology and composition of the surface of a sample, whereas the electron beam in the TEM projects all information on the mass it encounters in a two dimensional image of sub-nanometre resolution.

2.3.2.4 Energy Dispersion X-ray Spectroscopy (EDX)

Energy dispersive X-ray spectroscopy (EDX) is an analytical tool for chemical characterization, typically coupled with electron microscopy [9]. Each element of the periodic table has a unique electronic structure and, therefore, a unique response to electromagnetic waves. When an element is bombarded with an electron beam, the specimen will release some of the absorbed energy as X-rays. Much of the time, the energy is the result of changes in the speed of an electron, which is random; however, when this interaction removes an electron from a specimen's atom, frequently a vacancy in the inner electron shell appears. In order to return the atom to its normal state, an electron from an outer atomic shell "drops" into the vacancy in the inner shell. This drop results in the loss of a specific amount of energy, namely, the difference in energy between the vacant shell and the shell contributing the electron. This energy is given up in the form of X-rays. Since energy levels in all elements are element-specific, the X-rays generated have energies which are also element specific. Energy dispersive X-ray microanalysis uses detection equipment to measure the energy values of the characteristic X-rays generated within the electron microscope. Using semiconductor material (typically, Si/Li single crystal) to detect the X-rays and a multi-channel analyzer, an X-ray microanalysis system converts X-ray energy into an electronic count. The accumulation of these energy counts creates a spectrum representing the chemical analysis of the sample.

2.3.2.5 Selected Area Electron Diffraction (SAED) [10, 11]

Selected area electron diffraction (SAED) is a crystallographic experimental technique which can be performed inside a TEM. In a TEM, a thin crystalline specimen is subjected to a parallel beam of high-energy electrons. As TEM specimens are typically ~100 nm thick, and the electrons typically have an energy of 100 - 400 kV, the electrons pass through the sample easily. In this case, electrons are treated as wave-like, rather than particle-like. Because the wavelength of high-energy electrons is a fraction of a nanometre, and the spacing between atoms in a solid is only slightly larger, the atoms act as a diffraction grating to the electrons, which are diffracted. That is, some fraction of them will be scattered to particular angles, determined by the crystal structure of the sample, while others continue to pass through the sample without deflection. As a result, the image on the screen of the TEM will be a series of spots - the selected area diffraction pattern (SADP), each spot corresponding to a satisfied diffraction condition of the sample's crystal structure. If the sample is tilted, the same crystal will stay under illumination, but different diffraction conditions will be activated, and different diffraction spots will appear or disappear.

SAED is referred to as "selected" because the user can easily choose from which part of the specimen to obtain the diffraction pattern. Located below the sample holder on the TEM column is a selected area aperture, which can be inserted into the beam path. This is a thin strip of metal that will block the beam. It contains several different sized holes, and can be moved by the user. The effect is to block all the

electron beam except for the small fraction passing through one of the holes; by moving the aperture hole to the section of the sample the user wishes to examine, this particular area is selected by the aperture, and only this section will contribute to the SADP on the screen. As a diffraction technique, SAED can be used to identify crystal structures and examine crystal defects.

2.3.2.6 TEM, SEM, EDX and SAED Experiments

In Chapter 3, the TEM experiment was carried out using a Phillips CM20 microscope operating at 200 kV. Elemental analysis was conducted using Stereoscan S360 digital scanning electron microscope with elemental analysis by Oxford Instrument EDS6767 energy-dispersive X-ray analyzer (EDX). The sample was gently ground, suspended in 2-propanol, and placed on a carbon-coated copper grid after the evaporation of the solvent. Electron micrographs and EDX analyses of selected areas were taken.

In Chapter 4 and Chapter 5, a JEOL JEM-3000F working at 300 kV carried out the TEM experiments. The crystal structure was examined by selected area electron diffraction (SAED) patterns, which were recorded by a 1k × 1k CCD camera. The lattice constants were then carefully calculated from SAED patterns. In order to achieve this, it is essential to calibrate the experimental patterns with the known diffraction pattern. This was achieved by setting up a protocol of constant lens settings for the microscope, which enabled the calibration against an Au

polycrystalline sample maintained to a high accuracy. By labelling the Au diffraction rings with the corresponding Au (111), (200), (220) and (311) planes, we obtained the scattering radian per pixel on the CCD screen. This value was used to calculate the scattering angles for various MCE planes of their SAED patterns (results in Chapter 4), and the reciprocal of the scattering angle corresponds to the interplane spacing, from which the lattice constants were deduced.

2.3.3 X-ray Photoelectron Spectroscopy (XPS)

2.3.3.1 Aim

XPS technique was used to determine the element compositions on the surface of catalysts and the oxidation states.

2.3.3.2 Principle [9]

X-ray photoelectron spectroscopy (XPS) is one of the most versatile techniques based on the photoelectric effect, in which an atom absorbs a photon of energy $h\upsilon$, therefore a core or valence electron with binding energy E_B is ejected with kinetic energy of emitted photoelectrons (E_K). The relationship between the energies and the energy of the incoming X-ray photon energy ($h\upsilon$) is shown below:

$$E_K = h\upsilon - E_B + \Phi \qquad (2.6)$$

where Φ is the work function of the spectrometer.

By convention, the binding energy of a core level electron is measured with the respect to the highest occupied level of solid, the Fermi level. Figure 2.4 show the XPS summarizing process. The total energy available to excite a core electron is clearly equal to the photon energy. However, some of the photon energy must be consumed in overcoming the potential energy barrier, associated with the attraction of the electron for the nucleus.

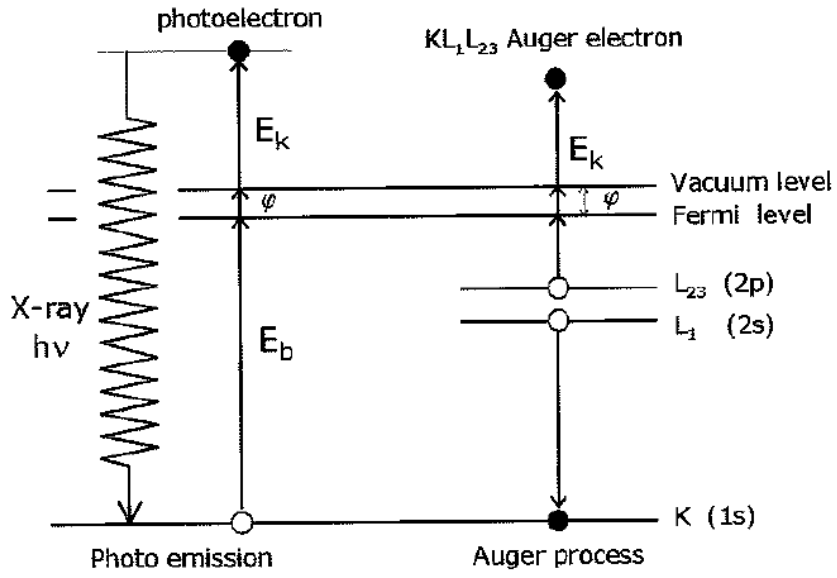

Figure 2.4 X-ray excitation of a 1s core level [9]

The remaining energy is transformed into the kinetic energy of the photo-emitted electrons. It is clear that for the fixed photon energy, photoemission will produce photoelectrons with well-defined kinetic energies varying systematically from

element to element due to the presence of element specific well-defined core levels [12].

2.3.3.3 Experiments

The nano ceria powders - MCE samples (Chapter 4) were attached to the sample holder using conductive carbon tape. The XPS experiment was performed in a VG Microtec ion pumped XPS system equipped with a nine-channel CLAM4 electron energy analyzer. The exciting radiation used in the studies was for the monochromatised aluminium Kα radiation in a 650 μm spot at 200 W power. Charge compensation was activated, provided by the in-lens flood gun at a 2 eV setting and the 401 argon ion flood source at a "zero energy" setting. Sensitivity factors after Scofield [13] were used in quantification. The energy scale reference used was the maximum of the carbon 1*s* peak: this was set to 285 eV.

2.3.4 Temperature Programmed Reduction (TPR)

2.3.4.1 Aim

Temperature programmed reduction (TPR) is a widely used technique in the study of supported and unsupported catalysts. TPR gives information on the reducibility of oxide species by heating the sample under a flow of a H_2 containing

gas.

2.3.4.2 Principle

The TPR technique is based on the precise measurement of the amount of hydrogen consumption in the reduction of the oxide species from which it is possible to glean both the quantity and the availability of various reducible species in the sample, depending on the oxidative species peaks and the related area. The factors may vary with catalysts preparation and pre-treatment, and therefore this technique plays an important role in catalyst characterizations [14]. A TPR experiment consists of holding a sample in a programmable furnace that can increase the temperature linearly while a reducing gas mixture, usually hydrogen in nitrogen or argon, is passed over the sample. Sites of different reactivity will react differently with the hydrogen gas as the temperature is increased. Because the hydrogen has been used for the reduction process, it is convenient to measure the uptake of hydrogen by difference in the thermal conductivity of the gas before and after reduction. This change is recorded using a Thermal Conductivity Detector (TCD), and is displayed as a series of peaks plotted against temperature and time.

2.3.4.3 Experiments

The H_2-TPR was carried out in CE Instrument TPD/R/O1100 using 5% H_2/Ar as

the reducing agent with a flow rate of 20 mL/min. The sample was weighed carefully and accurately to ± 0.1 mg and then filled in a quartz tube with a pre-treatment in a flowing stream of helium at room temperature for 30 min. After that, the carrier gas was switched to 5% H_2/Ar before the sample was ramped from room temperature to 1000 ^{o}C at 10 ^{o}C / min without further optimization for any peak differentiation. The consumption of hydrogen was calculated based on calibration using a standard sample (CuO).

2.3.5 Electronic paramagnetic resonance (EPR)

2.3.5.1 Aim

EPR has matured into a powerful, versatile, nondestructive, and nonintrusive analytical method. Unlike many other techniques, EPR yields meaningful structural and dynamical information, even from ongoing chemical or physical processes without influencing the process itself.

2.3.5.2 Principle [15]

In EPR spectroscopy the difference in energy levels is predominately due to the interaction of unpaired electrons in the sample with a magnetic field produced by a magnet in the laboratory, this effect is called the Zeeman effect. Because the electron

has a magnetic moment, it acts like a compass or a bar magnet when you place it in a magnetic field, B_0. It will have a state of lowest energy when the moment of the electron, μ, is aligned with the magnetic field and a state of highest energy when μ is aligned against the magnetic field. The two states are labelled by the projection of the electron spin, Ms, on the direction of the magnetic field. Because the electron is a spin 1/2 particle, the parallel state is designated as $M_s = - 1/2$ and the antiparallel state is $M_s = + 1/2$.

From quantum mechanics, we obtain the most basic equations of EPR:

$$E = g \mu_B B_0 M_s = \pm 1/2 \, g \mu_B B_0 \qquad (2.7)$$

and

$$\Delta E = h\nu = g \mu_B B_0 \qquad (2.8)$$

g is the g-factor, which is a proportionality constant approximately equal to 2 for most samples, but varies depending on the electronic configuration of the radical or ion. μ_B is the Bohr magneton, which is the natural unit of electronic magnetic moment.

As varying the magnetic field strength can change the energy differences between the two spin states, there is an alternative means to obtain spectra. A constant magnetic field is applied and frequency of the electromagnetic radiation is scanned as in conventional spectroscopy. Alternatively, the electromagnetic radiation frequency

constant is kept and the magnetic field is scanned. A peak in the absorption will occur when the magnetic field "tunes" the two spin states so that their energy difference matches the energy of the radiation. This field is called the "field for resonance". Owing to the limitations of microwave electronics, the latter method offers superior performance.

The field for resonance is not a unique "fingerprint" for identification of a compound because spectra can be acquired at several different frequencies. The g-factor,

$$g = h\nu/\mu_B B_0 \qquad (2.9)$$

being independent of the microwave frequency, is much better for that purpose. Measurement of g-factors can give us some useful information; however, it does not tell us much about the molecular structure of our sample.

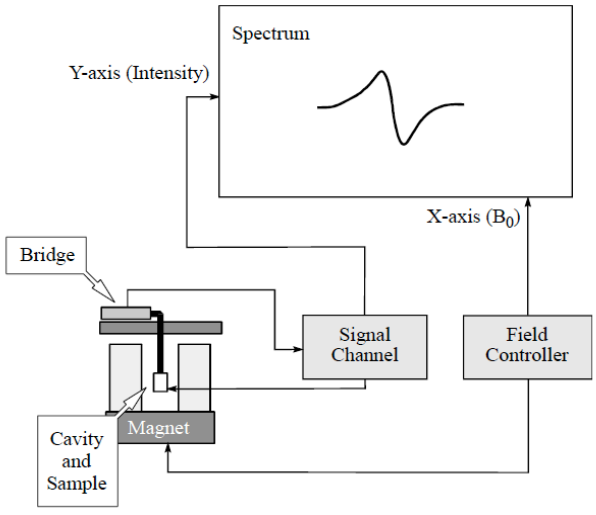

Figure 2.5 Diagram of an EPR spectrometer [15].

2.3.5.3 Experiment

X-band CW EPR spectra were recorded at room temperature on a Bruker EMX spectrometer using an Elexsys high sensitivity probehead. Cerium oxide samples, without the pre-treatment, were prepared in 4 mm tubes and weighed carefully to an accuracy of 0.01 mg.

Calculation of the spin number was based on a powder sample of Cu(II)TPP with a molar mass of 677.5 g and 1 spin per molecule. The CW EPR signal intensity *vs* electron spin number was obtained from the double integral of the spectrum. Ceria samples were weighed to an accuracy of 0.01mg. The CW EPR signal intensity of the broadened peak from the pure ceria samples with particle sizes smaller than 5.1 nm (Chapter 4) were also calculated from the double integral, enabling the number of spins per gram of ceria to be determined. All calibration measurements were made with a microwave power of 5.02 mW, modulation amplitude of 2.00 G, and 100 kHz modulation frequency.

2.3.6 Fourier Transform Infrared Spectroscopy (FTIR) [9]

2.3.6.1 Aim

FTIR is a technique for surface analysis of the types of reactive sites present on

the surface of a catalyst. Here it is used to investigate the formate species adsorption on the catalysts surface.

2.3.6.2 Principle

Infrared spectroscopy is based on absorption of infrared radiation exciting the bonds in the sample from one vibrational energy state to another higher vibrational energy state. Consequently, the infrared spectrum shows a set of absorption bands whose intensity and frequency provides information on the structure and bonding in the molecules. FTIR instruments employ interferometer techniques in the collection of spectral information, and the spectrum is calculated as an inverse Fourier transform of the interferogram. The improved sensitivity of FTIR instrumentation coupled with specialised techniques such as reflection-absorption spectroscopy and diffuse reflectance spectroscopy has remarkably improved its versatility for surface analysis. FTIR spectroscopy is non-destructive, structural specific and unlike high vacuum techniques is able to provide spectral information about solid/liquid or solid/gas interface in-situ. Absorption signals of the order 10^{-4} to 10^{-2} A are typically detected in surface analysis, hence special sensitivity requirements must be set for FTIR instruments applied to surface analysis.

2.3.6.3 Experiment

The IR spectra were acquired on a Nicolet 6700 FT-IR spectrometer with a liquid-nitrogen-cooled MCT detector. A drop of the test sample (Chapter 5) dispersed in 1 mL of 0.5 M aqueous formic acid solution was placed on smart golden gate-ZeSe/diamond crystal surface and evaporated at room temperature before recording the FT-IR spectra. The IR spectra were obtained by averaging 128 scans with a resolution of 4 cm^{-1}.

2.3.7 Diffuse Reflectance Fourier-Transform Spectroscopy (DRIFTS)

2.3.7.1 Aim and Principle

DRIFTS is a powerful technique for infrared analysis of fine particles and powders. It also allows the ability to measure surface species on a catalytic species.

2.3.7.2 Experiment

The DRIFTS of CO adsorption was measured at room temperature (Chapter 3). The material was first brought up to the reaction temperature under Argon and then switched to 2% CO to in Ar prior to their hydrogen pre-reduction at 800^{o}C. This DRIFTS reduction procedure was deliberately chosen so that the conditions were

comparable to those tested catalysts that had been explored to this high temperature and in the presence of hydrogen (product gas). A reference DRIFTS single scan was then recorded as a background. The reaction mixture (typically 2% CO in Ar) was subsequently introduced at a total flow rate of 100 ml/min. Stable DRIFTS signals were reached in less than 30 min (steady state conditions were achieved in terms of the concentrations of the surface species). The IR data are reported as log 1/*R*, with *R* = I/I_0, where *R* is the sample reflectance, I_0 is the intensity measured on the sample after exposure to 7% water, and *I* is the intensity measured under reaction mixture. It is found that the function log 1/*R* (= "absorbance") gives a better linear representation of the band intensity against the sample surface coverage than that given by the Kubelka–Munk function for strongly absorbing media [16-18].

2.3.8 Thermo-gravimetric Analyzer (TGA)

2.3.8.1 Aim and Principle

Thermo-gravimetric analysis measures the change in weight of a sample as it is heated up at a known rate. It was used here in order to elucidate the percentage of organic surfactant present on the surface of nanoparticles synthesised through the polyol process. It also gave an idea of whether the stabiliser remained on the metal surface under the reaction conditions.

2.3.8.2 Experiment

In terms of assessment for rate of carbon deposition (Chapter 3), the reactor with sample around 10 mg was flushed with reaction gas (Gas mixture: 2% methane/N_2 with the flow rate of 60 mL/min. Balance flow was 40 mL/min and the furnace flow was 20 mL/min) for 30 min at RT, and then the sample was heated from RT to 800 ℃ at ramp rate of 30 ℃ / min under the reaction gas. The sample temperature was kept at 800 ℃ for 900 min with the same reaction gas flow. All the experiments were performed and the data was collected by the equipment TGA Q50.

2.3.9 Raman Spectroscopy [19]

2.3.9.1 Aim

Raman spectroscopy is used in heterogeneous catalysis for investigation of supported and unsupported metals and oxides. This technique can be used as a probe of surface species and as a source of information about the level of disorder in crystal lattices.

2.3.9.2 Principle

Raman spectroscopy deals with vibrational phenomena in materials, just like

infrared (IR) spectroscopy but with somewhat different selection rules. Whereas allowed transitions in IR have a change of dipole moment, a Raman active transition requires a change in polarizability of the bonds caused by either ultraviolet, visible or near-IR light. If a molecule is irradiated by a monochromatic light of frequency v (laser), the light of frequency v (Rayleigh scattering) as well as that of frequency $v \pm v_i$ (Raman scattering) is scattered where v represents the vibrational frequency of the molecule. Therefore, Raman spectra are presented as shifts from the incident frequency in the ultraviolet, visible and near IR region.

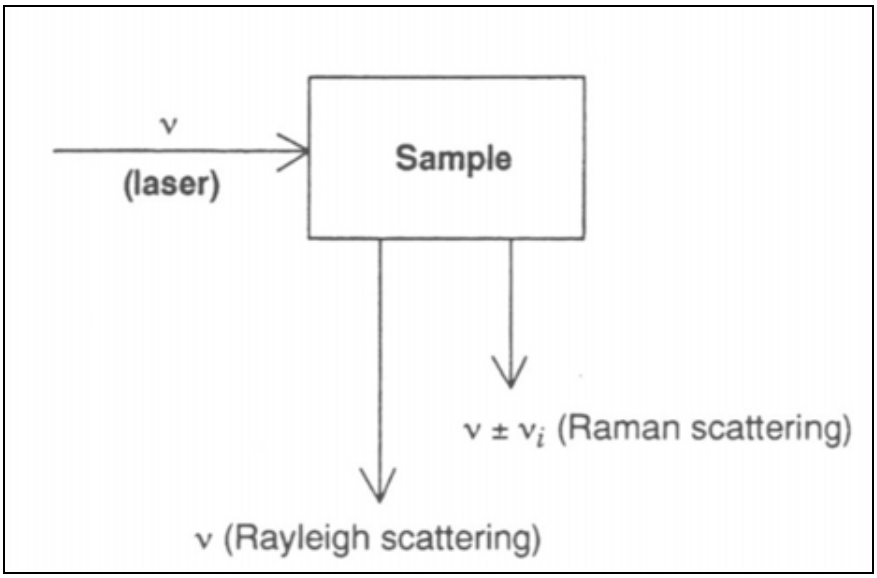

Figure 2.6 Mechanism of Raman scattering.

2.3.9.3 Experiment

The Raman spectra of the ceria powder samples (Chapter 4) were recorded using a Jobin Yvon spectrometer equipped with a microscope, through a 50 fold

magnification objective (Olympus company), by combining four spectra with collection times of 10 seconds each. A 20 mW He-Ne laser (632.8 nm) was used, and the 1800 L mm^{-1} grating provides a resolution starting from 1.0 cm^{-1} at 200 cm^{-1} up to 0.5 cm^{-1} at 3600 cm^{-1}. The abscissa was calibrated with the 520.7 cm^{-1} peak of silicon standard, and the sharp Raman shifts were accurate within the limits of the resolution. For Pt doped ceria samples (Chapter 5), Raman spectra were performed between 200 and 1200 cm^{-1} using a Perkin Elmer Raman Station 400 with a near-IR laser of 785 nm.

2.4 Catalytic Testing

2.4.1 Methane Steam Reforming (MSR)

As shown in Scheme 2.1, the experimental setup employed in MSR reaction consisted of: (a) a gas unit (containing N_2 and CH_4 cylinders and a mass controller), (b) a steam generator, (c) a gas pre-heater, (d) a tubular reactor, and (e) a gas chromatograph (GC).

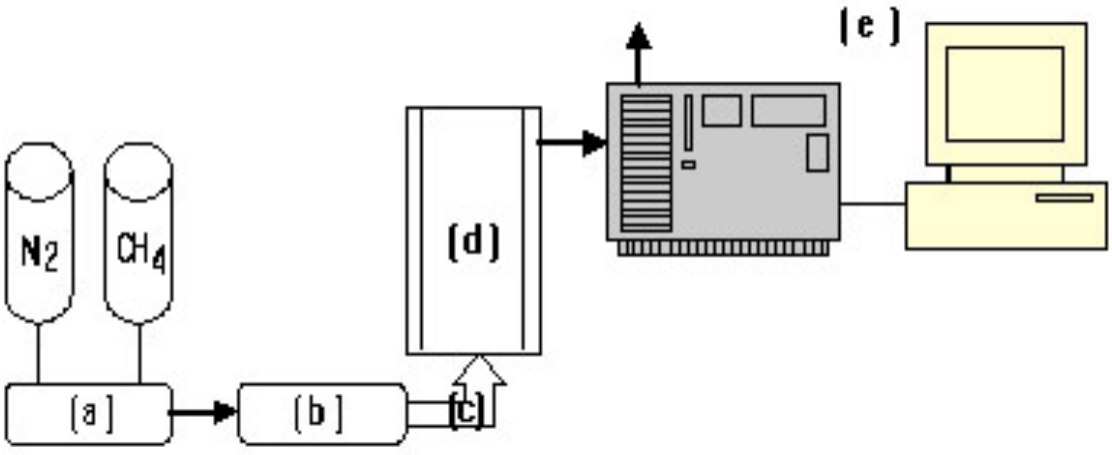

Scheme 2.1 The MSR reaction system ((a) a gas unit (containing N_2 and CH_4 cylinders and a mass controller), (b) a steam generator, (c) a gas pre-heater, (d) a tubular reactor, and (e) a gas chromatograph (GC)).

2.4.1.1 MSR Reaction - Activity Testing

A 200 mg sample was placed in the middle of a 4 mm id long reaction tube

sandwiched between two silica wool plugs. First, the sample was pretreated under a flowing stream of dilute hydrogen (5% H_2/Ar) with the total flow rate of 20 mL/min at 350 ^oC for 2h. The sample was then allowed to cool to room temperature followed by raising the temperature to 800 ^oC under a flowing stream of nitrogen at a flow rate of 8-11 mL/min for 2 h. The temperature was dropped to 300 ^oC before switching the nitrogen gas to reaction gas mixture. A constant flow of mixture gas was provided by the gas unit and steam generator with the gas hourly space velocity (GHSV) 11,600 mL/h with the composition of $H_2O/CH_4/N_2$ = 32.7/25.1/42.2 vol.-%. The mixture gas was preheated to 110 ^oC and then injected into the tubular reactor. The GC analyzer (PerkinElmer ARNEL, AutoSystetm XL) was used to measure the concentration of H_2, CO_2, N_2, CO and CH_4 in the production. Before each measurement was taken, 30 min equilibration time was allowed. This was followed by three consecutive measurements taken at 10 min intervals at a fixed temperature and the data was averaged. The temperature was ramped from 300 ^oC to 800 ^oC.

2.4.1.2 MSR Reaction – Stability Testing

Stability of the catalyst was evaluated under a flowing stream of $H_2O/CH_4/N_2$ = 6.3/25.1/68.6 vol.-% with a GHSV of 11,600 mL/h at 800 ^oC with the same pretreatment of catalyst before starting the testing. Once the stability testing started, data were collected from GC analyzer every 15 minutes until the reactor was blocked, which was indicated from the reaction flow rate decreasing.

2.4.1.3 Calculation method

The concentrations of CH_4^{in} and product gas mixture: H_2, CO and CO_2, CH_4^{out} with reference to N_2 were monitored by GC-TCD. Thus, the H_2, CO and CO_2 productivities were calculated with respect to N_2 with a constant GHSV. The percents of CH_4 conversion to CO_x (CO + CO_2) and to carbon were calculated as $[(CO+CO_2)/CO+CO_2+CH_4^{out}] \times 100\%$ and $[(CH_4^{in} - CO - CO_2 - CH_4^{out})/ CH_4^{in}] \times 100\%$, respectively.

The yield of major gas species in the product was also calculated in this way: The rate of N_2 was set as the basic rate. The percentage of CH_4 (H_2, CO, and CO_2) was referenced to the percentage of N_2 in the product. The CH_4 consumption and carbon deposition during the experiment (activity testing and stability testing) were calculated by equation (1) to (3):

Consumption of CH_4 (%) =

The yield of CH_4 injected (CH_4^{in})/ the yield of CH_4 in the product (CH_4^{out}) × 100

(2.10)

Carbon deposition (compare to whole gas mixture) (%) =

[The percentage of CH_4^{in} – the percentage of $(CO_2 + CO + CH_4)^{out}$] × 100

(2.11)

Carbon deposition (compare to initial CH_4) (%) =

Carbon deposition (compare to whole gas mixture) / the percentage of CH_4^{in}

(2.12)

2.4.2 Hydrogenolysis of Glycerol

2.4.2.1 Experimental Details

The hydrogenolysis of glycerol reaction was carried out in the liquid phase in a 300 mL stainless steel autoclave (Figure 2.7). The autoclave was equipped with a magnetic stirrer, a pressure gauge and a thermocouple (Chapter 5).

Figure 2.7 High pressure glycerol hydrogenolysis reactor

A typical experiment was carried out in the liquid phase in a stainless steel Parr autoclave. The catalyst was placed in the autoclave and suitable amount (e.g. 50 mL) of 0.68 M solution of glycerol (Aldrich, spectrophometric grade >99.5%) in DI water was added. The autoclave was then flushed with pure hydrogen (99.99% BOC) for a minute to remove any traces of oxygen. The autoclave was pressurized to a high pressure (e.g. 20 bar) with hydrogen (99.99% BOC) at 20 ^{o}C and heated to a reaction temperature of 150 ^{o}C. The autoclave was then cooled to 10 ^{o}C and the gas phase analyzed by a Perkin Elmer Autosystem XL Arnel Gas phase GC-FID. After that, the reactor was cooled down with dry ice and all the gases present were released. Then 50 μL of 1.0 M glucose solution was added as an external standard to the liquid filtrate of the sample and was analysed with a Perkin Elmer 200 series HPLC equipped with a refractive index detector.

2.4.2.2 Product Analysis

Gas phase reaction products were analysed using a Perkin Elmer Autosystem XL gas chromatograph equipped with a flame ionization detector (FID) and a Carbosphere (80/100 mesh, 1/8 inch x 6ft) packed column. The reactor was cooled by dry ice and attached to the GC through the reactor outlet valve which was slowly opened to fill the detector's sample loop. The gas filling the loop was at atmospheric pressure as the loop was connected to an outlet valve. The gaseous products were then passed through the chromatographic column to separate the different components

before being passed through a methanator reactor, which converted all the carbon containing products to methane over a catalyst. The methane fractions could then be detected using FID, whereby a hydrogen/compressed air flame ionized the organic components detected by a collector plate.

Liquid phase products were analysed in a Perkin Elmer series 200 HPLC machine. The HPLC was fitted with an Aminex HPX-87H (300 mm x 7.8mm) ion exchange column and a refractive index detector. 75µl of sample were injected into a flow of 0.025M H_2SO_4 using an autosampler needle. After slight differences in volume of sample injected by the HPLC autosampler it was decided to use an external standard. Glucose was chosen as it eluted earlier than any of the reaction products, and so all product concentrations were calculated relative to the peak area of glucose in that injection. The RI detector measured the differences between the refractive indices of the carrier solution and the products which were eluted from the column and produced a peak spectrum. Because of the different relative refractive indices of the products, calibration curves had to be made for each product to relate the refractive index peak area to its concentration. All calibrations were done relative to the area of a 0.01M glucose solution and at a range of concentrations spanning at least an order of magnitude.

A spreadsheet was created to calculate the molar quantities of the different products in the liquid reaction mixture from their concentration, worked out from the ratio of the HPLC refractive index peaks to the peak of 0.01M glucose. To calculate the molar quantities of gas phase products, the FID peaks were related to molar gas

quantity through a single calibration given by the manufacturer. The concentrations were then multiplied by the reaction pressure and the reactor headspace volume to give the true molar quantities of gas produced. The selectivity to each product was then calculated taking into account the stoichiometry of its formation:

Product Selectivity (%) =

Product Moles × 100 / Glycerol Moles in Starting Solution (M) × Stoichiometric Coeff. (2.13)

The total conversion of glycerol was calculated as

Glycerol Conversion (%) =

Glycerol conc. in product (M) × 100 / Glycerol conc. in starting solution (M) (2.14)

Glycerol concentration was determined exactly by running the starting solution through the HPLC and applying the glycerol calibration curve. To ensure accuracy the carbon mass balance was calculated according to:

Carbon Mass Balance (%)=

Total carbon moles in product × 100 / Total carbon moles in starting material (2.15)

All the reactions reported here gave a mass balance of >95%.

2.5 References

1. P. Collier, S. Golunski, C. Malde, J. Breen, R. Burch, Journal of the American Chemical Society, 125 (2003) 12414-12415.
2. T. Masui, K. Fujiwara, K. Machida, G. Adachi, T. Sakata, H. Mori, Chemistry of Materials, 9 (1997) 2197-2204.
3. C.M.Y. Yeung, K.M.K. Yu, Q.J. Fu, D. Thompsett, M.I. Petch, and S.C. Tsang, Journal of the American Chemical Society, 127 (2005) 18010-18011.
4. R.A. Van Santen, P.W.N.M. Van Leeuwen, J.A. Moulijn and B.A. Averill, Catalysis: an Integrated Approach, Elsevier, Amsterdam, 2000.
5. D.A. Skoog, F.J. Holler, T.A. Nieman, in Principles of Instrumental Analysis, Harcourt Brace College Publishers, Florida, 1998.
6. J.M. Thomas and W.J. Thomas, Principles and Practice of Heteregeneous Catalysis, VCH, Weinheim, 1997.
7. I. Chorkendorff and J. W. Niemantsverdriet, Concepts of modern catalysis and kinetics, Wiley-VCH, Weinheim, 2003.
8. N. Yao, Z.L. Wang, Handbook of microscopy for nanotechnology, Kluwer Academic publishers, New York, 2005.
9. J.W. Niemantsverdriet, Spectroscopy in catalysis: an introduction, Wiley-VCH, Weinheim, 2000.
10. L.A. Bendersky, F.W. Gayle, Journal of Research of the National Institute of Standards and Technology, 106 (2001) 997-1012.

11. http://cime.epfl.ch/page32481.html
12. G. Attard and C. Barnes, Surfaces, Oxford University Press, Oxford, 1998.
13. J.H. Scofield, Journal of Electron Spectroscopy and Related Phenomena, 8 (1976) 129-137.
14. H.E. Kissenger, Analytical Chemistry, 29 (1957) 1702-1706.
15. R.T. Weber, J.J. Jiang, D.P. Barr, EMX Manual, Bruker Instrument, 1998.
16. D. Tibiletti, F.C. Meunier, A. Goguet, D. Reid, R. Burch, M. Boaro, M. Vicario, A. Trovarelli, Journal of Catalysis, 244 (2006) 183–191.
17. F.C. Meunier, D. Reid, A. Goguet, S. Shekhtman, C. Hardacre, R. Burch, W. Deng, M. Flytzani-Stephanopoulos, Journal of Catalysis, 247 (2007) 277–287.
18. J.M. Olinger, P.R. Griffiths, Analytical Chemistry, 60 (1988) 2427-2435.
19. W.H. Weber and R. Merlin, Raman Scattering in Materials Science, Springer, Berlin, 2000.

CHAPTER 3

CERIA COATED COMERCIAL NICKEL CATALYSTS: METHANE STEAM REFORMING FOR HYDROGEN PRODUCTION USING LOW WATER TO METHANE RATIOS WITHOUT CARBON FORMATION

3.1 Introduction 93

3.2 Ceria Modified Ni Catalysts Applied to Methane Steam Reforming (MSR) Reaction 96

3.2.1 Model Design 96

3.2.2 Catalytic Performance 97

3.2.3 Resistance to Carbon Deposition 102

3.3 Catalysts Characterization 108

3.4 Discussion 120

3.5 Conclusion 123

3.6 References 124

3.1 Introduction

Methane steam reforming (MSR) is an established process for the large scale production of hydrogen in industry [1-4]. Recently, there has been renewed interest in the process as hydrogen is considered a clean carrier (for fuel cells or internal combustion engines [4]) for future energy provision [5]. Also, hydrogen purification from hydrogen rich reforming mixtures using membrane technology or pressure swing adsorption [6, 7] has received much attention. Particularly, targets are small hydrogen generators giving high levels of hydrogen using MSR have recently been demonstrated. Thus, current intense research effort is being placed on hydrogen generation by means of methane steam reforming (MSR - Equation 3.1) and water gas shift (WGS - Equation 3.2) followed by carbon capture or sequestration.

$$CH_4 + H_2O = CO + 3\ H_2 \quad (\Delta H^o_{298} = 206\ kJ/mol) \qquad (3.1)$$

$$CO + H_2O = CO_2 + H_2 \quad (\Delta H^o_{298} = -41\ kJ/mol) \qquad (3.2)$$

$$CH_4 = C + 2\ H_2 \quad (\Delta H^o_{298} = 76\ kJ/mol) \qquad (3.3)$$

$$2\ CO = C + CO_2 \quad (\Delta H^o_{298} = -173\ kJ/mol) \qquad (3.4)$$

The typical reformate produced from MSR consists of hydrogen, carbon monoxide and carbon dioxide. Depending on the actual pressure, temperature and steam-to-carbon ratio, different equilibrium conditions are achieved that determine the exact composition of the gas. A higher water/methane ratio in the feedstock favours

higher conversions, but unnecessary use of more steam than the reaction stoichiometry is energetically unfavourable and also dilutes the hydrogen content from the reformate. In addition, the H_2/CO ratios for downstream processes such as gas to liquid (GTL) technology can result in an overall poor efficiency for the operation. However, the use of stoichiometric or even lower ratios of steam to methane leads to severe carbon deposition over conventional nickel based steam reforming catalysts. This is because methane decomposition (Equation 3.3) and the Boudouard reaction (Equation 3.4) for carbon formation are favourable over nickel catalysts [8-13], but the deposited carbon can only be removed through gasification with steam or carbon dioxide, provided that steam to methane ratios higher than unity are used [11, 12, 14-16]. However, CeO_2 is commonly used as a support for many hydrocarbon reactions, and is known to offer resistance to carbon deposition because of its redox activity [5]. Recently, Huang *et al.* [10-12] demonstrated that nickel catalysts on ceria showed self de-coking capability, i.e. removal of the deposited carbon species *via* gasification by the O species supplemented from the lattice oxygen of the catalyst itself. It has been postulated that the role of CeO_x (x = 2 or 1.5) is to accelerate the reaction of steam with adsorbed carbon species on the metal surface at the metal-oxide interface, so the surface carbon species are quickly converted to gaseous products, preventing accumulation.

In this work, ceria was added to a commercial 65 wt.% Ni/SiO_2/Al_2O_3 powder catalyst (NSA) *via* a deposition precipitation method with and without polymer reversed charge pre-treatment [17] and also *via* a modified sol-gel method [18, 19].

The powder commercial catalyst together with the materials generated by the three methods, were then tested for MSR under the steam to methane ratios of above/below 1.0. Under such conditions carbon deposition is thermodynamically favourable, and thus comparison of their reaction activity, stability, and extent of carbon deposition was made. These materials were also characterised by DRIFTS, XRD, TPR, TGA, TEM and EDX with the aim of gaining insights on the important factors for inhibiting or severely reducing the extent of carbon deposition during MSR under stoichiometric or lower steam methane ratios.

3.2 Ceria Modified Ni Catalysts Applied to Methane Steam Reforming (MSR) Reaction

3.2.1 Model Design

The idea of the ceria modified Ni commercial catalyst is based on the following model: ceria is designated to surround the nickel particle as a shell in order to prevent carbon formation on the surface of nickel, as shown in Scheme 3.1. A thin ceria shell is used to cover the nickel core. The promoted ceria catalyst gives high activity for the MSR reaction without carbon deposition.

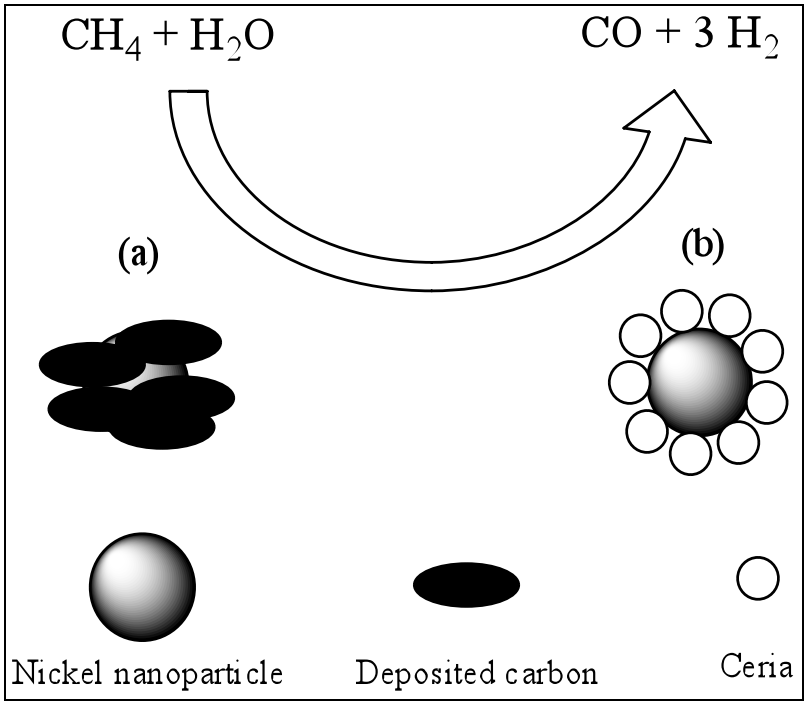

Scheme 3.1 The MSR reaction over Ni catalyst: (a) Traditional nickel catalyst poisoned by the deposited carbon during the reaction; (b) Ni nanoparticle is protected by the covered ceria as a core-shell catalyst.

3.2.1 Catalytic Performance

Figure 3.1 shows that methane conversion over the commercial supported Ni catalyst (NSA) increases with rising temperature with the selectivity shifting towards H_2 and CO production under a flowing stream of 32.7 % H_2O and 25.1% CH_4 ($H_2O/CH_4 \sim 1.3$) at the GHSV of 11,600 h^{-1}.

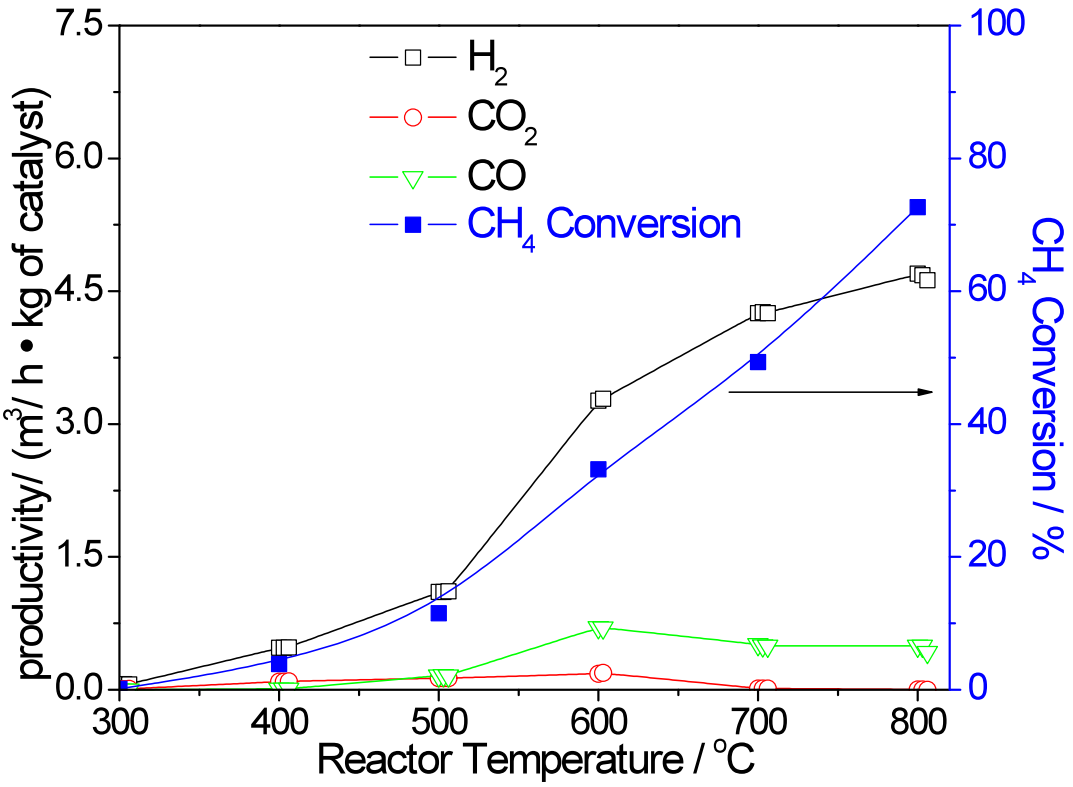

Figure 3.1 Productivity values for various products were obtained by passing 32.7 % H_2O and 25.1% CH_4 balanced with N_2 at GHSV of 11,600 h^{-1} over NSA sample at the temperature range of 300 ℃ to 800 ℃.

When the reaction temperature was 300 ^{o}C, the conversion of methane to hydrogen was very low (hardly detected). With increasing temperature the selectivity shifted towards higher H_2 production, primarily due to the reaction between methane and steam which turned methane into hydrogen and carbon monoxide. The reaction of hydrogen itself with carbon dioxide produced more carbon monoxide.

There was a sharp rise in the H_2 yield with a simultaneous increase in methane conversion with an on-set temperature around 400-500 ^{o}C. The tangent line drawn from the slope of the temperature change cutting the temperature axis is defined as the on-set temperature. High activation energy (estimated to be 49.0 kJ mol^{-1}) is required for this reaction, and it is noted that the activation energy derived could be affected by thermodynamic and kinetic limitations, for example starvations in substrate concentrations at higher temperatures. As a result, this value was derived below 550 ^{o}C, where the conversions of methane and water were kept below 35% (under near plug flow reactor conditions). This calculated energy matches well with those published using nickel catalysts [23].

Figure 3.2 shows the catalytic performances of the four CeO_2 modified NSA catalysts with different preparation conditions, and the synthesis details are listed in Chapter 2.

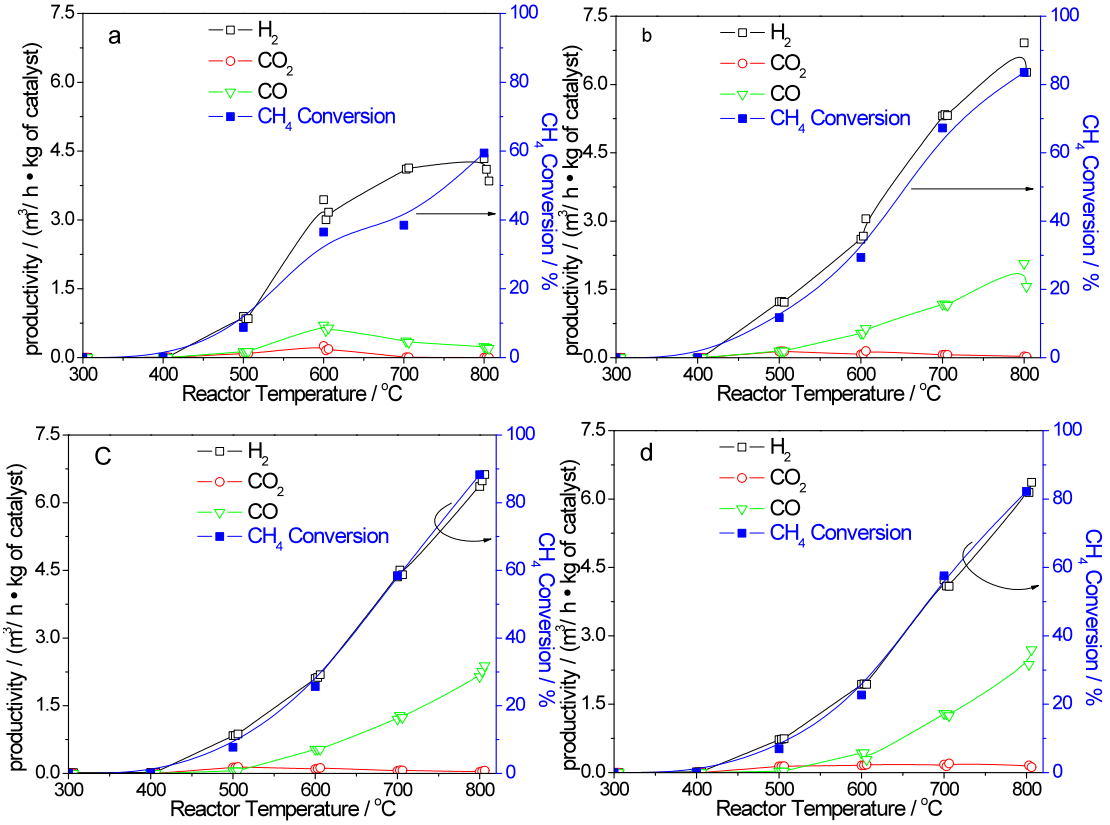

Figure 3.2 Productivity values for various products were obtained by passing 32.7% H_2O and 25.1% CH_4 balanced with N_2 at GHSV of 11,600 h^{-1} over different ceria modified NSA samples (a - NSAC-CN; b - NSAC-CNP; c - NSAC; d - NSAC-M2) at the temperature range of 300 ^oC to 800 ^oC.

In Figure 3.2a, compared to the original NSA sample, NSAC-CN during the methane steam reforming reaction does not show improvement from 300 ^{o}C to 700 ^{o}C. On the contrary, at 800 ^{o}C it appears to be worse than the original NSA (probably due to metal site alternation). On the other hand, NSAC-CNP shows a higher methane conversion with consistently higher H_2 production under a comparable temperature regime. Although there is a significant difference from Figure 3.1 compared to Figures 3.2b and Figure 3.2c/Figure 3.2d, there is no large difference between Figure 3.2b and Figure 3.2c/Figure 3.2d in the relative gas composition under this short test time.

In Figure 3.3, it is interesting to note that the H_2/COx ratio produced appears to be much higher than stoichiometric ratios (H_2/COx ratio of 3 - 4 is expected since the MSR of H_2O/CH_4 at 1:1 can produce H_2/CO =3 and some surplus H_2 formed from water gas shift reaction by forming CO_2), especially when higher temperatures were used. (H_2/COx > 9 was observed at 700-800 ^{o}C over the samples NSAC-CN and at 800 ^{o}C over NSA).

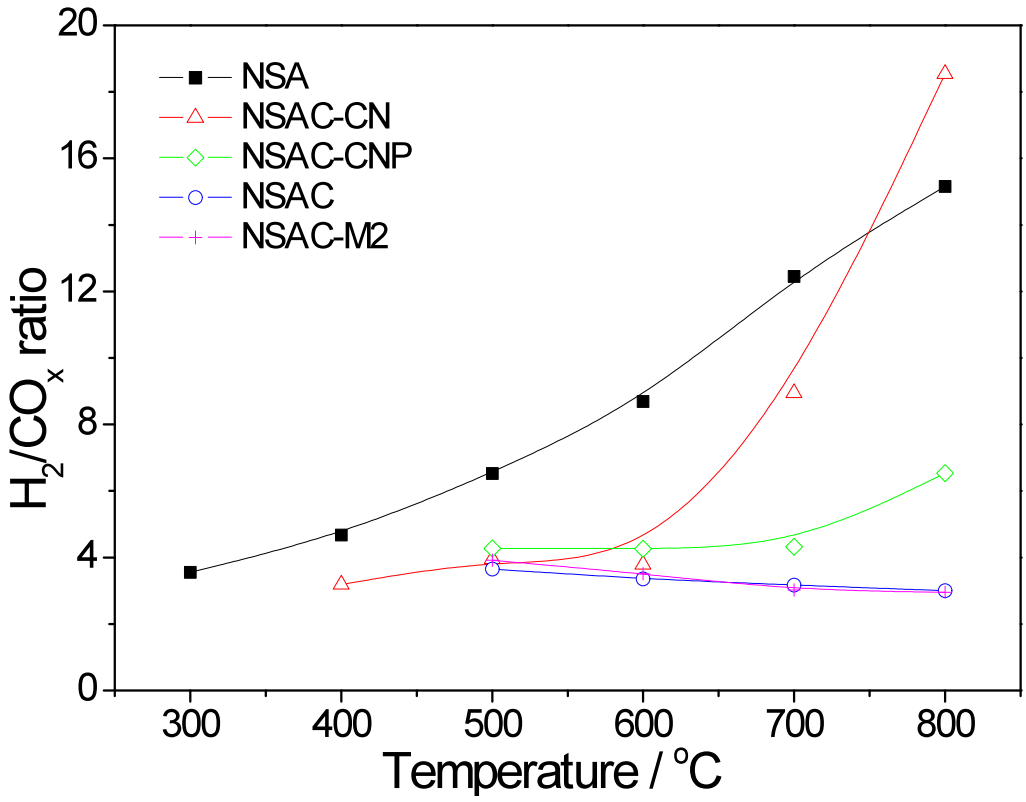

Figure 3.3 H_2/CO_x ratios for various products were obtained by passing 32.7% H_2O and 25.1% CH_4 balanced with N_2 at GHSV of 11,600 h^{-1} over different ceria modified NSA samples.

This implies that additional hydrogen was produced from methane decomposition ($CH_4 = C + 2\ H_2$). We note that the catalyst suffered from a rapid deactivation (due to carbon deposition) even during the short testing period. At 800 ^oC, the catalyst quickly levelled at about 70% methane conversion (deactivating catalyst) with a hydrogen productivity of about 4.5 $m^3\ h^{-1}\ kg^{-1}$cat.

The H_2/CO_x ratios deviated significantly from the stoichiometric ratio at lower temperatures to higher values at elevated temperatures (also referred to as carbon

balance in the next section). This clearly suggests that the methane decomposition into carbon and hydrogen became more significant at higher temperatures.

In contrast, NSAC and NSAC-M2 prepared from the modified sol-gel method showed higher methane conversions and H_2 productivities under the same temperature regime (see Figure 3.2c and Figure 3.2d).

The H_2/COx ratios obtained from the two samples at all temperatures were maintained at 3.2, which were close to the expected ratio implying no extensive carbon deposition within the testing period. Also, CO was the major carbon species with below 2% CO_2 in both product streams.

3.2.2 Resistance to Carbon Deposition

Table 3.1 shows the extent of calculated carbon deposition based on the difference in carbon count between reactant and product gases over the five different samples (NSA, NSAC-CN, NSAC-CNP, NSAC and NSAC-M2) during the steam reforming reaction from 300 ^{o}C to 800 ^{o}C as previously described.

Table 3.1 Carbon deposition under MSR conditions from 300 ^{o}C to 800 ^{o}C and methane decomposition at 800 ^{o}C over different catalysts

Catalyst	Carbon deposition[a]						Methane decomposition to carbon[b] (%)
	300 ^{o}C	400 ^{o}C	500 ^{o}C	600 ^{o}C	700 ^{o}C	800 ^{o}C	
NSA	0	0	4.3	11.6	60.4	75.4	25.3
NSAC-CN	0	0	0	6.0	62.1	84.6	20.0
NSAC-CNP	0	0	0	5.5	24.6	35.8	19.4
NSAC	0	0	0	1.1	1.0	0.5	13.6
NSAC-M2	0	0	0	1.9	1.9	-2.8	5.4

Carbon deposition[a] was calculated based on the difference in the total carbon count of reactant and product gas before and after the MSR reaction: $[(CH_4^{in} - (CO+CO_2+CH_4)^{out})/ CH_4^{in}] \times 100\%$. The result was averaged by the first three data collected for each reaction temperature. The error was estimated to be ± 0.1% using the pure silica as the catalyst. The negative value for NASC-M2 was assigned to the possible disturbance of gas flow or/and volume change(s) during the MSR over the sample.

Methane decomposition to carbon[b] was evaluated by TGA method: 10 mg samples was pre-treated in a flowing stream of 2% methane/N_2 with the flow rate of 60 mL/min before the temperature was ramped at 30 ^{o}C / min from room temperature to 800 ^{o}C and kept there for 900 min. The %weight gain relative to the sample weight at 800 ^{o}C after 900 min was measured by the gravimetric method.

At low temperatures (< 600 ^{o}C), there was very little carbon deposition over all the samples. Above 700 ^{o}C severe carbon deposition was encountered over NSA and NSAC whilst NSAC-CNP exhibited an intermediate degree of carbon deposition amongst all the samples. However, it is interesting to find that there was an extremely small amount of carbon loss, if any carbon deposition, over samples NSAC and NSAC-M2 during the short testing period. Within experimental error the measured carbon balances of the two samples were within 3%, which indicated no significant carbon deposition. Also, an independent evaluation for carbon deposition from methane decomposition over the samples under a flowing stream of 2% methane/nitrogen using gravimetric thermal analysis (TGA) at 800 ^{o}C was carried out.

The weight increase relative to the sample at 800 ^{o}C ranked the extent of carbon deposition from methane as the following order: NSA > NSAC-CN > NSAC-CNP > NSAC >> NSAC-M2. This order is the similar to those calculated carbon deposition under the MSR conditions (NSA apparently showed a lower carbon loss than the NSAC-CN however, we noted that the deactivation over the NSA was so rapid that the actual values of carbon loss were expected to be much higher than those measured values at above 600 ^{o}C).

It should be noted that the small extent of carbon gain in the case of NSAC-M2 from the TGA is comparable to the result using pure silica as a sample indicating that its catalytic surface is as inert as the container material for carbon deposition by thermal methane decomposition. The results clearly suggest that the extent of carbon deposition over Ni catalysts under MSR conditions can be eliminated, or at least

substantially reduced, whilst maintaining the high activity for MSR reaction, by blending the commercial Ni catalyst with ceria. Also, an important point to note is that this kinetic inhibition of carbon deposition critically depends on the preparation method by which the ceria is blended.

A stability test for NSA and ceria modified Ni commercial samples under the MSR conditions was evaluated at 800 ^{o}C under a flowing stream of 6.3% H_2O and 25.1 % CH_4 in N_2 at the GHSV of 11,600 h^{-1}. It is noted that the water to methane was deliberately set at 0.25 and the results of all the samples are summarised in Table 3.2.

Table 3.2 The comparable parameters of different samples during the stability testing

Catalysts	Active life	Yield of H_2			Carbon deposition		
		1hr	10hrs	100hrs	1hrs	10hrs	100hrs
NSA	<16.1 hrs	1	0.17	/	1	1.28	/
NSAC-CN	1.9 hrs	0.95	/	/	1	/	/
NSAC-CNP	3.1 hrs	0.96	/	/	0.94	/	/
NSAC	19.3 hrs	0.78	0.18	/	0.68	0.18	/
NSAC-M2	>112.3 hrs	0.84	0.32	0.40	0.69	0.008	0

*The yield of H_2 and the carbon deposition over NSA at 1hr are both set to 1, and the parameters of other samples are calculated based on these two factors.

From Table 3.2 it is clear to see that under the very low water to methane ratio reaction condition NSA loses the activity (the reactor is totally blocked by formed carbon) in less than 16 hours. NSAC-CN and NSAC-CNP deactivate much more quickly (1.9 hours for NSAC-CN and 3.1 hours for NSAC-CNP). On the other hand, NSAC remains active longer than NSA, but not for more than 20 hours. Compared with other three ceria modified nickel samples, NSAC-M2 shows a high stable activity even after 112 hours' reaction.

Figure 3.4 shows some significant parameters from NSAC-M2 during the MSR stability testing reaction.

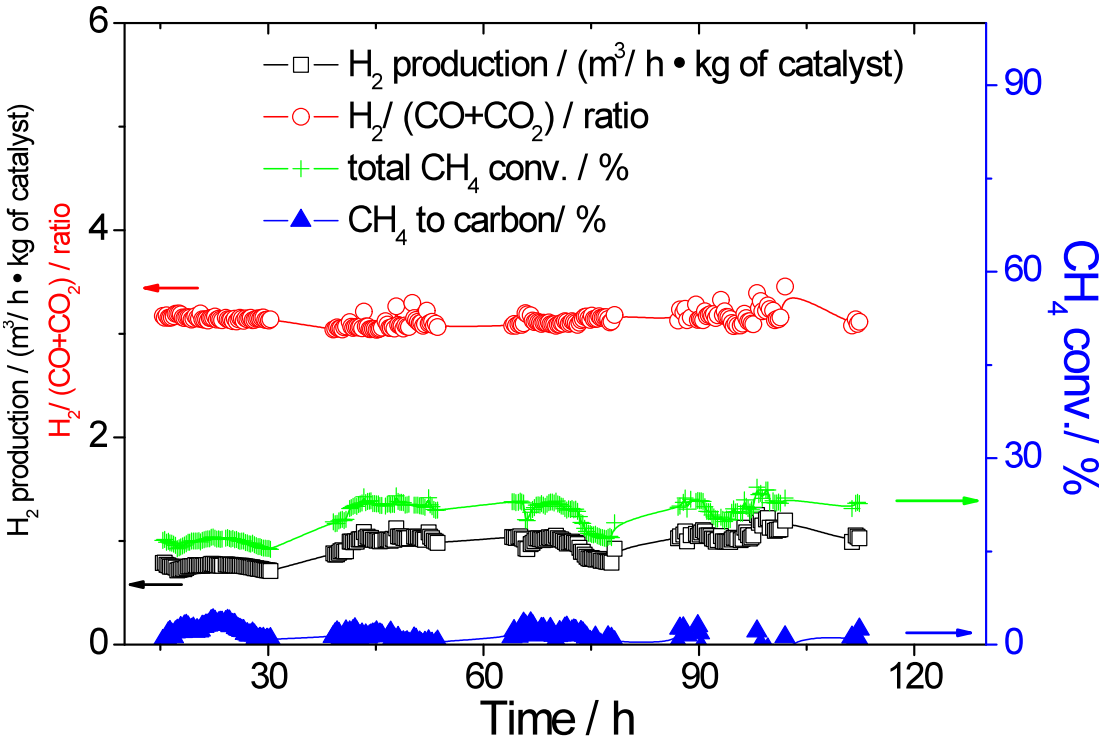

Figure 3.4 A stability test over NSAC-M2 using 6.3 % H_2O and 25.1% CH_4 in N_2 at GHSV of 11,600 h^{-1} at 800 ^oC.

Under such highly reducing conditions conventional catalysts would be very susceptible to carbon deposition, leading to rapid deactivation. As seen from Figure 3.4, we find that the catalyst gave about 25% methane conversion presumably achieving the total consumption of water to CO and H_2 (unsteady conversions along the testing period were primarily due to a slight fluctuation in the steam generation). The activity was maintained for more than five days (about 112 h) with a constant high rate of hydrogen production giving the H_2/COx value at about 3.1. On the other hand, the parent catalyst, NSA, almost immediately lost all its activity for hydrogen production within a short time (< 16.1 h) with the reactor entirely blocked up by the carbon deposited over this sample under the same conditions (hence the stability study could not be continued beyond this time).

3.3 Catalysts Characterization

Figure 3.5 shows the XRD results of NSA (commercial catalyst), NSAC-CN (ceria doped nickel catalyst by deposition precipitation method), NSAC-CNP (ceria doped nickel catalyst by polymer-added deposition precipitation method), NSAC (sol-gel method) and NSA-M2 (sol-gel method).

The commercial catalyst NSA showed diffraction peaks, which match well with Ni (2θ of 44.5, 51.9 and 76.4 degree) and NiO (2θ of 36.7 and 62.8 degree) phases. This suggests the co-existence of metallic Ni and NiO phases in the NSA sample before the hydrogen pre-treatment and activity testing.

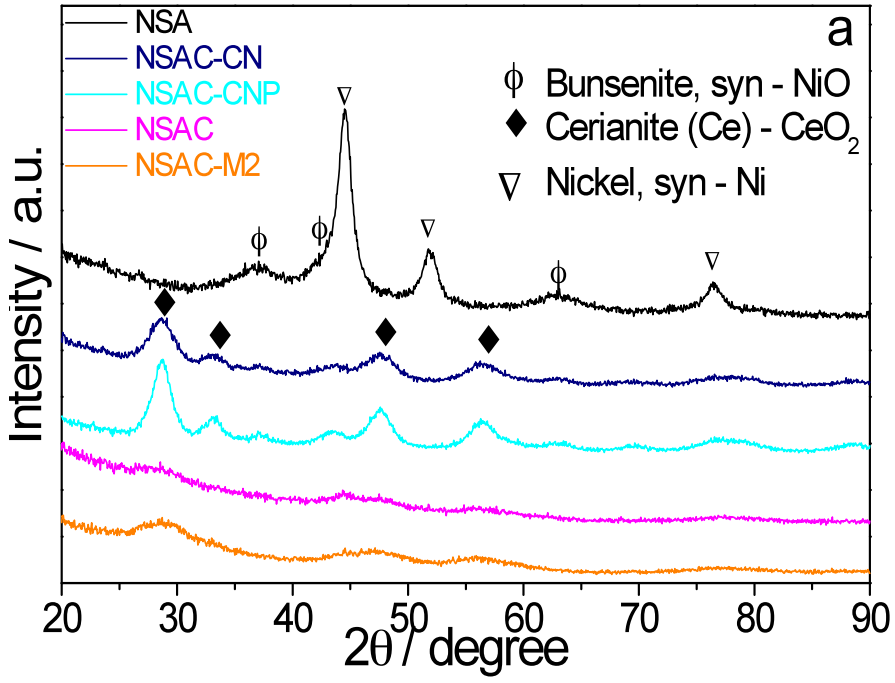

Figure 3.5 XRD patterns of NSA and CeO_2 modified NSA samples.

After the coating of CeO_2 by the deposition precipitation method, the peak intensities of Ni and NiO from the samples NSAC-CN and NSAC-CNP were much attenuated, presumably due to the dilution of Ni and NiO phases by the additive. It should be noted that the dense NSA (0.5 g) was greatly diluted by the ceria precursor (1.2 g), thus the representative sample for XRD contained a relatively smaller quantity of NSA. However, the metallic Ni peaks were still visible in those samples with the ceria inclusion despite the size attenuation (seen also from TEM). Also, some new characteristic diffraction peaks of CeO_2 (2θ degree of 28.6, 33.1, 47.5 and 56.3) indeed appeared in both samples. Similarly, having modified NSA with ceria isopropoxide by the sol-gel method, the diffraction peaks of NiO and Ni almost disappeared in NSAC and NSAC-M2. Furthermore, there was no significant peak intensity of CeO_2 detected. One reason could be that the particle size of ceria was too small to be distinguished from the background.

Figure 3.6 shows the XRD results of all these samples after the MSR activity testing reactions (Chapter 3.3.1).

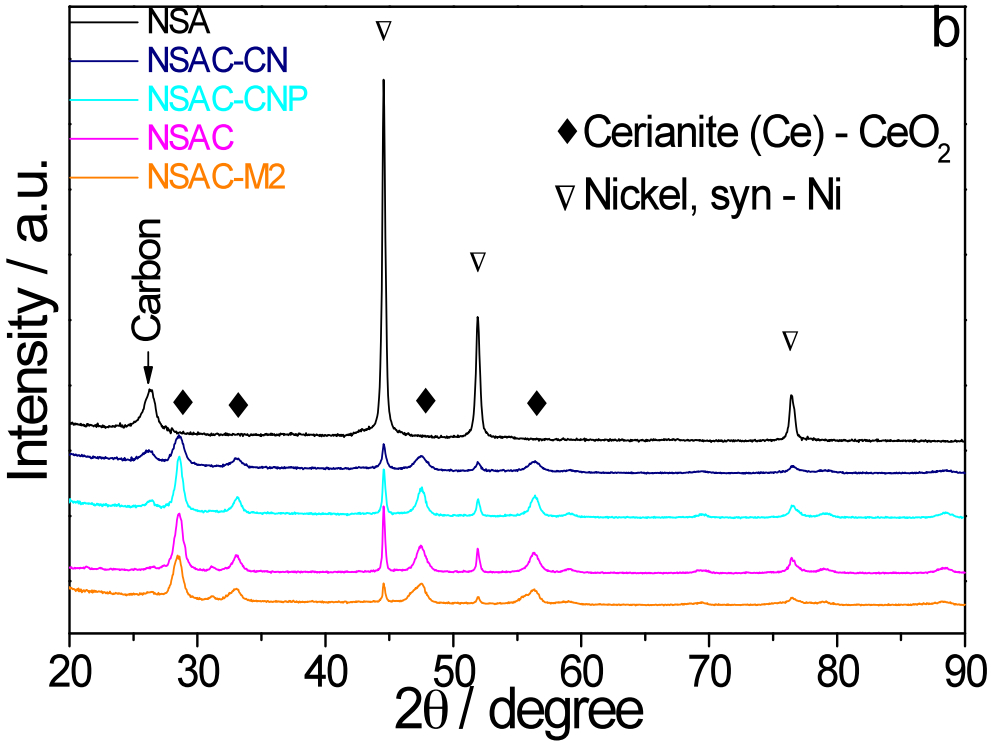

Figure 3.6 XRD patterns of NSA and CeO_2 modified NSA samples after MSR reaction.

After the MSR activity testing, all the samples showed sharp peaks of Ni and CeO_2, indicative of a degree of sintering under the reaction conditions, and no NiO peak can be found. A new peak at 26.2 (2θ) is assigned to graphitic material with an interlayer of the NSA, NSAC-CN and NSAC-CNP samples. This fact supports the observation of carbon deposition at least partially in form of graphite over the samples. However, no graphite formation is evident in the NSAC and NSAC-M2 samples. This evidence reinforces the observation that the carbon (discussed later) was formed over the NSA, NSAC-CN and NSAC-CNP samples prepared by the deposition precipitation method but not on the sol-gel prepared samples, NSAC and NSAC-M2 during the activity testing reactions.

Figure 3.7 shows the TEM image of the NSA sample's profile, the black points are the Ni nanoparticles from this commercial sample. The average particle size of Ni is about 10 nm.

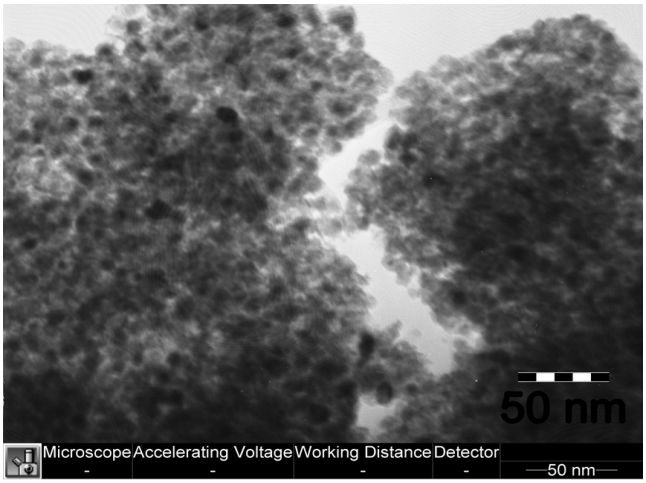

Figure 3.7 TEM image of NSA – 65%Ni/SiO_2/Al_2O_3;

Figure 3.8 shows the images of NSAC-CN (prepared by the deposition precipitation method) and NSAC-M2 (sol-gel method).

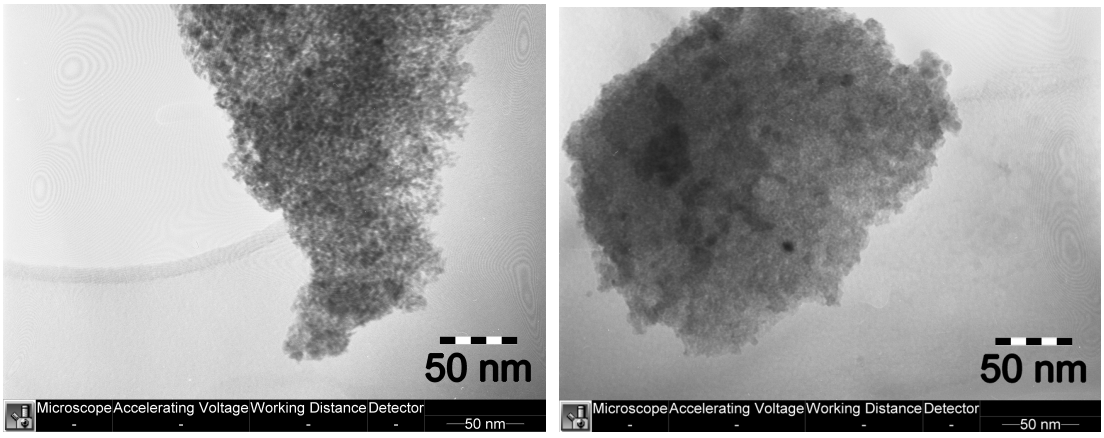

Figure 3.8 TEM image of (a) left: NSAC-CN - NSA modified with CeO_2 by deposition precipitation method; (b) right: NSAC-M2 - NSA modified with CeO_2 by sol-gel method.

In Figure 3.8a, after adding ceria to NSA sample by the deposition precipitation method, it is found that Ni nanoparticles are shattered into smaller particles (match the results from XRD in Figure 3.6). In Figure 3.8b, the Ni nanoparticle remains the same particle size around 10 nm as the original NSA, indicating that there was no major alteration in particle size despite various deposition methods, but the concentration was much lower than the NSA sample. It can be concluded from this that the additive ceria was injected at the interface between the Ni nanoparticle and the silica and alumina support, which means ceria and Ni is in close proximity to each other.

Attempts were made at obtaining elemental analysis at the near surface region of these catalyst materials. According to Monte Carlo simulations using SANYL [24] 6 keV electrons have a penetrating depth of about 0.5 μm, hence the electron beam energy for EDX analysis was attenuated to about 6 keV.

Table 3.3 shows the analysis results from EDX for each fresh catalyst before the MSR activity testing.

Table 3.3 Near surface elemental analysis by EDX at 6 keV

Catalyst	Atomic (%)					Ce/Ni (Calculated from EDX)	Ce/Ni (recipe ratio)
	O	Al	Si	Ni	Ce		
NSA	50.6	5.6	4.5	39.3	/	/	/
NSAC-CN	55.3	3.2	2.7	14.2	9.4	0.66	0.5
NSAC-CNP	55.3	2.4	2.3	12.3	9.8	0.80	0.5
NSAC	46.8	1.3	1.2	5.9	3.8	0.64	0.5
NSAC-M2	48.2	0.8	1.0	3.8	8.6	2.26	2.0

It was found that the percentage of Ni on the surface of the parent sample NSA is 39.3%, while the modified NSAC-CN, NSAC-CNP, NSAC and NSAC-M2 show 14.2% and 12.3% 5.9% and 3.8%, respectively with increasing cerium contents indicative of external ceria coatings.

It is envisaged that the thin ceria coating prepared by the sol-gel method particularly in the NSAC-M2 sample, must have covered the Ni catalyst very evenly with no sharp diffraction ceria peaks detected (refer to Figure 3.6) despite the fact that a high content of ceria was used. It is noteworthy that there seems to be a slight systematic variation in the Al/Si atomic ratio as the table is descended. This could modify the acid characteristics of the silica-alumina component of the catalysts possibly also affecting the catalyst propensity for carbon deposition.

Figure 3.9 shows the H_2-TPR profiles of CeO_2, parent NSA and CeO_2 modified samples.

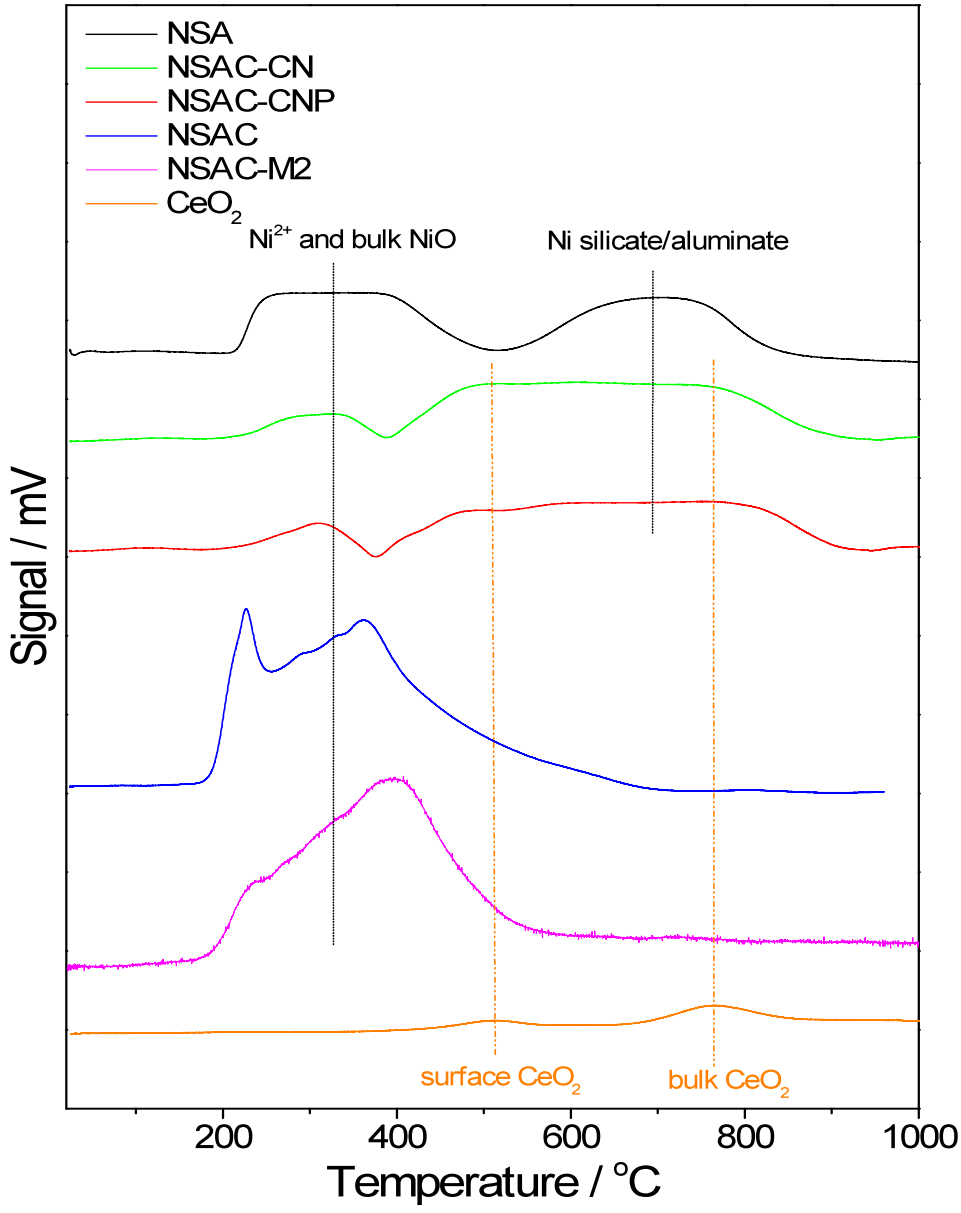

Figure 3.9 H_2-TPR profiles of CeO_2 modified NSA catalysts.

For the pure CeO_2, primarily two peaks were detected at approximately 500 ^oC and 780 ^oC [25]. These peaks are assigned to the reductions of surface and lattice oxygen from ceria. For NSA two broad reduction peaks can be clearly seen: the first reduction peak of NSA starts at 230 ^oC and ends at about 480 ^oC, the second peak starts at 500 ^oC and ends at 820 ^oC. The low temperature peak can be attributed to the reduction of lattice [O] from NiO phase while the high temperature peak to the reduction of lattice [O] from NiO with a strong support interaction, possibly relating to the formation of aluminate or silicate [25-29].

On the other hand, the TPR profile of NSAC-CN in Figure 3.9 basically represents the combination of TPR profiles of NSA and CeO_2 giving huge reduction humps. This suggests that there was no strong interaction between the parent NSA catalyst with the 'ceria coating' with their solid phases physically separated from each other.

NSAC-CN may represent the generally poor interface between Ni and ceria created using deposition precipitation or related impregnation methods. NSAC-CNP shows almost identical features as the NSAC-CN, which suggests the polymer did not give a major modification by the deposition precipitation method.

Interestingly, for NSAC prepared by the sol-gel method, no trace of the characteristic high temperature reduction peak of the bulk ceria was observed. A similar graphic character was observed for the NSAC-M2 sample, and the consumption of hydrogen was the same as the NSAC sample.

The reduction of oxygen species from the sample also appeared to take place readily with all the peaks shifted towards lower temperatures. The strong metal-support interaction between the NSA catalyst and the ceria undoubtedly facilitates reducibility of the sample. This is thought to arise from the effective ceria coating onto Ni containing phases by the sol-gel method.

Diffuse Reflectance Infrared Fourier-transform Spectroscopy (DRIFTS) for characterising exposed Ni surface with pre-adsorbed CO molecules of these samples was carried out to confirm this postulation. In Figure 3.10, it shows the adsorption bands of CO at room temperature over the pre-reduced NSA where two main bands at high frequencies, *ca* at 2087 cm^{-1} and 2057 cm^{-1} attributed to linear carbonyl species are observed [20-22]. Another distinctive band at *ca* 1925 cm^{-1} matching with bridging CO species is clearly evident (although we cannot yet assign it to two or three fold bridging with confidence). There are also some very minor peaks at around > 2087 cm^{-1} and <1925 cm^{-1}, possibly due to the linear and bridging CO species attached on metal sites with different coordination numbers.

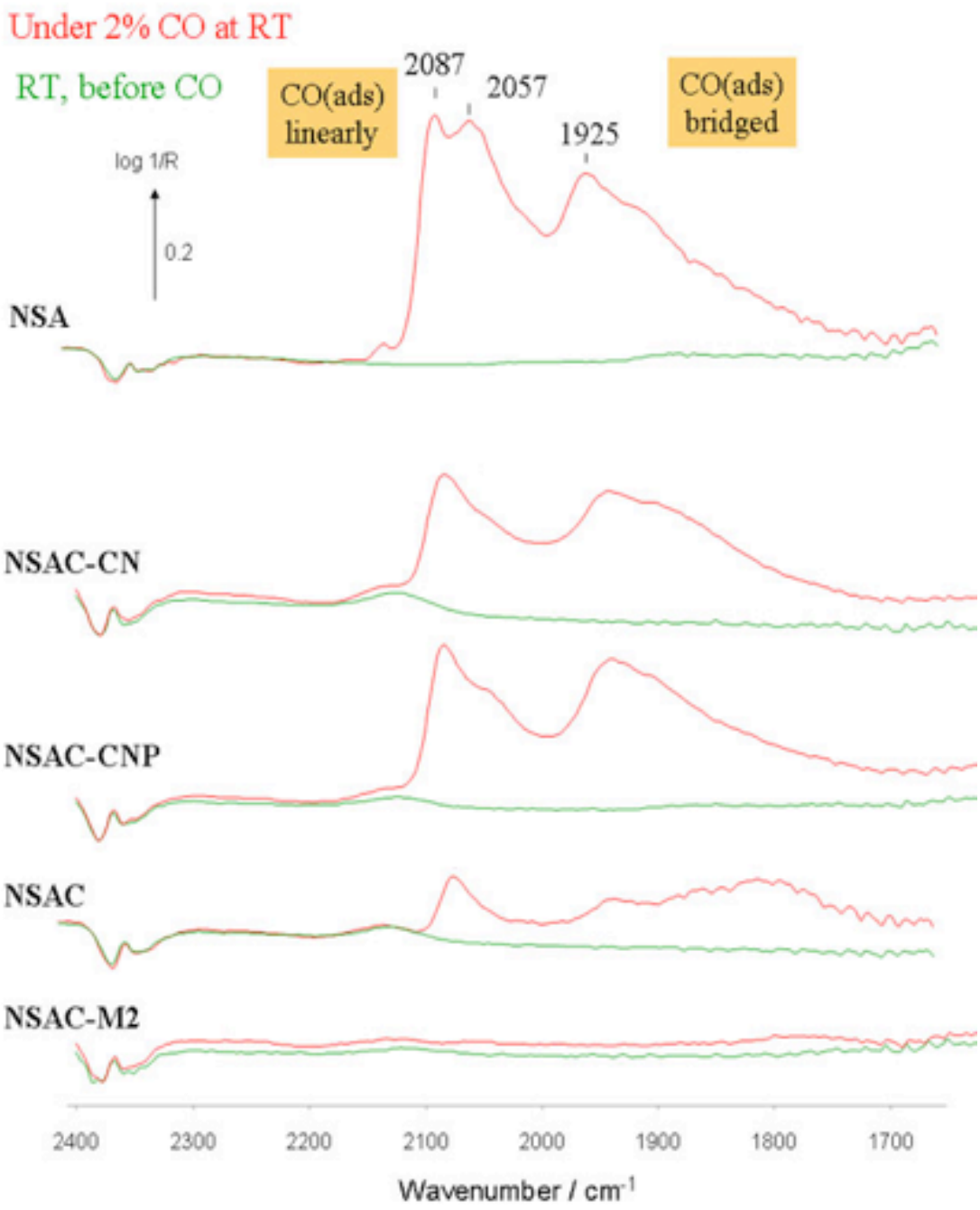

Figure 3.10 DRIFTS of CO adsorption on various Ni catalysts after their pre-reduction.

It is believed that the linear CO adsorbed species is favourably formed over the isolated metal sites (corner, edge, etc) [30] and the bridging CO species requires flat and extensive metal sites [31]. By carefully integrating the areas under these peaks, the ratios of the linear and bridging CO species are listed in Table 3.4.

Table 3.4 Relative areas of different CO adsorption peaks identified from DRIFTS data (Figure 3.10)

	Relative areas of different CO adsorption peaks			**$Area_{linearly}$ / $Area_{bridging}$ (Calculated)**
	CO (ads) linearly	**CO (ads) bridging**	**linearly + bridging**	
NSA	1.0	0.913	1.913	1.09
NSAC-CN	0.308	0.583	0.891	0.53
NSAC-CNP	0.409	0.614	1.023	0.67
NSAC	0.073	0.027	0.100	2.70

* The area of linear carbonyl species of NSA is referenced as 1.0. Others areas are calculated with respect to this peak.

It is found that the total chemisorbed CO species over the NSA sample can be referenced as 1.913 with nearly 1:1 linear to bridging distribution. Clearly, the application of ceria coatings on NSAC-CN, NSAC-CNP, NSAC and NSAC-M2 dramatically attenuated the values of chemisorption to 0.891, 1.023 and 0.100 (Table 3.4), respectively. This reflects the sol-gel coating is indeed more effective in

covering the Ni phase on the catalysts, which can create an intimate contact between Ni and ceria necessary for reducing the extent of carbon deposition during the MSR reaction.

It is also very interesting to note the alteration of linear and bridging CO species distribution depending on the preparative method. For the deposition precipitation samples, NSAC-CN and NSAC-CNP bridging mode is relatively more favourable after the application of the ceria coating. Presumably the ceria phase may have blocked the more reactive corner, edge, or defective metal sites. On the other hand, the sol-gel modified NSAC sample (NSAC-M2 cannot be analysed) shows the preferential blocking on flat or extensive metal sites (where the bridging species locate), enhancing the linearly /bridging mode ratio to 2.70. Such sol-gel deposition is likely to take place on an atomic level whereby an individual surface metal site directly interacts with ceria alkoxide molecule prior to gelation. This will break up the large Ni surface ensembles into smaller islands hence increasing the linearly /bridging mode ratio.

It should be noted that large metal ensemble (flat and extended metal sites) is thought to be responsible for carbon deposition, which requires cooperative neighbour metal sites for activation and polymerization [32, 33]. Nevertheless, we show that the supported Ni particles are modified by ceria that can substantially prolong the MSR activity without much carbon deposition.

3.4 Discussion

NSA was the commercial supported Ni catalyst with 65 wt.-% Ni on support of 1:1 silica to alumina. The NSAC-CN and NSAC-CNP samples were ceria modified NSA samples prepared by the deposition precipitation method using cerium (IV) nitrate as the precursor. The NSAC and NSAC-M2 were modified from NSA by ceria using sol-gel method with the precursor of Ce (IV) isopropoxide. From this study it is clear that the NSAC-M2 sample modified by sol-gel method shows much better resistance to carbon deposition in MSR stability testing at a very low water to methane ratio.

It is not yet clear how the structural or electronic modifications can affect the catalytic properties of the Ni particle and whether they are partially/totally covered with ceria. Table 3.5 lists the crystallite size of ceria of NSA and other ceria modified Ni catalysts after MSR reaction.

Table 3.5 Crystallite size of Ceria calculated using Scherrer equation of NSA and CeO_2 modified NSA samples after MSR reaction from XRD data (Figure 3.5)

Samples	**NSA**	**NSAC-CN**	**NSAC-CNP**	**NSAC**	**NSAC-M2**
Size (nm)	/	10.0	13.1	11.5	8.7

NSAC-M2 shows a significant smaller size (< 10 nm) of ceria compared with other ceria modified NSA samples. A mechanism is proposed to explain how nano scale ceria can deliver high activity for the removal of the deposited carbon from the surface of the Ni catalyst in the MSR reaction, and the schematic profile is shown below.

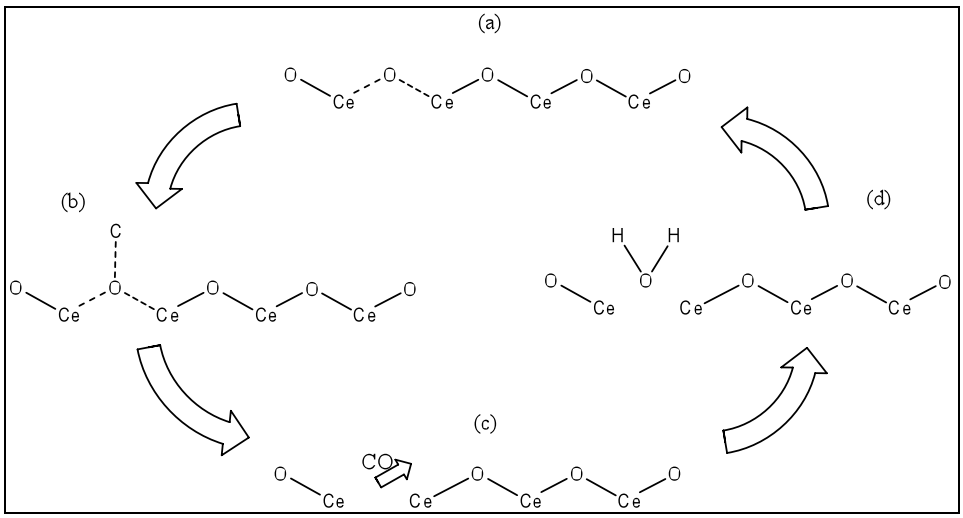

Scheme 3.2 The regeneration of mobile oxygen on the surface of ceria for oxidation from water activation over by the oxygen vacancy.

As shown in Scheme 3.2, if the deposited carbon is formed during the MSR reaction, it will be removed *via* gasification by the O species (Scheme 3.2a) on the ceria surface (Scheme 3.2b), and an oxygen vacancy is left (Scheme 3.2c) and then supplemented by trapping the oxygen atom from the water molecule (Scheme 3.2d). As a result, the ceria at the metal-oxide interface can therefore accelerate the gasification of deposited carbon. This oxygen is regenerated from the water activation over oxygen vacancy on the surface, and a catalytic cycle is thereby achieved. It

seems that nano ceria with a smaller size (specifically < 10 nm) shows a better carbon resistance. More work in Chapter 4 will give information about the effect of the size of ceria on carbon inhibition on catalyst surface.

3.5 Conclusion

By depositing ceria on a commercially supported Ni catalyst, it is demonstrated that carbon formation under MSR conditions using low water to methane ratios can be much attenuated. It is interesting to note that the degree of carbon inhibition over the Ni catalyst depends critically on the type of deposition method used. The sol-gel method using cerium alkoxide appears to be the most effective method in modifying the catalyst to eliminate or severely reduce carbon formation during the MSR conditions. Extensive catalyst characterisation indicates that an intimate contact between Ni and ceria phases must be achieved in order to enhance the beneficial metal-metal oxide interaction. Thus, the optimised, sol-gel modified Ni catalyst can give a stable and high level of hydrogen production with no significant carbon deposition at laboratory scale for over 110 h at water-methane ratio of as low as 0.25 while unmodified parent catalyst suffers from rapid deactivation under the same conditions. A longer reaction time at larger scale for testing this new catalyst using the stoichiometric water to methane ratio of MSR may be required.

3.6 References

1. M. P. Ramage, The Hydrogen Economy: Opportunities, Costs, Barriers, and R&D Needs, The National Academy Press, Washington, DC, 2004.
2. B. Yildiz, M. S. Kazimi, International Journal of Hydrogen Energy, 31 (2006) 77-92.
3. J. A. Ritter, A. D. Ebner, Separation Science and Technology, 42 (2007) 1123-1193.
4. H. G. Düsterwald, J. Günnewig, P. Radtke, Fuel Cells, 7 (2007) 183-189.
5. B. Höhlein, S. v. Andrian, T. Grube, R. Menzer, Journal of Power Sources, 86 (2000) 243-249.
6. A. Yokozeki, M. B. Shiflett, Applied Energy, 84 (2007) 351-361.
7. A. Qi, B. Peppley, K. Karan, Fuel Processing Technology, 88 (2007) 3-22.
8. M. A. Ermakova, D. Y. Ermakov, G. G. Kuvshinov, L. M. Plyasova, Journal of Catalysis, 187 (1999) 77-84.
9. S. Wang, G. Q. M. Lu, Applied Catalysis B: Environmental, 19 (1999) 267-277.
10. J. B. Wang, Y. S. Wu, T. J. Huang, Applied Catalysis A: General, 272 (2004) 289-298.
11. T. J. Huang, H. J. Lin, T. C. Yu, Catalysis Letters, 105 (2005) 239-247.
12. T. J. Huang, T. C. Yu, Catalysis Letters, 102 (2005) 175-181.
13. N. Iwasa, M. Takizawa, M. Arai, Applied Catalysis A: General, 314 (2006) 32-39.

14. C. L. Gardner, M. Ternan, Journal of Power Sources, 171 (2007) 835-841.

15. H. He, J. M. Hill, Applied Catalysis A: General, 317 (2007) 284-292.

16. L. Zhu, J. Yu, X. Wang, Journal of Hazardous Materials, 140 (2007) 205–210.

17. P. Collier, S. Golunski, C. Malde, J. Breen, R. Burch, Journal of the American Chemical Society, 125 (2003) 12414-12415.

18. K. M. S. Khalil, L. A. Elkabee, B. Murphy, Microporous and Mesoporous Materials, 78 (2005) 83-89.

19. K. M. S. Khalil, L. A. Elkabee, B. Murphy, Journal of Colloid and Interface Science, 287 (2005) 534-541.

20. A. Goguet, F. C. Meunier, D. Tibiletti, J. P. Breen, R. Burch, Journal of Physical Chemistry B, 108 (2004) 20240 -20246.

21. D. Tibiletti, F. C. Meunier, A. Goguet, D. Reid, R. Burch, M. Boaro, M. Vicario, A. Trovarelli, Journal of Catalysis, 244 (2006) 183-191.

22. F. C. Meunier, D. Reid, A. Goguet, S. Shekhtman, C. Hardacre, R. Burch, W. Deng, M. Flytzani-Stephanopoulos, Journal of Catalysis, 247 (2007) 277-287.

23. K. Watanabe, W. M. Shu, E. Motohashi, M. Matsuyama, Fusion Engineering and Design, 39-40 (1998) 1055-1060.

24. G. J. Thomas, K. J. Gross, N. Y. C. Yang, C. Jensen, Journal of Alloys and Compounds, 330-332 (2002) 702-707.

25. S. Xu, X. Wang, Fuel, 84 (2005) 563-567.

26. J. Zielin´ski, Journal of Catalysis, 76 (1982) 157-163.

27. A. G. Boudjahem, S. Monteverdi, M. Mercy, M. M. Bettahar, Applied Catalysis A: General, 250 (2003) 49-64.

28. T. Tsoncheva, M. Linden, J. Rosenholm, C. Minchev, Reaction Kinetics and Catalysis Letters, 86 (2005) 275-280.

29. S. R. Kirumakki, B. G. Shpeizer, G. V. Sagar, K. V. R. Chary, A. Clearfield, Journal of Catalysis, 242 (2006) 319-331.

30. T. Lear, R. Marshall, J. A. Lopez-Sanchez, S. D. Jackson, T. M. Klapötke, M. Bäumer, G. Rupprechter, H. J. Freund, D. Lennon, The Journal of Chemical Physics, 123 (2005) 174706

31. S. C. Chang, J. D. Roth, Y. Ho, M. J. Weaver, Journal of Electron Spectroscopy and Related Phenomena, 54-55 (1990) 1185-1203.

32. M. Primet, J. A. Dalmon, G. A. Martin, Journal of Catalysis, 46 (1977) 25-36.

33. G. A. Martin, M. Primet, J. A. Dalmon, Journal of Catalysis, 53 (1978) 321-330.

CHAPTER 4

SIZE DEPENDENT OXYGEN STORAGE CAPACITY OF CERIA NANOCRYSTALS

4.1 Introduction 129

4.2 The Synthesis of Ultrafine Ceria Nanoparticles 130

4.2.1 Microemulsion Synthesis of Ceria Nanoparticles 130

4.2.2 Size Distribution of Ceria Nanoparticles 131

4.3 Size Effect for the Structure of Ceria Nanoparticles 137

4.3.1 Lattice Expansion in Ceria Nanoparticles 137

4.3.2 Oxygen Vacancy on Nano Ceria Surface 142

4.4 Surface Oxygen Species of Nano Ceria 147

4.4.1 Surface Oxygen Species Detected from XPS 147

4.4.2 H_2-TPR Investigation of Oxygen Species 151

4.4.3 Quantification of Superoxides by EPR Technique 156

4.5 Conclusion 160

4.6 References 162

4.1 Introduction

Cerium dioxide (CeO_2) is an extensively studied and used oxide, as it supports a number of practical uses ranging from catalysis, electro- and photochemistry and material science [1]. Currently, solid oxide fuel cells (SOFC), solar cells (SC) and three-way catalysts (TWC) are among the most relevant examples where CeO_2 is the essential component [1-4]. In all these cases, the use of nano structured CeO_2-based materials can generally improve performance with respect to microsized or bulk-like materials [1-5]. Clearly, these properties are size dependent but this critical 'size effect' is, at present, not well understood. Perhaps, one important aspect is their ability to store oxygen under oxidizing conditions and to release it under reducing conditions. However, the associated structural, chemical and electronic changes in ceria at low dimension are still far from clear.

This chapter details a systematic study of these changes of ceria as a function of the decreasing particle size. Particularly, hydrogen has been employed as a reaction probe to differentiate and quantify the different types of oxygen species from nano ceria with different sizes in a careful and controlled manner through temperature programmed reduction (TPR) as well as the quantitative evaluation of superoxide species using EPR, in combination with XPS, XRD and TEM characterizations.

4.2 The Synthesis of Ultrafine Ceria Nanoparticles

4.2.1 Microemulsion Synthesis of Ceria Nanoparticles

The synthesis of ceria nanoparticles (namely MCE samples) were based on the modified microemulsion method reported by Masui et al [6], and the details are described in Chapter 2. The yield for the microemulsion process was between 55%-73%, similar to the value reported in the reference [6, 7]. It was confirmed from TG-DTA analysis data that the surfactant did not remain in the samples and the BET N_2 surface areas of these samples are around 100-120 m^2/g, similar to those reported [6, 7]. Figure 4.1 shows a typical XRD pattern, in this case, of MCE02.

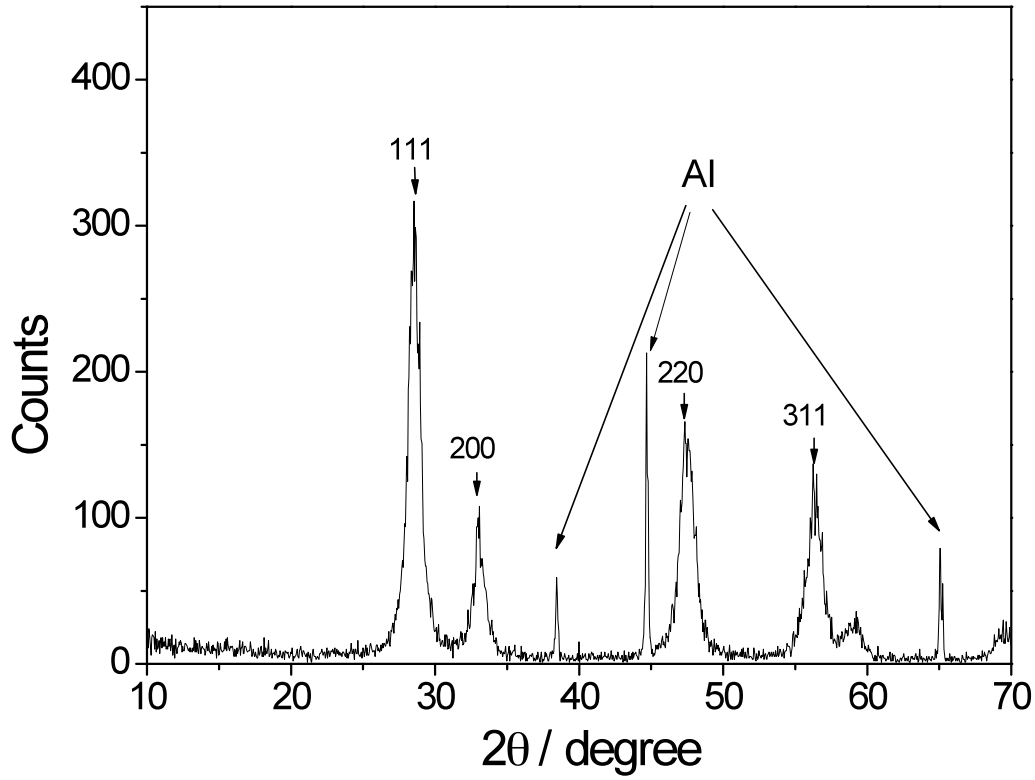

Figure 4.1 XRD patterns of MCE02 sample synthesized by the microemulsion method.

Crystalline ceria is indicated by the XRD pattern with the major peaks assigned to CeO_2, contributing to the 2θ degree 28.6 (111), 33.1 (200), 47.5 (220) and 56.3 (311), are clearly observed [8]. By collecting the FWHM value from each peak and then calculating using the Scherrer equation, the average particle size of this MCE02 sample is determined to be 9.9 nm. TEM is also used to characterize the nano-particulate nature of the sample. Figure 4.2 shows the TEM image of MCE02.

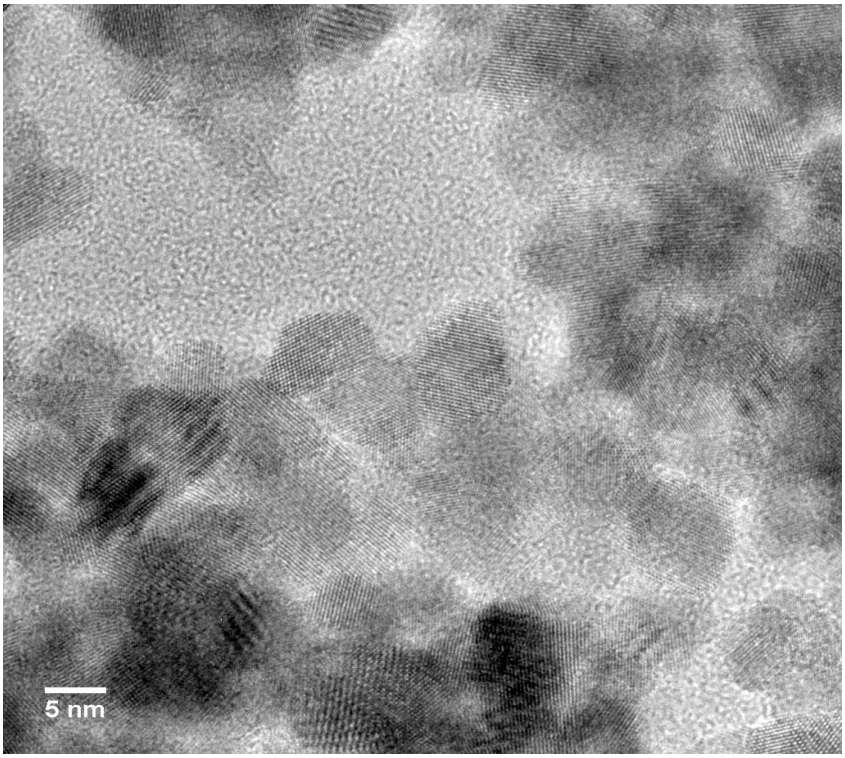

Figure 4.2 TEM image of MCE02.

In Figure 4.2, it shows a typical electron micrograph of the cerium oxide nanoparticles prepared by the microemulsion method (MCE 02). It demonstrates the single-crystalline nature of our product, and the nearly spherical (faceted), highly crystalline ceria particles. This sample mainly composed of the (111) planes, which is expected because the (111) plane is considered to be the most stable phase of CeO_2 [9,

10], which is also correlated with the sharp 111 peak in the XRD pattern.

There is a degree of particle aggregation of ceria sample as shown in the TEM image of Figure 4.2, but by careful identification of individual particles from TEM images, a narrow size distribution is recorded (Figure 4.3).

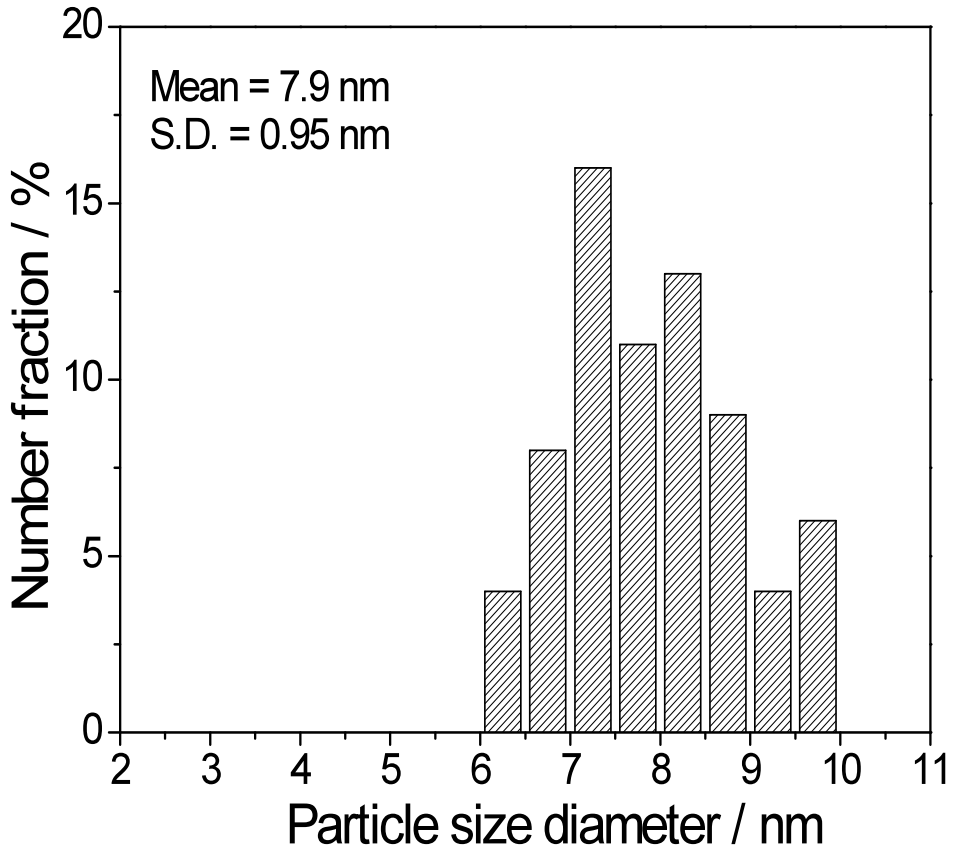

Figure 4.3 The size distribution histogram collected from TEM of MCE02.

From analysis of more than 70 particles from the sample, the mean size of MCE02, determined by TEM microscopy, is 7.9 nm, matching excellently with those determined by XRD using the Scherrer equation. The value seems to be slightly larger than the TEM data, most probably due to the agglomeration observed in the micrographs. However, it can be concluded that by the microemulsion synthesis method, the nano size ceria is successfully synthesized.

4.2.2 Size Distribution of Ceria Nanoparticles

It is reported that adjusting the synthetic parameters of the microemulsion method leads to the formation of smaller ceria particles [6, 7]. The key synthetic parameters include: (1) the ratio of water to surfactant (Triton® X-100), (2) the ratio of water to co-surfactant, (3) the concentration of cerium precursor (cerium (III) nitrate hexahydrate) and (4) water to oil phase ratio (*n*-Heptane). We attempted to synthesize a series of nano ceria particles with different sizes by adjusting these parameters. Figure 4.4 shows the XRD patterns of the produced ceria samples.

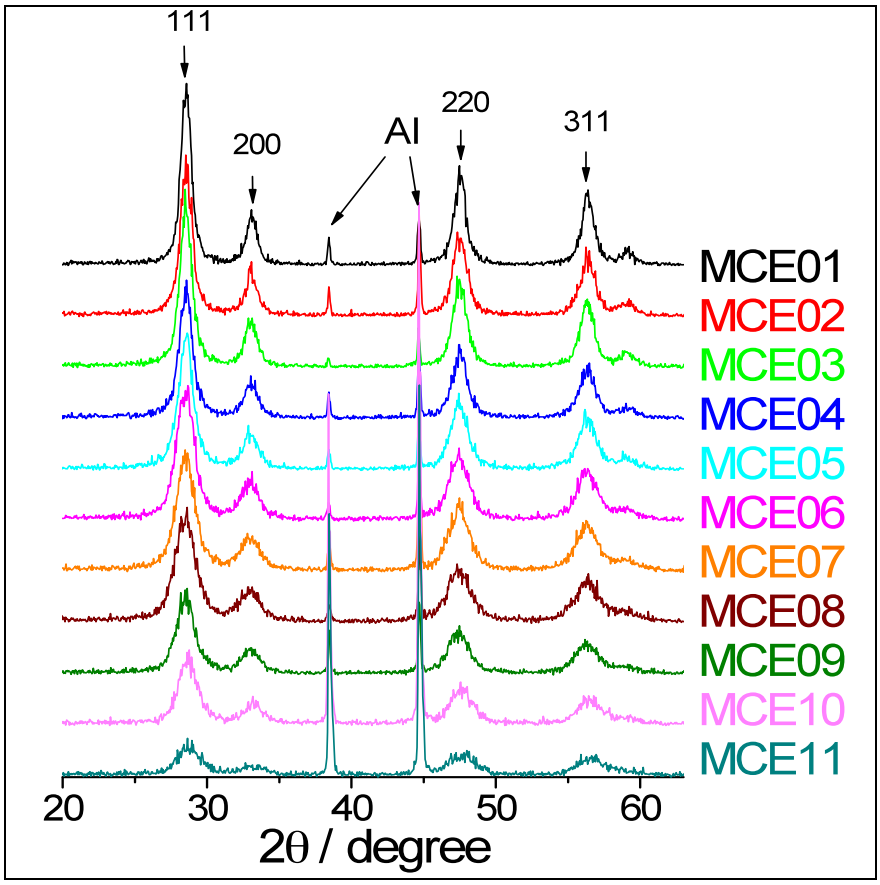

Figure 4.4 XRD patterns of nano ceria synthesized by the microemulsion method.

In Figure 4.4, all the samples agree well with the presence of a cubic fluorite-type phase. The typical CeO_2 peaks are observed with the relatively large line width. It is ascribable to the presence of small crystallites formed after calcination at 773 K [11]. Table 4.1 lists the samples with the different particle sizes, calculated from the XRD patterns by the Sherrer equation, and their related synthetic parameters.

Table 4.1 Synthesis conditions and particle size of ceria samples

Sample	Particle size /nm	Ce conc. / (mol/L)	$[H_2O]/[Oil]$ (w/w)	$[H_2O]/[Surfc.]$ (w/w)	$[H_2O]/[co\text{-}Surfc.]$ (w/w)
MCE01	12.5	0.5	15/30	15/38	15/30
MCE02	9.9	0.5	8/58	8/19	8/30
MCE03	9.4	0.5	8/116	8/19	8/30
MCE04	8.5	0.5	8/116	8/38	8/30
MCE05	7.8	0.25	8/116	8/38	8/60
MCE06	6.0	0.5	5/58	5/38	5/30
MCE07	5.8	0.25	5/58	5/38	5/30
MCE08	5.3	0.1	5/58	5/38	5/30
MCE09	5.1	0.1	5/116	5/76	5/60
MCE10	4.9	0.25	1/58	1/38	1/30
MCE11	4.4	0.05	5/58	5/38	5/30

As a result, by adjusting the ratios of reagents it is possible to vary the particle size of the nano ceria without changing the thermal treatment conditions. A series of nano ceria with particle sizes ranging from 12.5 to 4.4 nm have been made, and the particle size of nano ceria decreases gradually.

The TEM characterization was performed for the size distribution analysis in these ceria samples. Figure 4.5 shows two more typical high-resolution electron micrographs of the ultrafine ceria particles prepared by the microemulsion method with different particle size.

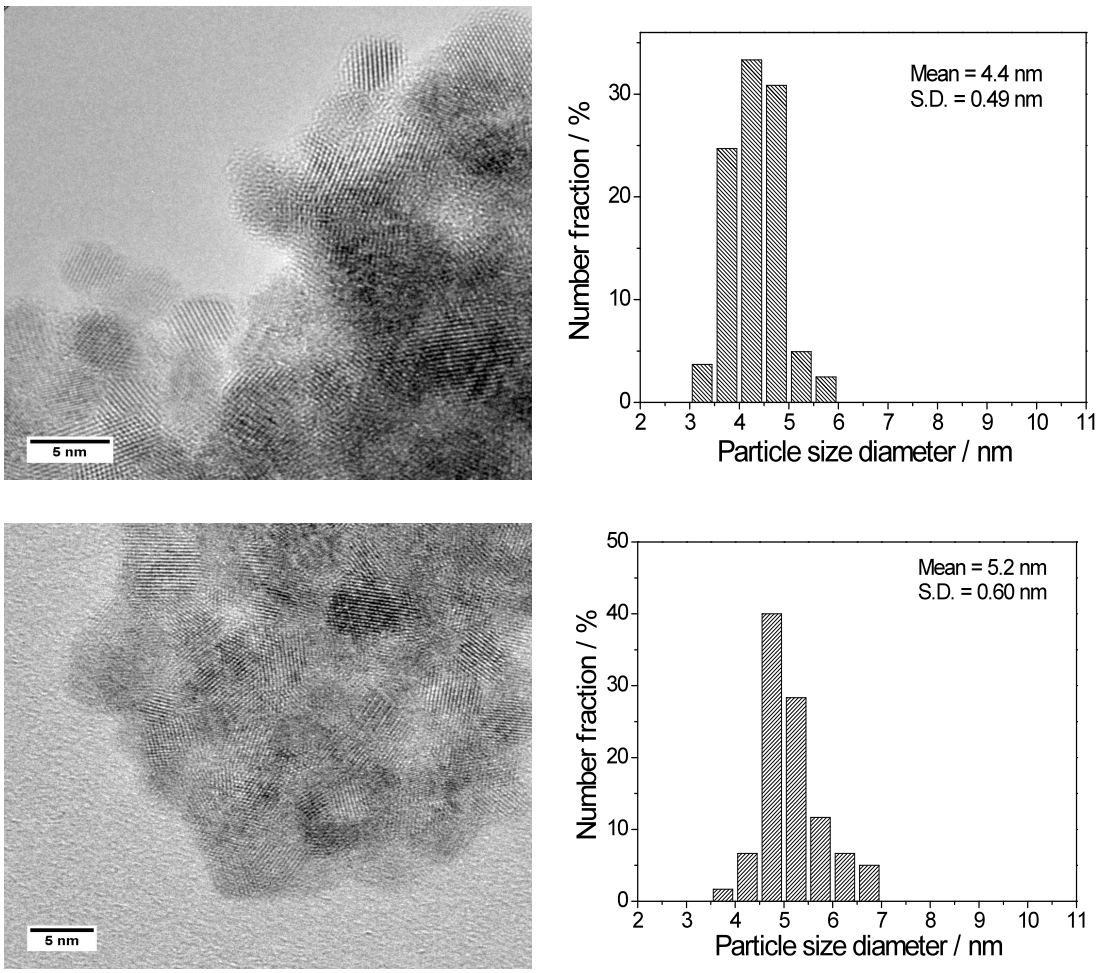

Figure 4.5 (a) Upper: A typical TEM of ceria particles MCE11 with the particle size distribution histogram; (b) Bottom: TEM of MCE08 with the size distribution histogram.

Figure 4.5a demonstrates that the highly crystalline ceria nanoparticles after the calcination were collected as our product MCE11. It is nearly spherical (faceted) and there is a degree of particle aggregation. By the careful identification of individual particles from TEM images, a narrow size distribution of these particles is evident. The mean particle size of the sample MCE11 from the TEM microscopy is 4.4 nm, which matches well with those determined from the XRD patterns using the Scherrer equation (seen in Table 4.1). Figure 4.5b shows the similar electron micrograph of the cerium oxide nanoparticles with a single crystalline nature. In Figure 4.5b, the mean size of MCE 08 from the TEM image is 5.2 nm, matching the XRD result of 5.3 nm.

In conclusion, both the XRD patterns and the TEM images of the products are consistent to confirm that the ceria nanoparticles are synthesized by the modified microemulsion method and a series of ceria nano crystals with different particle sizes are successfully achieved.

4.3 Size Effect for the Structure of Ceria Nanoparticles

4.3.1 Lattice Expansion in Ceria Nanoparticles

Because of the small particle size, the peaks are broadened in XRD patterns. As a result, the selected area electron diffraction (SAED) is a more valuable technique for identifying the crystal structure of nano ceria particles. Figure 4.6 shows SAED patterns with the Debye-Scherrer rings of the nano ceria sample MCE02.

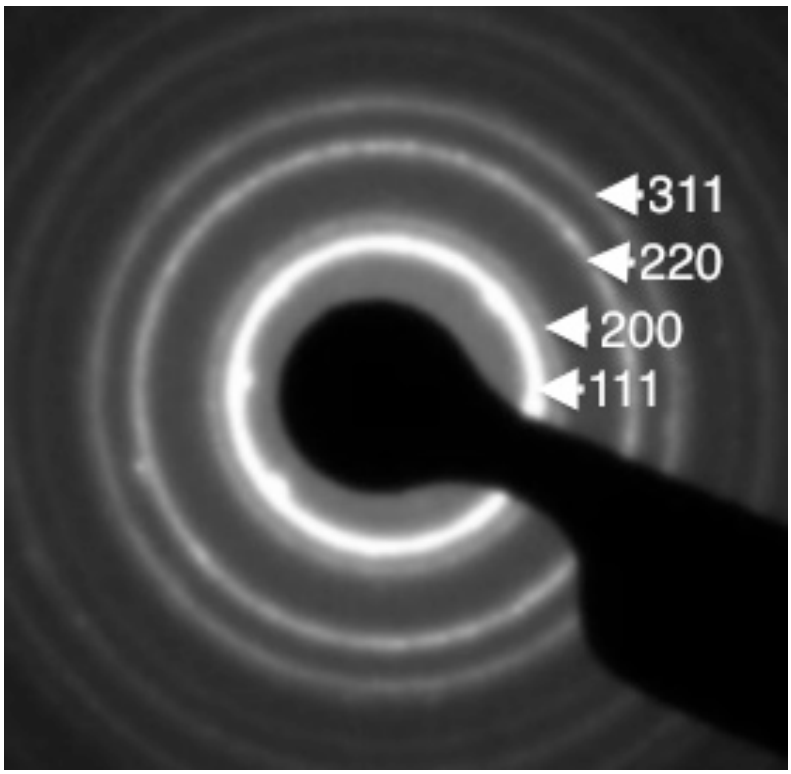

Figure 4.6 SAED pattern with the Debye-Scherrer rings from the sample MCE02

The lattice constants were carefully calculated from the SAED patterns. They can be consistently indexed as those of cerium (IV) oxide with the cubic fluorite structure [6]. The lattice constant calculated from the radii of rings of MCE02 is 0.5417 nm and

it is in a good agreement with that given in the literature [5] even slightly greater than the bulk value of 0.5411 nm [12]. The lattice parameters are collected from the SAED patterns of the sample MCE08 with the particle size 5.3 nm as well as the sample MCE11 with the particle size 4.4 nm with the number 0.5429 nm and 0.5459 nm.

The XRD patterns of the nano ceria samples are also refined by the Rietveld method (details in Chapter 2) and a plot of lattice constant versus particle size is shown in Figure 4.7. In the refinement work, the error from the sample MCE10 with the particle size 4.9 nm and MCE11 with the particle size 4.4 nm is higher than 15%, so the results of them are not presented in this figure. The lattice constants collected from SAED results are also shown in Figure 4.7.

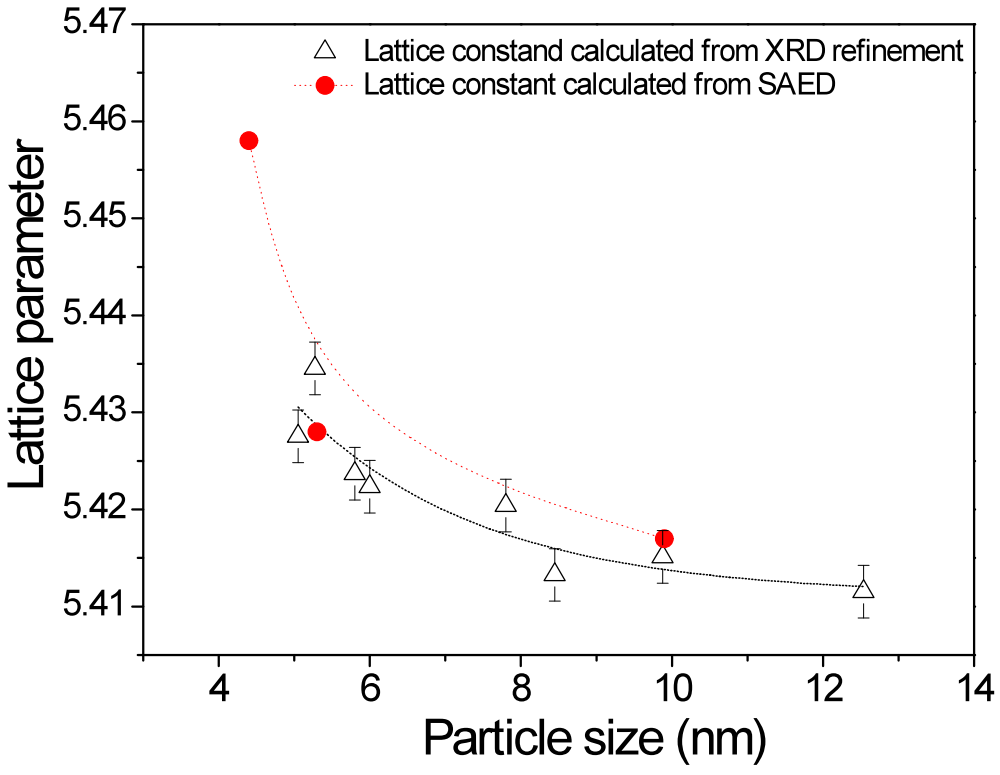

Figure 4.7 Size dependent lattice parameter of nano ceria (from XRD refinement results by Rietveld method, and SAED patterns).

In Figure 4.7, it is clear to see the size dependence of the lattice parameters in our samples from the XRD refinement results (black triangle and the solid line), and that though the expansion of the lattice expansion approaches 0.42% at the sample MCE09 with 5.1 nm compared with the bulk CeO_2 sample (0.5411 nm) [13], the fluorite lattice persists even at this size. It is also shown that the lattice parameters collected from SAED (red circles with a dotted line) of the smaller size nano ceria match well with the XRD refinement results, and that the lattice expansion of nano ceria critically increases when the particle size decreases below 5 nm. This confirms the results of the previous study that the lattice parameter increases as the nano ceria particle size decreases [7, 13].

Raman spectroscopy is also used as a characterization technique to probe the local structure of various ceria nano and Figure 4.8 depicts the Raman spectra of some selected samples.

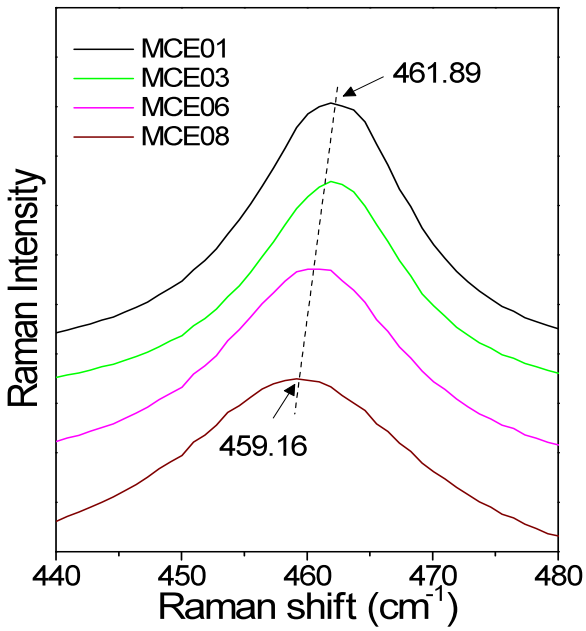

Figure 4.8 Raman spectra of the nano ceria showing a progressive red shift of F_{2g} mode at decreasing particle size.

Fluorite structure metal oxides only have a single allowed Raman mode, which has F_{2g} symmetry and which can be viewed as a symmetric breathing mode of the O atoms around each cation. Since only the oxygen atoms move, the mode frequency should be nearly independent of the cation mass [14]. In the ceria, this frequency was reported between 453 and 454 cm^{-1} attributed to a symmetrical stretching mode of Ce-O8 vibrational unit [15]. In our sample MCE01, the peak contributed to F_{2g} mode was found at 461.89 cm^{-1}. This difference between our data and the reference one should be due to the error from the silicon calibration from the equipment. As shown in Figure 4.8, the peak at 461.89 cm^{-1} of MCE01 with the particle size 12.5 nm shifts to lower energy 459.16 cm^{-1} of the sample MCE08 with the particle size 5.3 nm. Table 4.2 summarize the major peak position and the half width of the band from different particle size ceria samples.

Table 4.2 Relative Raman peak to the different particle size ceria synthesized by the microemulsion method.

Samples	**Particle size (nm)**	**Raman results**	
		Raman frequency (cm^{-1})	**Half-width (cm^{-1})**
MCE01	12.5	461.89	16.98
MCE02	9.9	461.89	16.20
MCE03	9.4	461.89	16.64
MCE04	8.5	461.89	19.62
MCE05	7.8	461.40	19.62
MCE06	6.0	460.69	21.87
MCE07	5.8	460.00	30.82
MCE08	5.3	459.16	29.92

From Figure 4.8 and Table 4.2, it is noted that a red shift of the Raman peak at 462 ~ 459 cm^{-1} is found when the particle size is smaller than 8 nm. This conclusion is similar to that in the work by Hernández-Alonso *et al*. [7]. As seen in Table 4.2, the Raman peak broadens from 16.98 to 29.92 cm^{-1} as the particle size decreases from 12.5 nm to 5.3 nm respectively.

Several factors can contribute to the observations of the changes in the Raman peak position and the broadening linewidth associated with the decreasing size of the nano ceria [14-17]. These include phonon confinement, strain, broadening associated with the size distribution, effects and variations in phonon relaxation with particle size. And various models of Raman scattering have been reported by researchers to explain the peak shift and the line broadening [14-21].

The increasing lattice parameter (strain relative to the bulk) measured for decreasing particle size can explain the Raman shift and the line width broadening well [16, 17]. Furthermore, it is assumed that the strain comes from the presence of Ce^{3+} ions and oxygen vacancies by providing the estimates of the oxygen vacancy concentration [14, 16, 17] but other effects such as the surface stress (increasing surface energy) are not taken into account [22].

The formation and transport of oxygen vacancies is pivotal for many of the reactions, which happens on ceria catalysts. And it is thought that this improvement of catalyst efficiency was caused by the higher concentration of oxygen vacancies, which is size dependent, as well as changes in structural, electronic, and lattice vibrational properties [1]. It is proposed [10, 13, 23, 24] as a result of the sharp increase in the concentration of oxygen vacancies when the ceria particle size reduces below 10 nm. In this chapter, the results from XRD, SAED and Raman match well and confirm the lattice expansion in the smaller nano ceria. However, the hypothesis

to connect the lattice expansion in consequence of the increase in oxygen vacancies of the MCE samples still needs some more evidence.

4.3.2 Oxygen Vacancy on Nano Ceria Surface

It is well known that the oxygen vacancy in ceria is formed by the following reaction:

$$2\,Ce^{4+} + O^{2-} \Leftrightarrow 2\,Ce^{3+} + V_o + \tfrac{1}{2}\,O_2 \qquad (4.1)$$

where V_o is an oxygen vacancy. Ceria crystallizes in the fluorite structure, in which the Ce^{4+} cation is surrounded by eight equivalent O^{2-} ions forming the corner of a cube, with each O^{2-} coordinated to four Ce^{4+}.

Due to the introduction of oxygen vacancies by Equation 4.1, Ce^{3+} species are introduced into the lattice positions previously occupied by Ce^{4+} [25]. The radius of the Ce^{3+} ion is larger than that of Ce^{4+} (1.14Å *vs* 0.97Å, according to the data of Shannon and Prewitt [26]). The introduction of the oxygen vacancies and the accompanying Ce^{3+} ions leads to a distortion of the local symmetry. This causes the change in the Ce-O bond length (lattice distortion) and the overall lattice parameter [24]. So the lattice expansion is commonly interpreted as a consequence of reduction of Ce^{4+} ions to Ce^{3+}.

Because such a lattice expansion effect is generally believed to be a result of the increase in Ce^{3+} concentration in the nanocrystal as the particle size decreases, as well as oxygen vacancies [13, 27-30]. As a result, the Ce^{3+} concentration in the nano ceria with smaller particle size should be greater than in ceria with larger particles. In order

to validate this hypothesis, x-ray photoelectron spectroscopy (XPS) [24, 31] was carried out to detect the changes in the surface valence of nano ceria MCE samples. Figure 4.9 shows the cerium $3d_{3/2}$ and cerium $3d_{5/2}$ x-ray photoemission spectra for the samples with different particle sizes from 9.9 nm to 4.4 nm.

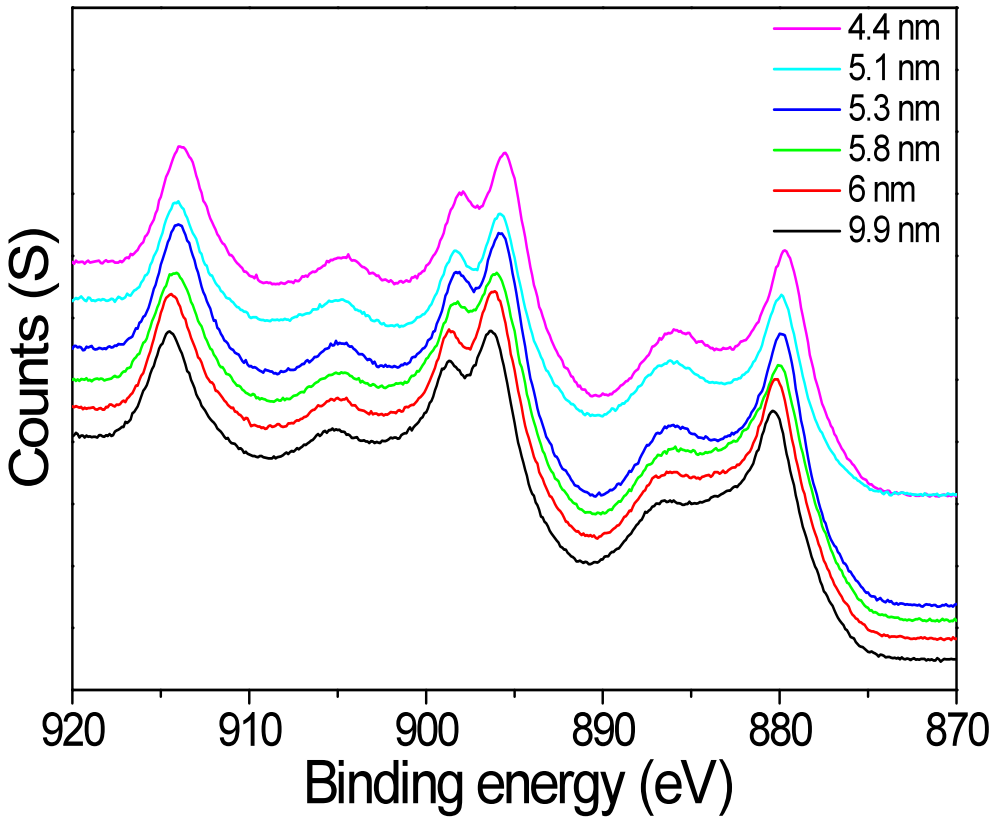

Figure 4.9 Ce 3d XPS spectrum for ceria samples with different particle sizes.

In Figure 4.9, the Ce 3d XPS spectra of the MCE samples have a similar shape to the spectrum from the reference of CeO_2 [24]. It is noted that as the nano ceria particle size decreases, a shift to lower binding energy of the Ce 3d spectra is observed, which is attributed to the lattice expansion on the surface of smaller particles in a similar manner to the red shift observed in the Raman spectra [17, 31].

Figure 4.10 shows possible individual contributions to peaks under optimized conditions (MCE11 with the particle size 4.4 nm as the example).

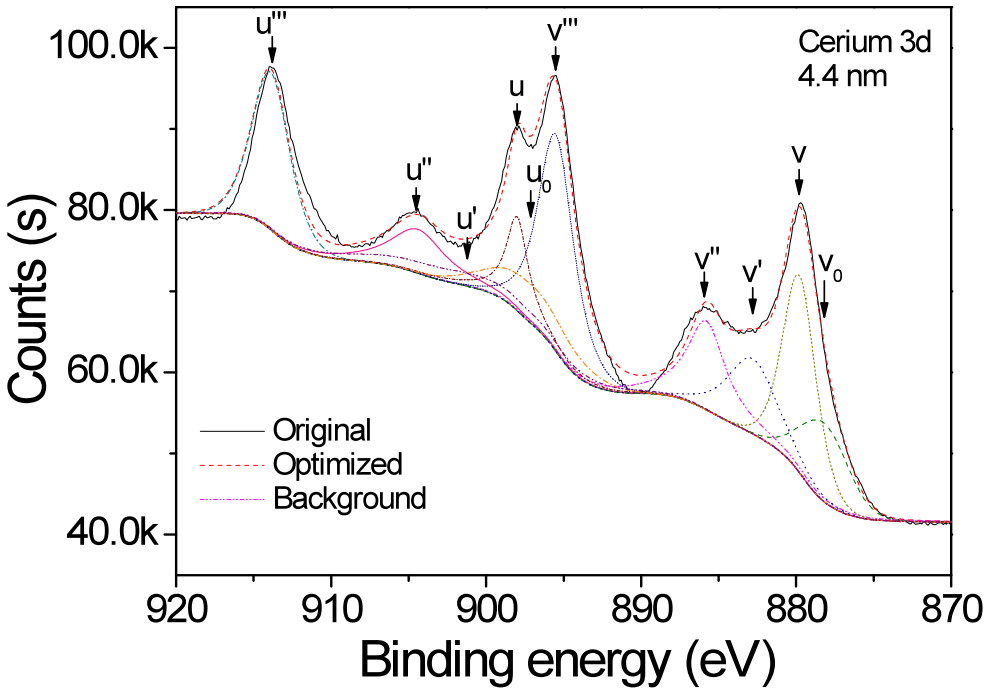

Figure 4.10 The possible individual contributions, peaks denoted by the subscripts v and u assigned to $3d_{5/2}$ and $3d_{3/2}$ states respectively.

Cerium compounds are known to exhibit rather complex XPS features due to hybridization with ligand orbitals and fractional occupancy of the valence 4f orbitals. Since the initial work of Burroughs *et al.* [32], it has been demonstrated that the Ce 3d XPS spectrum of a Ce^{4+} compound can be resolved into six structures and if some Ce^{3+} species are also present, four more structures are added [33, 34]. As shown in Figure 4.10, the denotation by the subscripts v and u are assigned to $3d_{5/2}$ and $3d_{3/2}$ states respectively. v_0, v', u_0, and u' peaks are attributed to Ce^{3+}; while v, v'', v''', u, u'', and u''' are characteristic of Ce^{4+}. The same peak fitting was done for the XPS spectra of other MCE samples with different sizes. The peak positions for all the samples are listed in Table 4.3.

Table 4.3 XPS binding energies of individual peaks for the Cerium 3d spectrum of different ceria nanoparticles.

Particle Size / nm	Ce^{4+}						Ce^{3+}			
	v	v''	v'''	u	u''	u'''	v_0	v'	u_0	u'
9.9	880.3	886.5	896.2	898.7	905.3	914.5	878.7	883.3	897.6	902
6	880.2	886.4	896.1	898.7	905.3	914.4	878.6	883.3	897.7	902
5.8	880	886.1	895.85	898.4	904.7	914.1	878.5	883.6	897.45	901.6
5.3	879.9	886	895.8	898.2	904.9	914	878.4	883	897.3	901.3
5.1	879.8	885.8	895.5	898	904.4	913.9	878.2	882.8	897.1	901.1
4.4	879.8	885.8	895.5	898	904.4	913.9	878.2	882.8	897.1	901.1

It is accepted that XPS is a surface technique but the electron escaping depth should allow a deep analysis of the nano ceria samples. A semi-quantitative analysis of the integrated peak area can provide the concentration of Ce^{3+} ions in the synthesized nanoparticles. It can be calculated accordingly [34]:

$$[Ce^{3+}] = \frac{A_{v0} + A_{v'} + A_{u0} + A_{u'}}{A_{v0} + A_{v'} + A_{u0} + A_{u'} + A_{v} + A_{v''} + A_{v'''} + A_{u} + A_{u''} + A_{u'''}}, \quad (4.2)$$

where A_i is the integrated area of peak "i". The results of the concentration for Ce^{3+} are summarized in Table 4.4.

Table 4.4 Concentration of Ce^{3+} as a function of nano ceria particle size calculated using Equation 4.2.

Samples	**MCE02**	**MCE06**	**MCE07**	**MCE08**	**MCE09**	**MCE11**
Size (nm)	9.9	6	5.8	5.3	5.1	4.4
Ce^{3+} Corn. (%)	29.4	28.8	27.9	27.6	27.9	29.5

In Table 4.4, it is surprising to note that the concentration of Ce^{3+} does not significantly change with particle size. This result disagrees with the results reported by Deshpande *et al.* [24] in 2005. In their work, Ce^{3+} concentration increased with a decrease in the particle size of nano ceria.

With the synthesis of nano ceria, depending on calcination and treatments, the formation of Ce^{3+} and oxygen vacancies are not anticipated to be the same. However, the XPS results of MCE samples show there was no significant change in Ce^{3+} concentration for nano ceria with different particle sizes under identical preparation and heat treatment, whereas a change in lattice parameter was truly recorded from XRD and SAED results.

Due to the similar Ce^{3+} concentration in our nano ceria MCE samples with different particle sizes, the oxygen vacancy ratios should not be significantly different. So in the MCE samples, the increase of the lattice parameter with decreasing particle size cannot be attributed to the creation of more oxygen vacancies and the introduction of larger Ce^{3+} ions into the ceria crystal structure. Therefore the lattice expansion should be attributed largely to the strain effect created from the increasing surface energy of ceria with smaller sizes.

4.4 Surface Oxygen Species of Nano Ceria

4.4.1 Surface Oxygen Species Detected from XPS

The ability to adsorb and release oxygen plays a critical role in the overall performance of the catalytic activities of ceria, and the surface oxygen species are the important intermediates in many redox reactions [35]. An XPS study of O 1s on the surface of the different particle sizes samples are shown in Figure 4.11.

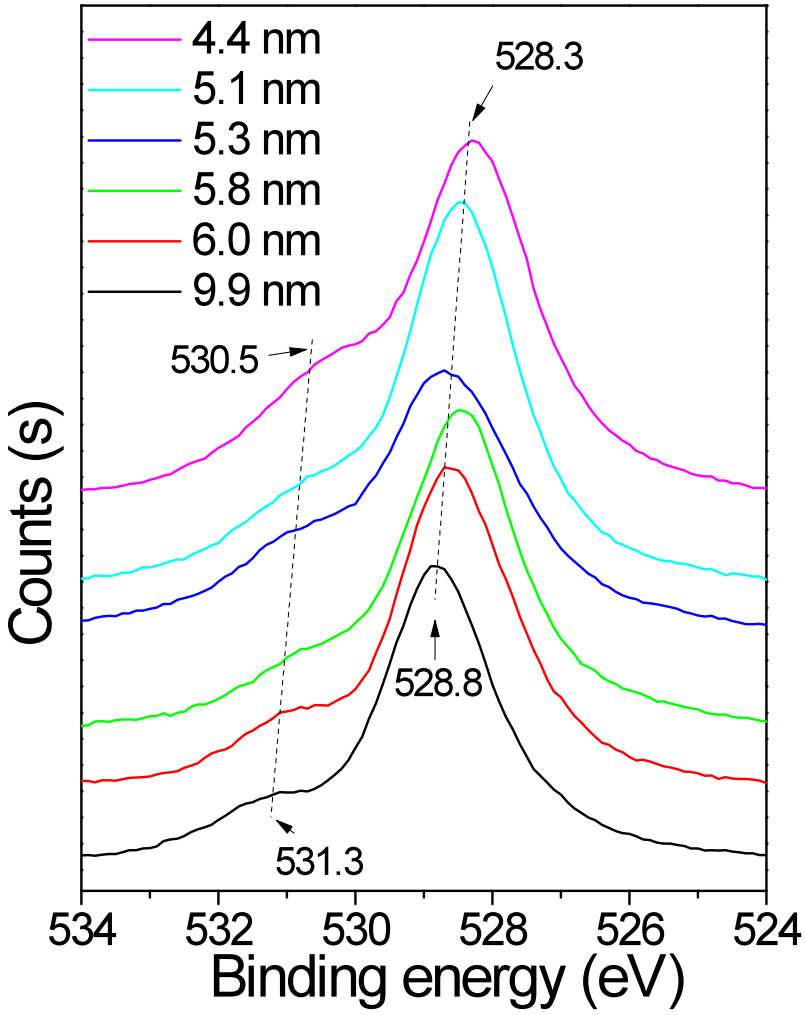

Figure 4.11 Oxygen **1s** photoemission spectra for samples with different particle sizes.

The O 1s spectra show two main peaks. The first peak in the low binding energy at 528 eV is attributed to oxygen anion in the lattice [36, 37]. The second oxygen peak in the higher binding energy, at 530 to 532 eV, can be attributed to the oxygen species formed on the surface of ceria [37-39]. Reducing ceria particle size from 9.9 nm to 4.4 nm, both peaks shift to lower binding energy, which is consistent to the Ce 3d spectra in Figure 4.9.

The O 1s spectra is fitted with two components using curve fitting and Figure 4.12 shows the curve fitting procedure of the sample of 4.4 nm.

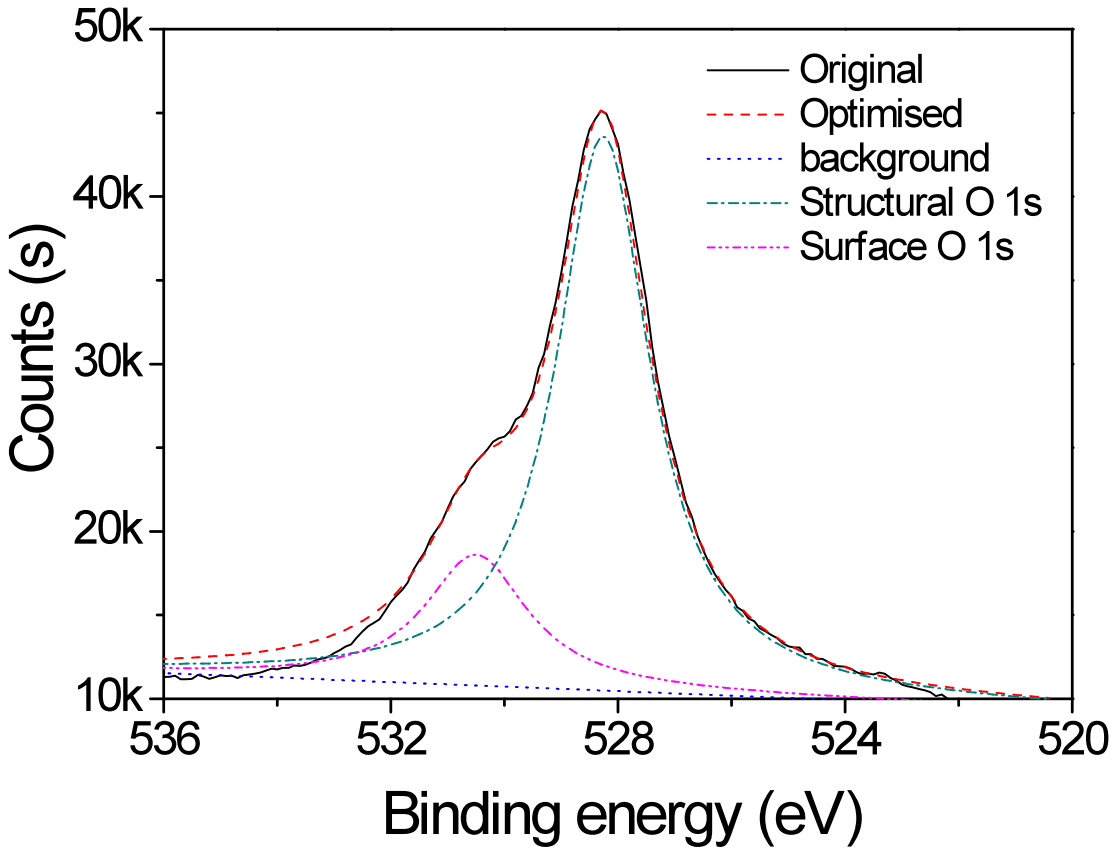

Figure 4.12 Oxygen **1s** photoemission spectra for the sample with the particle size 4.4 nm. The binding energy of the shouldered surface oxygen peak is found to be 531 eV, matching the literature value of superoxide species [36].

All the nano ceria samples with different particle sizes are fitted by the same method, and the fitted results are summarized in Table 4.5.

Table 4.5 XPS analysis of the O **1s** spectra for different ceria nanoparticles samples: binding energy and oxygen ratio.

Particle size	**Surface oxygen species**		**Lattice oxygen anions**	
(nm)	**BE (eV)**	**A_{surf} (%)**	**BE (eV)**	**A_{latt} (%)**
9.9	531.3	3.14	528.8	96.86
6	531.13	7.07	528.6	92.93
5.8	531	8.55	528.5	91.45
5.3	531	12.4	528.6	87.6
5.1	530.9	13.7	528.5	86.3
4.4	530.5	20.5	528.3	79.5

Comparing the ratio of the surface oxygen species and the lattice oxygen anions, it is clear to see that the surface oxygen fraction increases with decreasing particle size of the nano ceria. This is as expected because of the obvious geometric effect: the smaller sized nano ceria should have more surface ratio compared with bigger one. However, it is interesting to note from Table 4.5 that the decrease in lattice oxygen (528.8 eV) matches with new broad surface oxygen peak at binding energy 531 eV. The broad peak grows in size and gradually shifts to slightly lower binding energy (*ca*. 2eV above lattice oxygen) at the lowest size. This new peak position has been previously observed and there has been debate [40, 41] concerning the exact origin of such peaks, and it has been ascribed to superoxide species [41], which are reported as

the extremely active surface oxygen species for several catalytic oxidative reactions [35]. So it is very important to clarify the surface oxygen species from the MCE samples.

4.4.2 H_2-TPR Investigation of Oxygen Species

The redox properties of nano ceria samples were investigated by H_2-TPR technique. In Figure 4.14, the temperature programmed reduction profiles from ambient temperature to 1000 ^oC at 10 ^oC/min of the samples were collected.

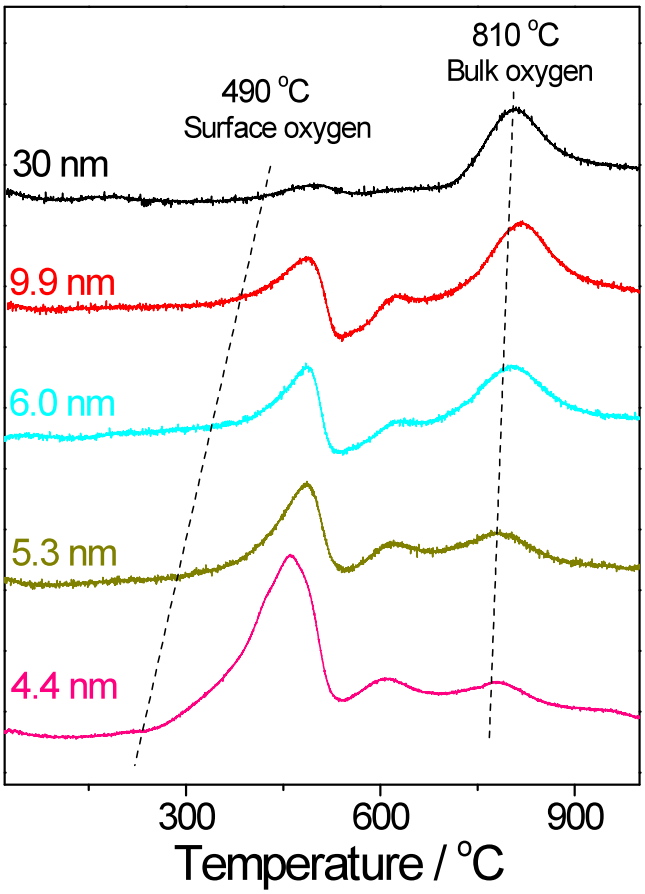

Figure 4.13 H_2-Temperature Programmed Reduction (TPR) profiles of nano ceria with different sizes.

At the end of the run, all ceria was reduced to the boundary state of Ce_2O_3 as indicated by XRD [42]. As seen from Figure 4.13, two types of reducible oxygen are clearly observed in the bulk ceria (30 nm). The first peak at around 490 ^oC corresponds to reduction of the "surface" oxygen with lower activation energy. The second peak at approximately 810 ^oC can be attributed to the reduction of the "bulk" oxygen, which was likely arisen from slow lattice oxygen diffusion [43].

The nano ceria samples show similar peak profiles, but a new oxygen reduction peak at 630 ^oC can be seen. The nature of this peak is not yet known, but the quantity is below 5% of the total extractable oxygen. It could be assigned to a slightly more facile reduction mechanism of extracting oxygen from the lattice with a specific crystallographic orientation [1].

There is also a slight but progressive shift to the lower temperature in both the surface and the bulk oxygen with decreasing particle size, indicating that the two reduction progresses are marginally facilitated at the smaller sizes. However, it is very interesting to note the dramatic increase in the surface oxygen peak at the expense of bulk oxygen when the particle size decreases. Table 4.6 summarizes the reducible oxygen value calculated from the TPR profiles of the nano ceria samples.

Table 4.6 Reducible oxygen of ceria samples from TPR profiles.

Size (nm)	Oxygen calculated from TPR				
	$[O]_{Surface}$		$[O]_{Bulk}$		$[O]_{total}$
	Amount (mmol/g)	**Ratio (%)**	**Amount (mmol/g)**	**Ratio (%)**	**(mmol/g)**
9.9	0.30	39.90	0.42	56.18	0.74
8.5	0.35	48.69	0.34	47.43	0.72
7.8	0.36	50.86	0.33	45.64	0.72
6.0	0.37	51.43	0.31	43.49	0.72
5.8	0.47	64.05	0.25	33.93	0.73
5.3	0.50	66.85	0.23	31.09	0.75
5.1	0.59	68.1	0.23	26.74	0.87
4.9	0.78	73.4	0.19	17.86	1.06
4.4	0.98	80.2	0.17	13.52	1.22

As Table 4.6 shows, the total reducible oxygen content of these ceria samples remains virtually unchanged from 9.9 nm to 5.8 nm (0.73 ± 0.01 mmol/g), suggesting that all the hydrogen is consumed in the reduction of oxygen species with no adsorption or desorption of hydrogen during the TPR. Furthermore, as previously stated, the general postulation for the formation of the large size Ce^{3+} from the Ce^{4+} with the introduction of oxygen vacancies (especially on the surface) of decreasing size, as an explanation for lattice expansion, could not be credited in the results from the work of this chapter. It contradicts the observation that the total reducible oxygen content showed absolutely no decrease (when in fact there was an increase of less than 5.3 nm).

Figure 4.14 shows clearly the inverse relationship between surface oxygen and bulk oxygen as a function of size.

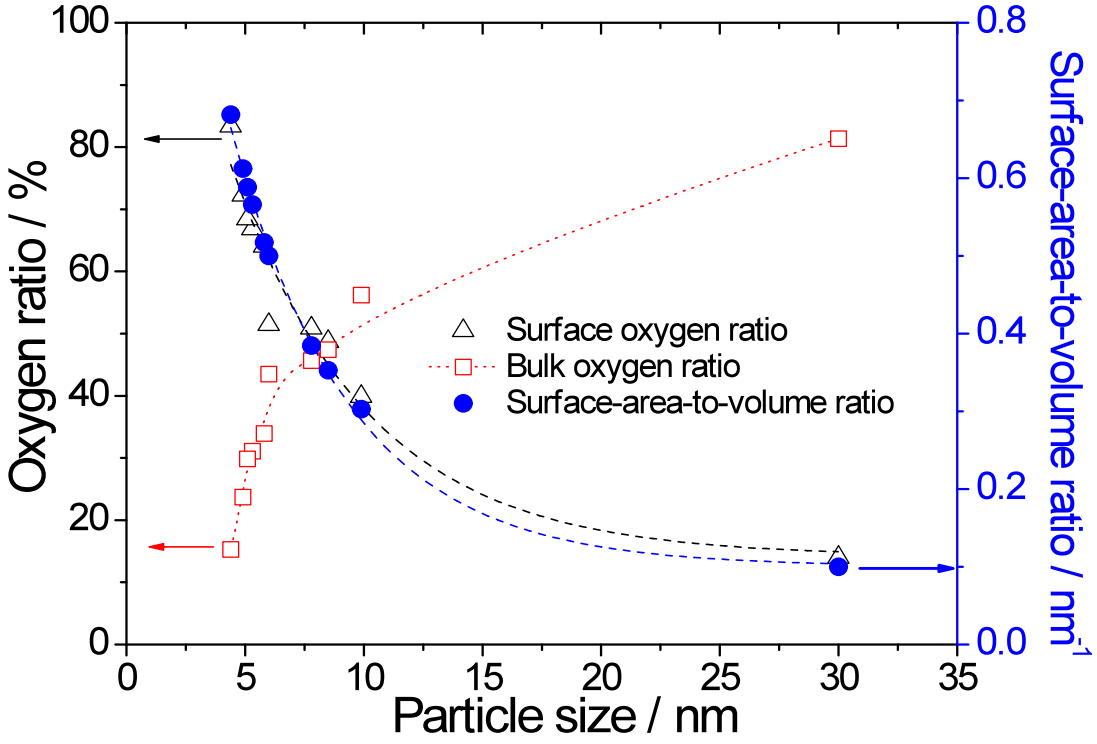

Figure 4.14 The inverse relationship of surface oxygen to bulk oxygen and the correlation of surface oxygen ratio with theoretical surface to volume ratio.

In Figure 4.14, the black line is the surface oxygen ratio calculated from TPR results, and the blue line is the theoretical surface to volume ratio (assuming nano ceria is a spherical particle as shown in TEM images). The surface oxygen ratio matches extremely well with the theoretical surface to volume ratio change as a function of size. Thus, the main effect of decreasing the particle size appears to increase the surface oxygen at the expense of bulk oxygen, which means increasing the amount of exposed co-ordinately structural oxygen ions at the surface.

Surprisingly, when the particle size reduces below 5.3 nm (particularly at 4.4 nm), the surface oxygen reduction peak area is drastically enhanced in comparison to all the other samples. The total sum of reducible oxygen is clearly higher than the constant total value (Table 4.6). It is also shown that the surface oxygen reduction peak becomes broadened, shifts towards the lower temperature and can be resolved into two sub-peaks. The Gaussian fit is done in the nano ceria samples with the particle sizes smaller than 5.1 nm (MCE11 with the particle size 4.4 nm as the example).

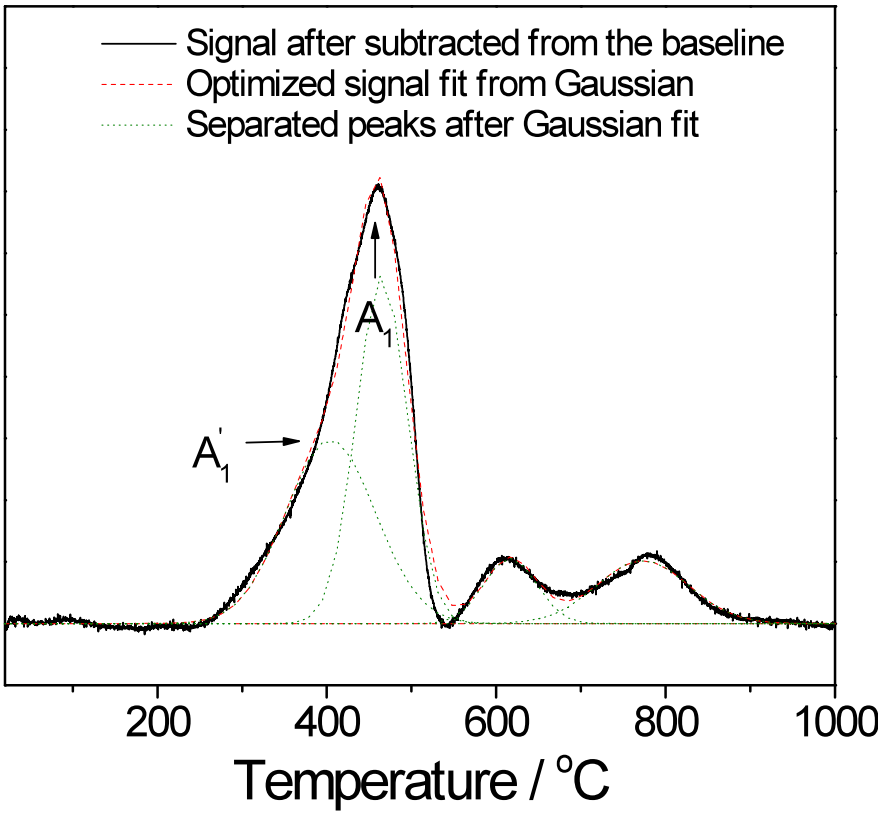

Figure 4.15 Gaussian fit H_2-TPR profiles of nano-ceria with the particle size of 4.4 nm. (For the samples with the particle size smaller than 5.1 nm, the surface oxygen peak is able to be separated into two peaks the first peak A_1' is at about 400 ^oC and the second peak A_1 is at 490 ^oC)

In Figure 4.15, the new oxygen species of the first sub-peak (A_1'), at about 400 ^oC, gives a distinguishable lower activation barrier than the second sub-peak (A_1), at about 490 ^oC, of the surface structural oxygen, which could quantitatively account for the oxygen enhancement (data are summarized in Table 4.7).

It is interesting to note a better correlation of Figure 4.7 (lattice parameter versus particle size by XRD and SAED) and Figure 4.14, indicating that the lattice expansion is likely related to the change of bulk to surface oxygen ratio. Concerning nano samples, the main effect of the decreasing size is to increase the surface to volume ratio, contributing to an overall decrease in the eight fold coordination of lattice oxygen to the cerium ions due to the surface non-stoichiometry, with tremendous strain created by the surface increase. This will lead to the lattice expansion. Likewise the formation of the unoccupied surface state/band gap states distortions due to the local strain at low dimensions [44] may also facilitate the activation of molecular oxygen air during calcination. Thus, identification and further quantification of the nature of the surface oxygen species formed at the lowest temperatures are important.

4.4.3 Quantification of Superoxides by EPR Technique

EPR analysis of ceria has been shown to yield important details on the nature and redox properties of ceria containing samples [45]. Figure 4.16 shows the EPR spectra of the nano ceria samples with particle sizes larger than 5.3 nm.

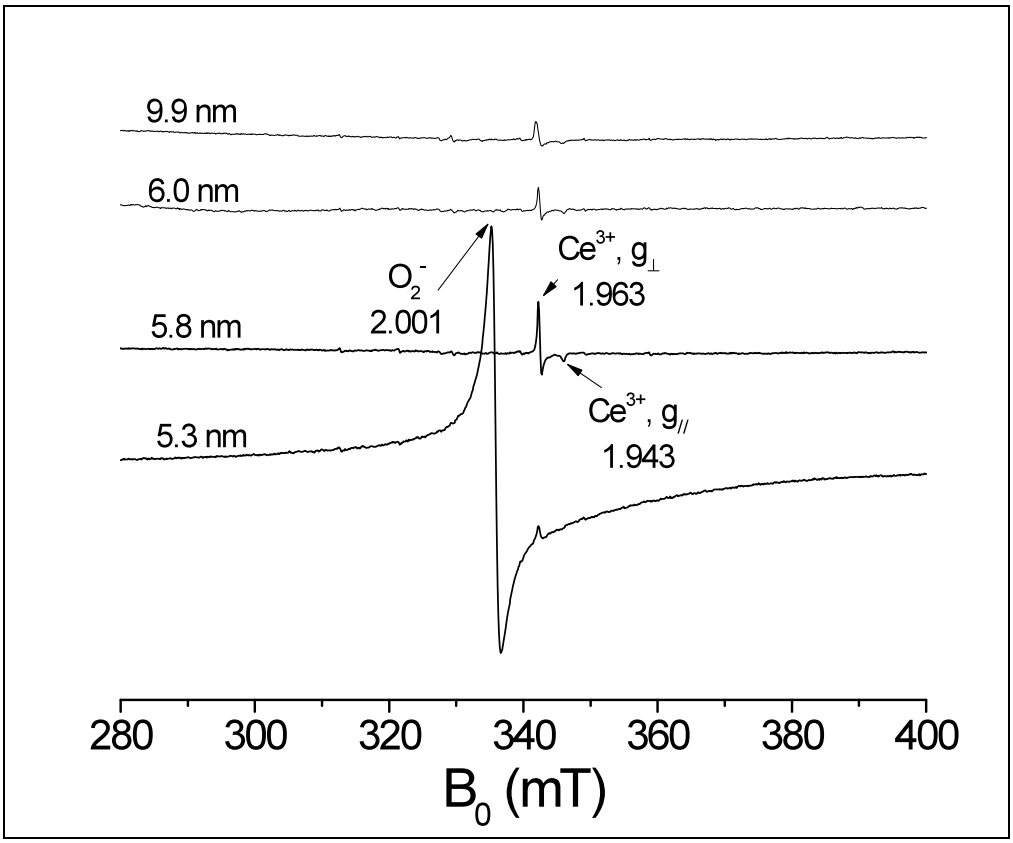

Figure 4.16 EPR spectra of nano ceria samples.

In Figure 4.16, when the nano ceria particle sizes are larger than 5.8 nm, the spectra clearly indicate the typical non-stoichiometric ceria at room temperature with the existence of Ce^{3+} the signals at $g_\perp = 1.963$ and $g_{//} = 1.943$ previously attributed to Ce^{3+} coupled with conduction electrons on ceria [46], a result consistent with the XPS data. There may be a slight fluctuation in the signal intensity of Ce^{3+} on the samples with

different particle sizes, but a quantitative analysis of this small peak proved to be difficult and the uncoupled Ce^{3+} EPR governed by 4f electrons normally requires the temperature below 20K to be visible [47].

A paramagnetic peak that was assigned to a radical with O_2^- character (g = 2.001, linewidth L_{pp} = 80 MHz in Figure 4.16) in the 5.3 nm ceria was also clearly observed at room temperature. The nature of this peak is believed to have arisen from the reaction $Ce^{3+} + O_2 \rightarrow Ce^{4+} + O_2^-$ [1]. The EPR spectra of the smaller size nano ceria and a simulation of the reported Ce^{3+} and Ce^{4+}-O_2^- are shown in Figure 4.17.

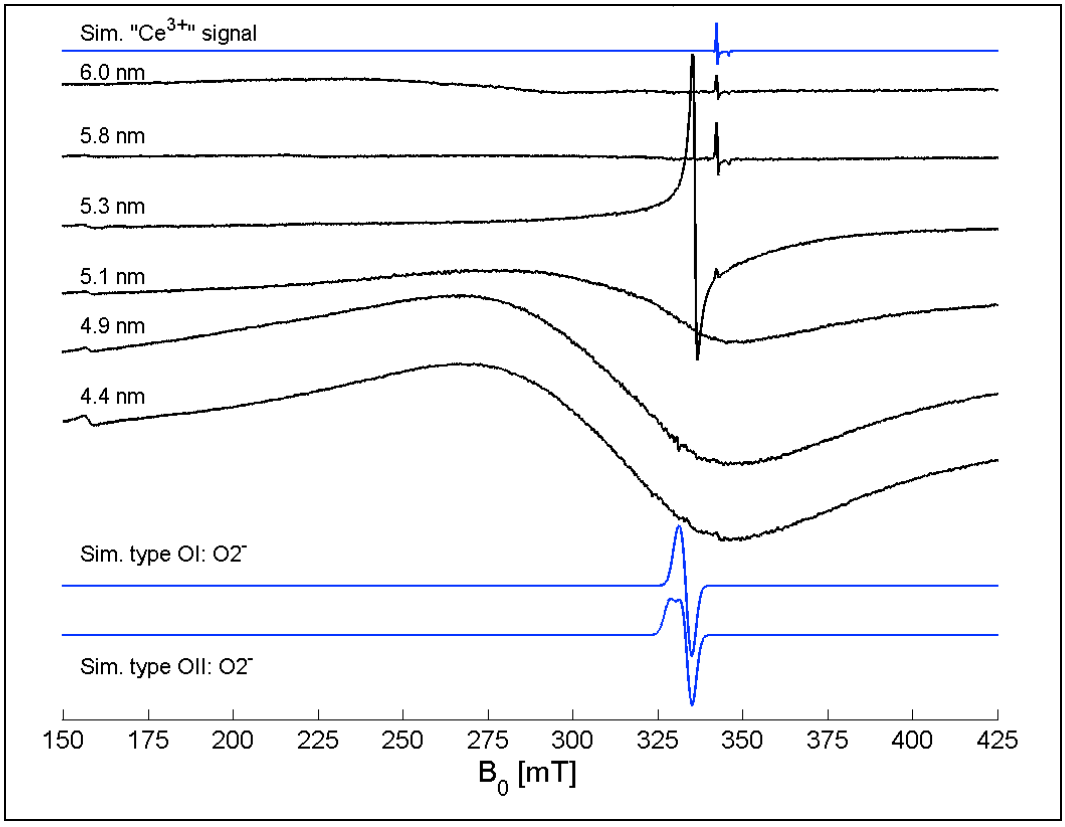

Figure 4.17 EPR spectra of ceria with different particle sizes showing the formation of superoxide surfaces at or below 5.3nm. Blue traces show simulations for the signal usually denoted as "Ce^{3+}" ($g_\perp$ = 1.963, $g_\parallel$ = 1.943) and for typical type OI ($g_\perp$ = 2.011, $g_\parallel$ = 2.032) and type OII (g_1 = 2.008, g_2 = 2.013, g_3 = 2.047) Ce^{4+}-O_2^- radicals [46, 48].

When the particle size decreased further to 4.4 nm, the Ce^{4+}-O_2^- type radical peak broadened significantly. As noted from the reported spectra in the literature [46, 48], the typical hyperfine couplings for the Ce^{4+}–O_2^- species should be < 80 MHz in the bulk ceria. Our broad linewidths and the high intensity g values collected clearly indicate significant coupling of the Ce^{4+}–O_2^- species on the surface of nano ceria, precluding their resolutions. This broadening is presumably due to the large electron-electron interactions at the higher coverage, hence concomitantly decreasing electron relaxation times [49]. The large electron-electron interactions are attributed to depend on the oxygen defect concentration and defect clusters [25].

The quantitative analysis of the O_2^- by the careful calibration of the EPR signal with the CuTPP samples of known spin concentration was carried out, and the data is shown in Table 4.7. It is also compared with the reducible oxygen calculated from the fitted result of TPR (Figure 4.13).

Table 4.7 The comparable oxygen analysis from ceria samples by TPR and EPR (NM: not measurable).

Size (nm)	**Oxygen calculated from TPR (mmol/g)**				**$[O_2^-]$ from EPR (mmol/g)**
	$[O]_{A1'}$ 675K	**$[O]_{A1}$ 750K**	**$[O]_{bulk}$**	**$[O]_{total}$**	
5.3	0.50		0.23	0.75	NM
5.1	0.12	0.47	0.23	0.87	0.11
4.9	0.32	0.46	0.19	1.06	0.33
4.4	0.47	0.51	0.17	1.22	0.35

In Table 4.7 the sharp increase in the total oxygen content from TPR (the A_1'

surface [O] peak) as the particle size fell below 5.3 nm matches the O_2^- value derived from EPR within experimental error. Thus, it is clear that the additional surface oxygen is the chemisorbed O_2^-. It is proposed that a paramagnetic species with high O_2^- character is formed from the gaseous molecular oxygen adsorption on a reduced low dimensional ceria surface [25]. Note that surface O_2^- has previously been identified on a low dimensional n-type semiconducting oxide sensor (SnO_2 and CeO_2) through electron localization by the adsorbed molecular oxygen [35, 50, 51].

4.5 Conclusion

In summary, in this chapter we find no evidence for the increasing surface Ce^{3+} and oxygen vacancies from Ce^{4+} the observed lattice expansion of nano ceria with decreasing size. Similarly, from detailed TEM work, Hailstone *et al.* [52] challenged the earlier claim of a reduced ceria shell (C-Ce_2O_3) on 1.5 nm ceria as they showed a resilient oxygen storage value as well as a fluorite structure of this ceria size. The lattice expansion should be attributed primarily to the strain of increasing surface energy at a smaller size. The formation of the surface superoxide species through the molecular oxygen adsorption on nano ceria of 5.3 nm or below is also demonstrated for the first time. This species is undoubtedly important in selective oxidation catalysis [1,53]. One possible potential application is to use the nano ceria for reversible desulphurization [54]. Thus, the quantum size dependent oxygen storage capacity is clearly shown. The mechanism for the superoxide formation is not known but could be related to a dioxygen interaction with a surface oxygen vacancy or vacancy clusters on a stressed surface [25] where quantum confinement plays a key role. Further work in this area is required. At this point, the previously observed blue shift in optical spectroscopy of ceria particles with a similar size range is noted [7].

Our results suggest that the earlier discovery by Tsunekawa and co-workers [27, 28] of lattice expansion of ceria at smaller size is mainly due to the 'strain effect' of higher surface energy with no evidence on increasing Ce^{3+} concentration. At ceria sizes of below 5 nm it is observed *for the first time* that the total amount of reducible oxygen is dramatically increased due to the formation of superoxide species (O_2^-) on a ceria surface, a result clearly indicative of its size dependent oxygen buffering capacity. The formation of superoxide species on a reduced ceria surface is attributed

to the activation of molecular oxygen from air by the Ce^{3+} to form Ce^{4+}-O_2^- at low dimension. We believe that the present findings have important implications in catalysis.

4.6 Reference

1. A. Trovarelli, Catalysis by ceria and related materials; Imperial College Press: London, 2002.
2. J. Kaspar, P. Fornasiero, M. Graziani, Catalysis Today, 50 (1999) 285-298.
3. S. D. Park, J. M. Vohs, R. J. Gorte, Nature, 404 (2000) 265-267.
4. G. A. Deluga, J. R. Salge, L. D. Schmidt, X. E. Verykios, Science, 303 (2004) 993-997.
5. N. Acerbi, S. C. Tsang, S. Golunski, P. Collier, Chemical Communications, 13 (2008) 1578-1580.
6. T. Masui, K. Fujiwara, K. Machida, G. Adachi, T. Sakata, H. Mori, Chemistry of Materials, 9 (1997) 2197-2204.
7. M. D. Hernández-Alonso, A. B. Hungría, A. Martínez-Arias, J. M. Coronado, J. C. Conesa, J. Soria, M. Fernández-García, Physical Chemistry Chemical Physics, 6 (2004) 3524-3529.
8. M. A. Thundathil, W. Lai, L. Noailles, B. S. Dunn and S. M. Haile, Journal of the American Ceramic Society, 87 (2004) 1442.
9. D. Knapp, T. Ziegler, Journal of Physical Chemistry C, 112 (2008) 17311-17318.
10. S. Tsunekawa, S. Ito, and Y. Kawazoe, Applied Physics Letters, 85 (2004) 3845.
11. J. M. Thomas and W. J. Thomas, Principles and Practice of Heteregeneous Catalysis, VCH, Weinheim, 1997.
12. JCPDS #43-1002
13. X. D. Zhou, W. Huebner, Applied Physics Letters, 79 (2001) 3512-3514.
14. J. R. McBride, K. C. Hass, B. D. Poindexter, W. H. Weber, Journal of Applied Physic, 76 (1994) 2435-2441.

15. I. Kosacki, T. Suzuki, H. U. Anderson, P. Colomban, Solid State Ionics, 149 (2002) 99-105.
16. J. E. Spanier, R. D. Robinson, F. Zhang, S. W. Chan, and I. P. Herman, Physical Review B, 64 (2001) 245404.
17. W. H. Weber, K. C. Hass, J. R. McBride, Physical Review B, 48 (1993) 178.
18. H. Richter, Z. P. Wang, L. Ley, Solid State Communications, 39 (1981) 625-629.
19. A. Nakajima, A. Yoshihara, M. Ishgame, Physical Review B, 50 (1994) 13297.
20. K. Clausen, W. Hayes, J. E. Macdonald, R. Osborn, P. G. Schnabel, M. T. Hutchings, A. Magerl, Journal of the Chemical Society-Faraday Transactions, 83 (1987) 1109-1112.
21. M. Balkanski, R. F. Wallis, E. Haro, Physical Review B, 28 (1983) 1928.
22. F. Zhang, S. W. Chan, J. E. Spanier, E. Apak, Q. Jin, R. D. Robinson, I. P. Herman, Applied Physics Letters, 80 (2002), 127.
23. Z. W. Wang, S. Seal, S. Patil, C. S. Zha, Q. Xue, Journal of Physical Chemistry C, 111 (2007) 11756-11759.
24. S. Deshpande, S. Patil, S. V. Kuchibhatla, S. Seal, Applied Physics Letters, 87 (2005) 133113.
25. F. Esch, S. Fabris, L. Zhou, T. Montini, C. Africh, P. Fornasiero, G. Comelli, R. Rosei, Science, 309 (2005) 752-755.
26. R. D. Shannon, C. T. Prewitt, Acta Cryst. B, 25 (1969) 925-1048.
27. S. Tsunekawa, R. Sivamohan, S. Ito, A. Kasuya, T. Fukuda, Nanostructured Materials, 11 (1999) 141-147.
28. S. Tsunekawa, K. Ishikawa, Z. Q. Li, Y. Kawazoe, A. Kasuya, Physical Review Letters, 85 (2000) 3440-3443.
29. S. Tsunekawa, S. Ito, Y. Kawazoe, Applied Physics Letters, 85 (2004) 3845-3847.

30. F. Zhang, S. W. Chan, J. E. Spanier, E. Apak, Q. Jin, R. D. Robinson, I. P. Herman, Applied Physics Letters, 80 (2002) 127-129.
31. S. Tsunekawa, K. Ishikawa, Z.Q. Li, Y. Kawazoe, Y. Kasuya, Physical Review Letters, 85 (2000) 3440.
32. P. Burroughs, A. Hamnett, A. F. Orchard, G. Thornton, Journal of the Chemical Society Dalton Transactions, 17 (1976) 1686-1698.
33. A. Laachir, V. Perrichon, A. Badri, J. Lamotte, E. Catherine, J. C. Lavalley, J. Elfallah, L. Hilaire, F. Lenormand, E. Quemere, G. N. Sauvion, O. Touret, Journal of the Chemical Society-Faraday Transactions, 87 (1991) 1601-1609.
34. S. Seal, T. Barr, Experimental Methods in the Physical Sciences (H. Singh Nalwa edts.), Academic, New York, Chapter 2, 111-190, 2001.
35. V. V. Pushkarev, V. I. Kovalchuk, J. L. d'Itri, The Journal of Physical Chemistry B, 108 (2004) 5341-5348.
36. A. E. Hughes, R. J. Taylor, B. R. W. Hinton, L. Wilson, Surface and Interface Analysis, 25 (1997) 223-234.
37. B. E. Koel, G. Praline, H. I. Lee, J. M. White, Journal of Electron Spectroscopy and Related Phenomena, 21 (1980) 31-46.
38. E. Abi-aad, R. Bechara, J. Grimblot, A. Aboukais, Chemistry of Materials, 5 (1993) 793-797.
39. A. E. Hughes, J. D. Gorman, P. J. K. Patterson, R. Carter, Surface and Interface Analysis, 24 (1996) 634-640.
40. J. P. Holgado, G. Munuera, J. P. Espinos, A. R. Gonzalez-Elipe, Applied Surface Science, 158 (2000) 164-171.
41. P. Dolle, S. Drissi, M. Besancon, J. Joupille, Surface Science, 269/270 (1992) 687-690.

42. H. C. Yao, Y. F. Y. Yao, Journal of Catalysis, 86 (1984) 254-265.
43. V. Perrichon, A. Laachir, G. Bergeret, R. Frety, L. Tournayan, O. Touret, Journal of the Chemical Society-Faraday Transactions, 90 (1994) 773-781.
44. J. E. Rowe, Solid State Communications, 15 (1974) 1505-1507.
45. A. Martínez-Arias, J. C. Conesa, J. Soria, Res. Chem. Intermed., 33 (2007) 775-791.
46. C. Oliva, G. Termignone, F. P. Vatti, L. Forni, A. V. Vishniakov, Journal of Materials Science, 31 (1996) 6333-6338.
47. X. L. Zhang, K. J. Klabunde, Inorganic Chemistry, 31 (1992) 1706-1709.
48. J. Soria, A. Martinez-Arias, J. C. Conesa, Journal of the Chemical Society-Faraday Transactions, 91 (1995) 1669-1678.
49. J. J. Steenhuis, B. A. Barry, Journal of Physical Chemistry B, 101 (1997) 6652-6660.
50. A. Gurlo, Chem. Phys. Chem., 7 (2006) 2041-2052.
51. S. C. Tsang, C. D. A. Bulpitt, P. C. H. Mitchell, A. R. Ramirez-Cuesta, Journal of Physical Chemistry B, 105 (2001) 5737-5742.
52. R. K. Hailstone, A. G. DiFrancesco, J. G. Leong, T. D. Allston, K. J. Reed, Journal of Physical Chemistry C, 113 (2009) 15155–15159.
53. M. Y. Yeung, K. M. K. Yu, Q. J. Fu, D. Thompsett, M. I. Petch, S. C. Tsang, Journal of the American Chemical Society, 127 (2005) 18010-18011.
54. R. S. Kempegowda, N. Laosiripojana, S. Assabumrungrat, Korean Journal of Chemical Engineering, 25 (2008) 223-230.

CHAPTER 5

THE ENHANCEMENT FOR THE OXYGEN STORAGE CAPACITY OF CERIA BY METAL

5.1 Introduction 168

5.2 Selective Glycerol Hydrogenolysis 170

5.2.1 Introduction 170

5.2.2 Glycerol Hydrogenolysis on Raney Ni 172

5.2.3 Mechanism of Selective Glycerol Hydrogenolysis 176

5.2.4 Ceria Promotion on Selective Glycerol Hydrogenolysis Reaction 177

5.3 The Promoted Oxygen Storage Capacity of Pt/Ceria by Strong Metal Ceria Interaction 180

5.3.1 The Synthesis of Pt/Ceria with Different Metal Oxide Interactions 180

5.3.2 Enhancement of Oxygen Storage Capacity of Ceria by Pt 183

5.3.3 The Effect of Metal Concentration 193

5.4 Conclusion 199

5.5 Reference 200

5.1 Introduction

Ceria is a very interesting oxide with widely industrial applications because of its high oxygen storage capacity [1]. In recent years, an increasing number of researchers have recognized that the oxygen vacancies of ceria particles were playing a key role in the high oxygen storage capacity of ceria, and were thus promoting redox catalytic reactions [1-3]. For example, Liu et al. reported a direct correlation between the concentrations of larger sized oxygen vacancy clusters and the reactivity of ceria in CO oxidation reaction [2]. As was stated in my last chapter, when the particle size of pure ceria is decreased below 5 nm the total amount of reducible oxygen is dramatically increased due to the formation of superoxide type species O_2^- from the molecular oxygen adsorption on the highly strained surface, where the oxygen vacancies may exist in the form of clusters [3].

Ceria supported metals have been especially useful as automotive, emissions control catalysts for many years [1, 4, 5]. The contribution of ceria as a support material for metals in hydrocarbon reforming [6, 7], water gas shift [8-13], and hydrocarbon oxidation reactions [14] etc. have been reported. For all these applications, ceria is used as the support for metals [8, 11], and metals are also regarded as the promoters for ceria [12, 15]. The interaction occurs at the metal-ceria interface, giving unique catalytic properties that were suggested as an unambiguous observation [16]: a direct influence of the oxide on the chemisorption and catalytic properties of the metal phase either by stabilizing unusual metal particle structure, by changing the electronic properties due to electron transfer processes between the metal particles and the oxide, or chemical bonding – compound formation – between metal and oxide. As a result, many phenomena could explain metal-oxide interactions

well. However, in this chapter we are focusing especially on the relationship between the metal-oxide interactions and the oxygen vacancies over ceria. Recently, Farmer et al. [17] published a paper in *Science* reporting that metal particles bind locally to those defective regions of a ceria surface where there is a greater oxygen vacancy concentration than elsewhere. The question is: if there is a strong local metal-oxide interaction between metal and oxide, does it create the oxygen vacancies around the metal? If this is the case, will it cause higher oxygen storage capacity of the metal promoted ceria? So with a better understanding of the interaction between metal and ceria will give better guidance for the future catalysts preparation.

In this chapter the glycerol hydrogenation reaction is employed as a chemical probe, which reflects the differences between the levels of surface oxygen vacancies in a commercial Ni catalyst and a ceria supported Ni catalyst. This is also an important reaction which has currently been receiving much attention. Particular attention will be paid to the specific preparative aspects of metal/ceria interphase, which may give some important chemical and nano-structural effects for the form of efficient oxygen vacancies by doping metal on ceria. Thus, synthetic techniques such as wet grinding, microemulsion, and co-microemulsion were used to dope Pt in ceria for the creation of active oxygen species. TPR, XRD, EPR, TEM, FTIR and Raman techniques were used as the characterization methods.

5.2 Selective Glycerol Hydrogenolysis

5.2.1 Introduction

Around 1 million tones of glycerol are produced per year in the current market, although with a declining market value coupled with the high expense of purifying the crude glycerol, much of the glycerol produced in biodiesel plants is disposed of as waste. An increase in the applications of glycerol would make separation profitable and could make biodiesel production itself more economical. From a green chemistry point of view glycerol is an interesting chemical because it is highly functionalized compared to fossil derived hydrocarbons, which gives it strong potential as a bio-renewable platform chemical. Indeed the US Department of Energy recently highlighted glycerol as one of its top 12 biomass derived sugar based building block compounds [18]. Possible pathways for transformation of glycerol include oxidation, dehydration, etherification, and polymerization [19].

The hydrogenolysis of glycerol using heterogeneous catalysis is one method for the reuse of glycerol. The products from the hydrogenolysis of glycerol have large possibilities [20], but essentially they proceed by two pathways: a C-C cleavage pathway and a C-O cleavage pathway. Controlling the selectivity of hydrogenolysis is a challenging prospect due to the highly similar bond energy of C-C (~154 KJ/mol) and C-O (~143 KJ/mol) bonds in glycerol, so there are many advantages to looking for available catalysts for selectively producing the specific chemical from glycerol. For example, it will increase the atom economy of biodiesel production by forming a cycle of bi-product and feedstock, reduce the financial cost of production, and increase the potential for the biofuel to become carbon negative [20-22]. Some

potential products from either C-C cleavage pathway or C-O cleavage pathway are shown in Scheme 5.1.

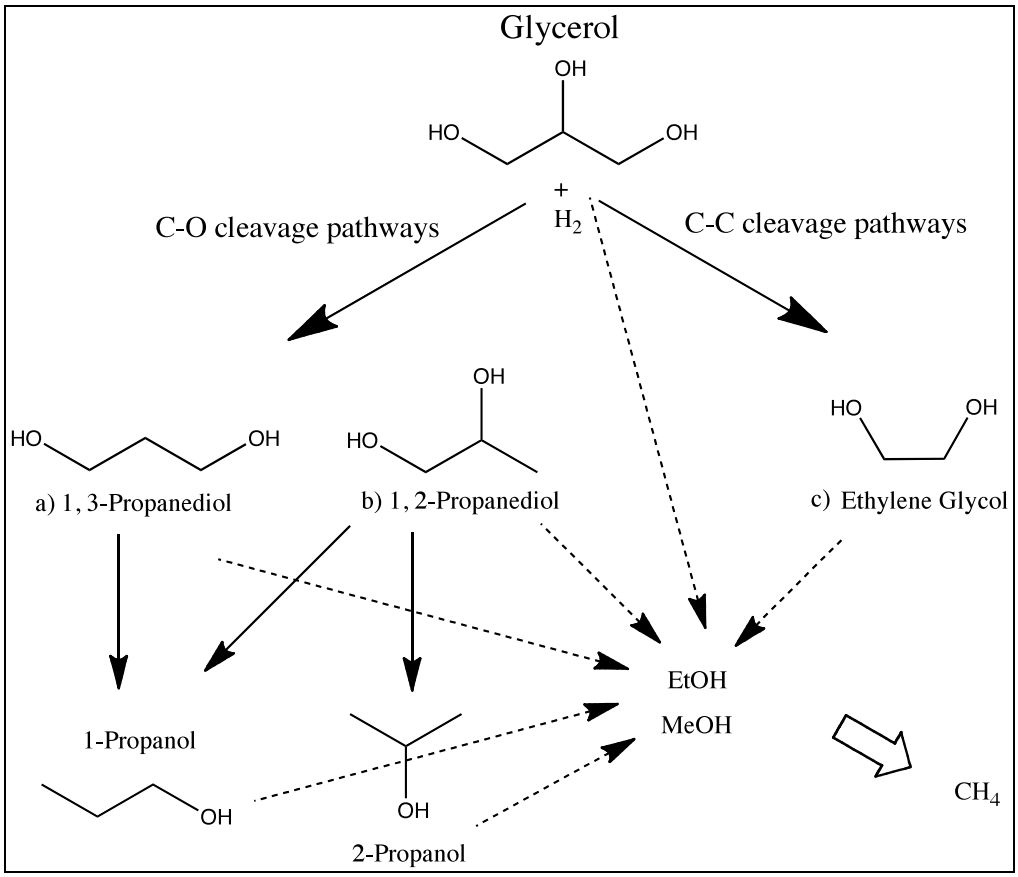

Scheme 5.1 Possible products from hydrogenolysis of glycerol.

From the C-O cleavage pathway, the major products of the first stage of glycerol hydrogenolysis are 1, 2-propanediol and 1, 3-propanediol (although it was difficult to separate them using the HPLC equipment in our lab). Propanediol (PD) will be further degraded to 1-propanol or 2-propanol in the second stage. In the C-C cleavage pathway, the major first step product will be ethylene glycol (EG) without any typical second step product. Some other products such as methanol, ethanol may come from the glycerol itself in the glycerol hydrogenolysis reaction, and the first step and second step products from C-O cleavage and C-C cleavage pathways. Methane is the

final product of the whole reaction. Many heterogeneous catalysts have been demonstrated to be effective in the glycerol hydrogenolysis of lower molecular weight chemicals [19-23] such as Cu, Pd, Rh, Co, Ir, Ni, and Pt, with the supports of silica, alumina and carbon. In this part of work, Raney Ni is chosen as a catalyst for the glycerol hydrogenolysis reaction before the later investigation of Ni/ceria sample.

5.2.2 Glycerol Hydrogenolysis on Raney Ni

Figure 5.1 shows the product selectivities over two reaction temperatures in the glycerol hydrogenolysis reaction.

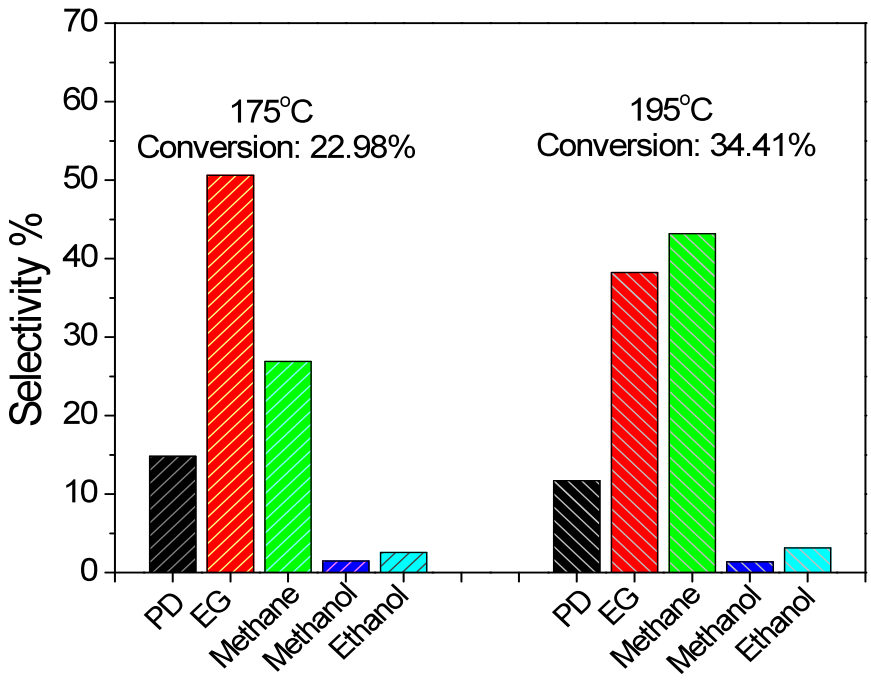

Figure 5.1 Hydrogenolysis of Glycerol with Raney Ni at two different temperatures. * $p(H_2)$ = 20 bar, 50 mL 0.6363 M Glycerol in water (32 mmol), 3 mL Raney Ni, reaction time 2 h.

As shown in Figure 5.1, when glycerol and Raney Ni are stirred and heated together at 175 °C for 2 h with 20 bars hydrogen, the conversion of glycerol is 22.98%. The major products are ethylene glycol (EG), propanediol (PD), and methane, with traces of methanol, ethanol, and other chemicals (not list in the figure). The selectivity of EG is 50.6%, the selectivity of PD is 14.8%, and the selectivity of methane is 26.9%.

When the reaction temperature increases to 195 °C, the conversion of glycerol is 34.41%. The major products are still EG, PD, and methane with minor production of other low carbon chain products. The selectivity of EG is 38.22%, PD 11.69 %, with 43.18% methane. Compared with PD, EG formed from C-C cleavage pathway appears to be more dominant in both temperatures.

Figure 5.2 shows the hydrogenolysis of glycerol on Raney Ni at 195 °C with the different reaction time.

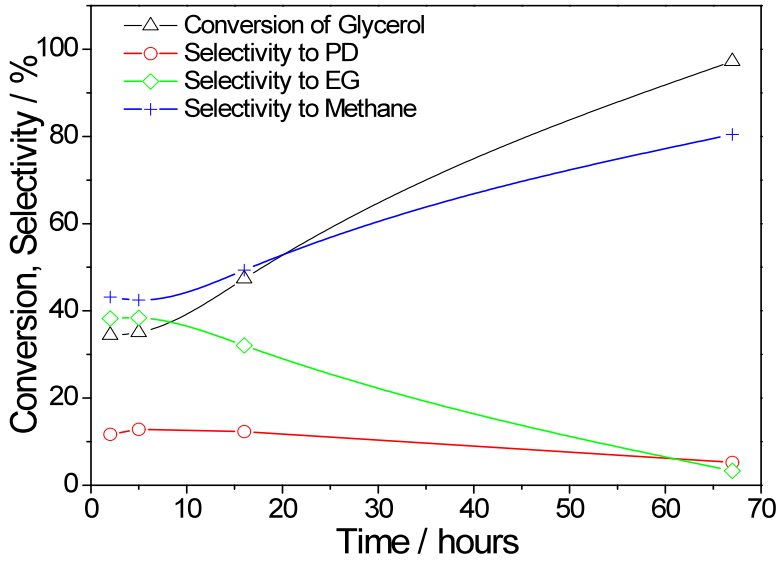

Figure 5.2 Hydrogenolysis of Glycerol with Raney Ni with different reaction time.

* $p(H_2)$ = 20 bar, reaction temperature is 195 °C, 50 mL 0.6363 M Glycerol in water (32 mmol), 3 mL Raney Ni.

In Figure 5.2, when the reaction time increases from 2 h to 5 h, the conversion of glycerol is kept at about 34% - 35%. EG and methane are the major products with selectivity of around 40% and 12%, respectively. When the reaction time is increased to 16 h, the glycerol conversion is increased to 47.36%. The selectivity of methane increases by 6% to 49.36%, whilst the selectivity of EG decreases by the same extent to 32.07%, and PD selectivity remains the same. With longer reaction time of 67 hours, the conversion of glycerol increases to 97.24%, with methane as the major product with the selectivity of 80.46%. The selectivity of EG is only 3.31%, and PD decreases to 5.23%. It is apparent that most of the methane molecules are derived from the degradation of EG.

The effect of the hydrogen pressure for the reaction is also tested, and the results are shown in Figure 5.3.

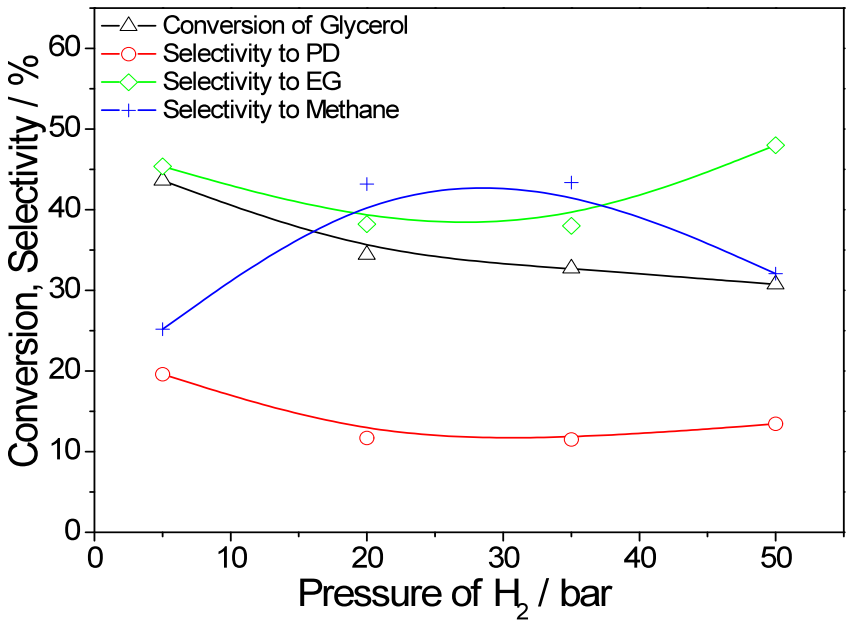

Figure 5.3 Hydrogenolysis of Glycerol with Raney Ni in different hydrogen pressure. * Reaction temperature 195 ^{o}C, 50 mL 0.6363 M Glycerol in water (32 mmol), 3 mL Raney Ni, reaction time 2 hours.

As shown in Figure 5.3, the conversion of glycerol decreases when the hydrogen pressure increases. It is 43.60% at 5 bars H_2, 34.41% at 20 bars H_2, 32.72% at 35 bars, and 30.74% at 50 bars H_2.

When the pressure of the reactor is at 5 bars, the selectivity of EG is 45.36%, PD 19.6%, and methane 25.17%. When the hydrogen pressure increases to 20 bars the selectivity of EG decreases to 38.22% and PD decreases to 11.69%, but the methane selectivity increases to 43.18%. When the hydrogen pressure increases to 35 bars, all the products' selectivity is similar compared with the hydrogen atmosphere at 20 bars.

Interestingly, when the hydrogen pressure increases to 50 bars, the selectivity of EG increases by 10% to 47.98%, while the methane selectivity dropped by about 11% to 32.06%. The PD selectivity does not change too much.

From the testing of the glycerol hydrogenolysis on Raney Ni, it can be seen that Ni is the selective catalyst for the C-C cleavage, which happens in the first few hours (less than 5 hours), the major products being EG, methane, and PD.

Regarding production of EG from glycerol hydrogenolysis, lower temperature (175 ^{o}C), shorter time (2h), and higher pressure (50 bar) appear to be better experimental conditions.

5.2.3 Mechanism of Selective Glycerol Hydrogenolysis

Product analysis may provide hints about the mechanism of glycerol hydrogenolysis reaction. Several mechanisms have been suggested, but the most acceptable one is from Montassier et al. [20-23]. In this mechanism, the first step of glycerol hydrogenolysis is involving dehydrogenation of glycerol to glyceraldehyde on metal surface. The cleavage of C-C bonds is then proposed to occur through a retro-aldol reaction, whereas the C-O cleavage occurs through a dehydration reaction. Based on the work from Montassier and other groups, Maris et al. [24] introduced an effective C-C cleavage Ru catalyst, such that the glyceraldehyde produced can be converted and hydrogenated to EG and methanol. It is clear from the work above that Ni is also an effective C-C cleavage catalyst. The proposed pathway of glycerol hydrogenolysis over Raney Ni is shown in Scheme 5.2 [20-22, 24].

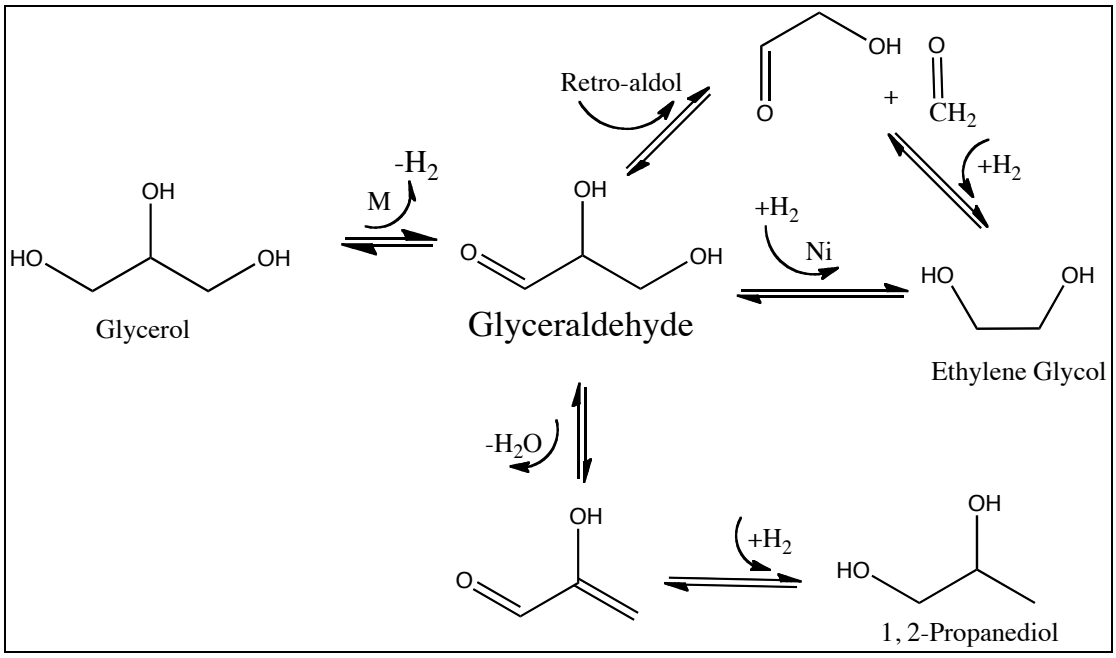

Scheme 5.2 Possible pathways of glycerol hydrogenolysis on Raney Ni [20-22, 24].

5.2.4 Ceria Promotion on Selective Glycerol Hydrogenolysis Reaction

As discussed in Chapter 3, we have studied two Ni containing samples, namely NSA and NSAC. NSA is a commercial catalyst with 65 wt.% Ni on a silica and alumina support, and NSAC is the ceria modified NSA sample prepared by the sol-gel method. The NSAC sample showed a strong interaction between ceria and the Ni nanoparticles with the ceria partly covered with Ni.

In this work, the glycerol hydrogenolysis reactions were tested over the NSA, NSAC and Raney Ni samples. Table 5.1 summaries the results of the three samples.

Table 5.1 Hydrogenolysis of Glycerol over NSA, NSAC and Raney Ni catalysts

Sample	**Conv. /%**	**Selectivity / %**				
		PD	EG	Methane	2-propanaol	Ethanol
Raney Ni	24.65	16.51	55.98	22.45	0.15	1.68
NSA	17.29	11.13	22.01	19.67	16.13	30.06
NSAC	5.05	73.62	13.01	2.36	4.88	5.64

* $p(H_2)$ = 50 bar, 20 mL 0.6363 M Glycerol in water (12.7 mmol), 2mL Raney Ni, 200 mg NSA and NSAC solid powder, reaction temperature at 175 ^{o}C, reaction time 2 hours.

On the Raney Ni catalyst, EG, PD and methane are three main products and the EG is the major product with the highest selectivity due to the good activity in C-C bond cleavage. In the NSA sample, there are at least five products with other trace products from the glycerol hydrogenolysis reaction: 22.01% EG, 11.13% PD, 19.67% methane, 16.13% 2-propanaol, and 30.06% ethanol. The presence of silica alumina support in the case of NSA is expected to play a key role in giving a range of products (cracking) with different product distribution due to the introduction of surface acid sites to glycerol hydrogenolysis reaction [25, 26]. NSAC is a ceria modified NSA sample with evidence of a strong interaction between Ni and ceria. As seen from Table 5.1, the conversion of the glycerol hydrogenolysis reaction on NSAC is significantly lower than the other two samples (5.05%), and the major products are mostly only PD and EG. The surface acidity introduced by silica-alumina support for extensive product cracking does not seem to work here, presumably because of the extensive coverage of the catalyst with doped ceria coating. The activity of this Ni catalyst for the glycerol hydrogenolysis reaction is also weaker because some active sites of Ni are partly covered by ceria. It is interesting to note that the allergic C-C bond cleavage Ni catalyst (for EG formation) can give high selectivity to PD (73.62%) in the presence of ceria coating (favourable for C-O cleavage). Scheme 5.3 summaries our postulation on the influence of ceria to Ni in promoting PD formation in the glycerol hydrogenolysis reaction.

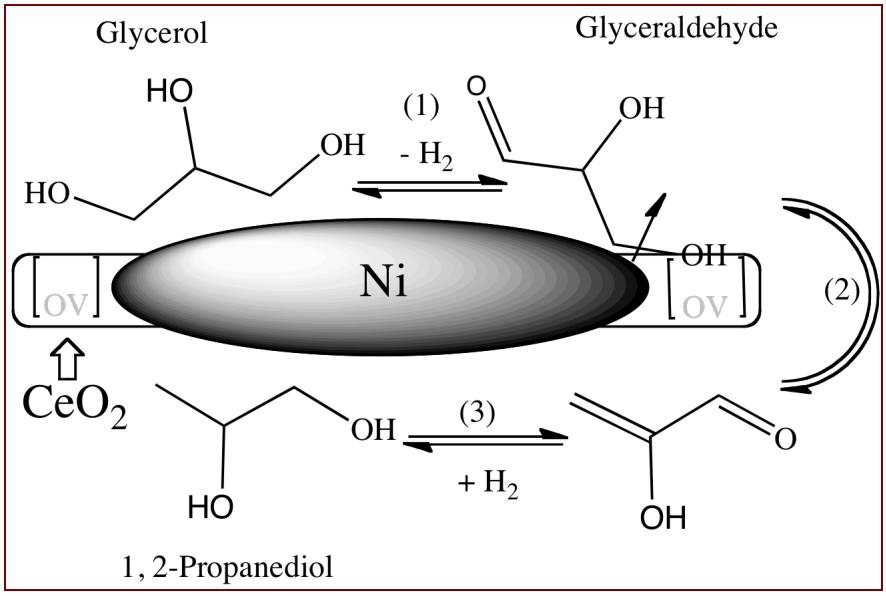

Scheme 5.3 Possible pathways of glycerol hydrogenolysis on NSAC.

As shown in Scheme 5.3, when the glycerol is dehydrogenated to glyceraldehyde (the first step), we envisage that the OH group of this intermediate is then adsorbed by the oxygen vacancy on the surface of ceria around the Ni at the interface, thus dehydration of the molecule will assist the cleavage of the C-OH bond (the second step) to give 1,2-propanediol as the major product upon surface hydrogenation. As a result, the oxygen vacancies in the interface of Ni and ceria can clearly promote the C-O cleavage in glycerol hydrogenolysis reaction, giving a sharp increase in the PD selectivity.

It is therefore concluded that when ceria is doped on the metal, a strong metal-oxide interaction is created. It appears that oxygen vacancies are formed in the interface of the metal and ceria, which can involve surface reactions. In this case, PD can be produced as the major product from glycerol hydrogenolysis.

5.3 The Promoted Oxygen Storage Capacity of Pt/Ceria by Strong Metal Ceria Interaction

5.3.1 The Synthesis of Pt/Ceria with Different Metal Oxide Interactions

Pt was the chosen metal to modify the ceria to investigate its metal oxide interactions. To avoid the interference of the exposed metal on the surface of ceria, the core-shell Pt/ceria samples were prepared by the microemulsion method [12, 13, 27].

First, we synthesized two core-shell samples, namely MPC02 and MPC06. Both samples contained 1.25 at.-% Pt in ceria. The MPC02 was synthesized by the microemulsion method followed by pre-reduction of metal [27]. The MPC06 was the Pt modified nano ceria prepared by the co-microemulsion method [12, 13], where the Pt precursor was added to the micelle before the application of ceria. As a comparison with these two core shell Pt/ceria samples, PC03 sample was synthesized, which contained Pt^0 metal particles prereduced from Pt^{4+} ions prepared by the wet-grinding method on a JMCE sample. (A commercial pure ceria nanoparticles was supplied by Johnson Matthey which was christened as JMCE with the particle size of 15-30 nm and the BET surface area of 50-60 m^2/g). All the synthesis details are described in Chapter 2. Figure 5.4 shows the XRD patterns of all the samples.

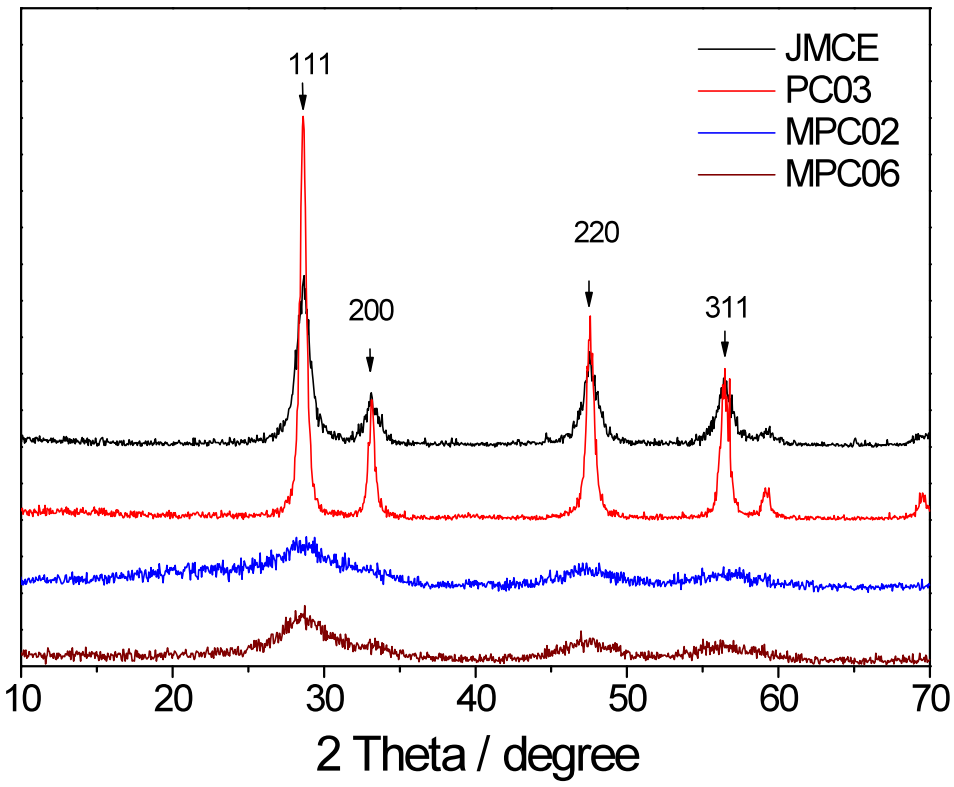

Figure 5.4 XRD patterns of commercial ceria and Pt doped ceria by different methods.

In Figure 5.4, the diffraction peaks of CeO_2 appear in all the samples, contributing to the 2θ degree 28.6 (111), 33.1 (200), 47.5 (220) and 56.3 (311). When the commercial sample is doped by Pt and calcined at 500 ^oC for 2 h, the peaks of PC03 are much more intensive than the original commercial JMCE sample because of the aggregation to ceria particles during the calcination treatment. Very broad peak corresponding to CeO_2 from MPC02 and MPC06 are observed. This shows without calcination, ceria nanoparticles have already formed after stirring and drying in air *via* the microemulsion method. No Pt peak is detected in the XRD pattern of any sample, so one may conclude that Pt disperses well and the average Pt size is likely to be lower than 2nm. HRTEM was employed for the further investigation and a typical image from MPC06 is shown in Figure 5.5.

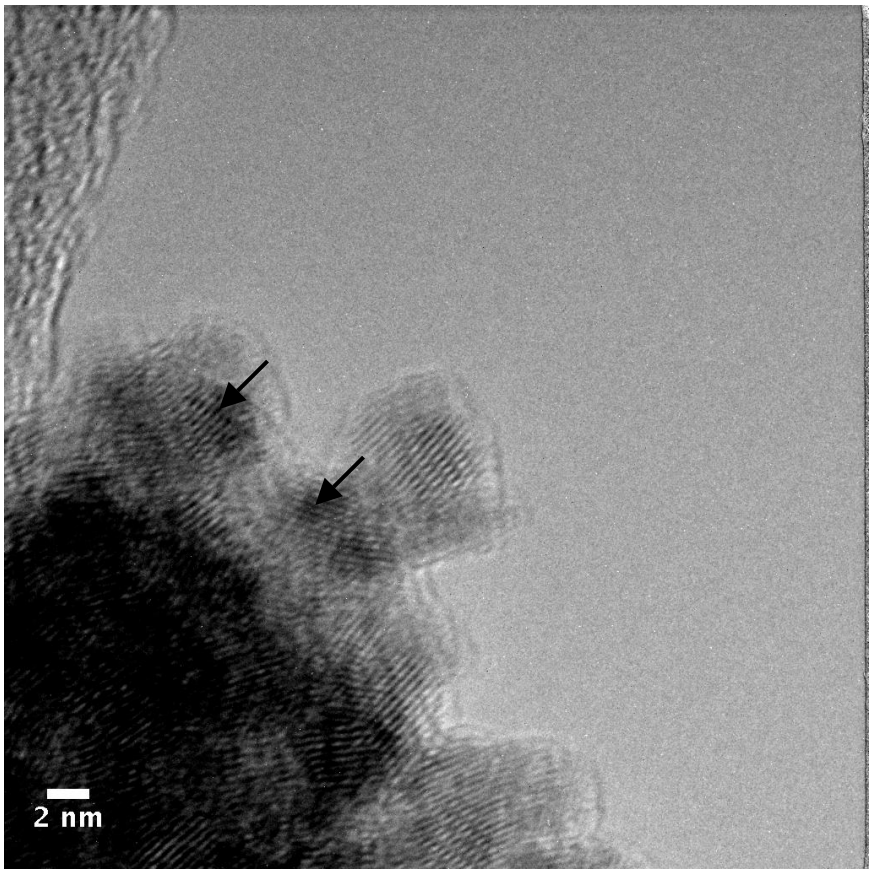

Figure 5.5 HRTEM image of MPC06 sample (co-microemulsion method modified Pt@ceria sample).

In Figure 5.5, MPC06 sample shows the characteristic electron micrograph of cerium oxide and highly crystalline ceria particles are clear observed. Also, under a careful examination of the TEM micrograph, the Pt core is clearly evident inside the ceria particle, as indicated by arrows. It can be concluded that the core shell Pt/ceria sample is successfully achieved.

5.3.2 Enhancement of Oxygen Storage Capacity of Ceria by Pt

Temperature programmed reduction (TPR) is a simple thermal technique widely used to investigate the ceria based materials and can provide wealth of information about the redox properties of oxide materials, valence states of metal ions at various stages of reduction and the nature of metal-support interactions [1, 28]. The method can also be applied to estimate the oxygen storage capacity of ceria. Figure 5.6 shows the TPR profiles of all these samples from ambient temperature to 1000 ^{o}C at 10 ^{o}C/min.

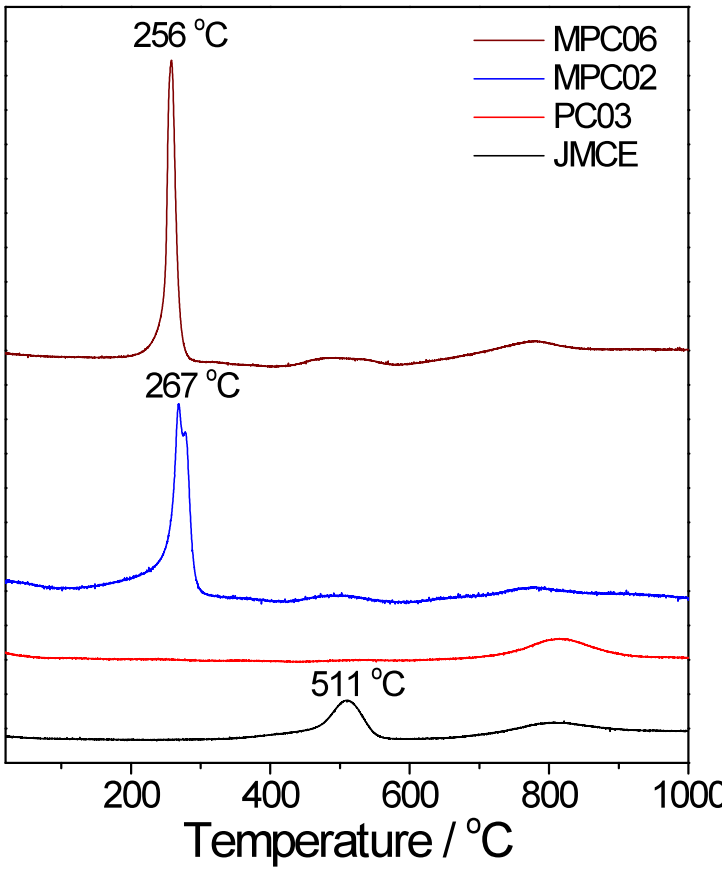

Figure 5.6 H_2-Temperature Programmed Reduction (TPR) profiles of pure ceria and Pt doped ceria by different methods.

In Figure 5.6, JMCE sample (nano ceria bought from Johnson Matthey and namely JMCE, the bottom line) shows the typical ceria TPR profile with two peaks, the surface oxygen reduction peak is at 511 ^{o}C and the bulk oxygen reduction peak is at 810 ^{o}C. For PC03, when the profile is compared with the reduction processes of JMCE sample, it is noted that the surface oxygen almost disappears the bulk oxygen peak becomes larger, which is similar to the TPR profile of bulk ceria with very low surface area i.e. 1.5 m^2/g [28]. It is believed that after the calcination treatment of the PC03 sample in the air, the ceria nanoparticles are aggregated to form bulk ceria. The absence of reducible surface oxygen suggests that there is poor interaction between the ceria and the physical mixed Pt particle.

For MPC02 and MPC06 synthesized by the microemulsion method, there is no significant difference for the bulk oxygen between the two samples and the pure ceria. Also, there is no reduction peak before 100 ^{o}C. Such low temperature reduction peak has previously been assigned to the spillover reduction peak by the exposed Pt metal [12]. It means for both the MPC02 and MPC06 samples, the Pt metal is fully encapsulated by the ceria shell. There are two surface oxygen peaks observed in the MPC02 and MPC06. The peak at about 500 ^{o}C is the ceria surface oxygen. Another reduction peak shifted to lower temperature is the surface oxygen of ceria but promoted by the Pt metal [1, 12, 28, 29]. Note for the MPC06, the shifted surface oxygen peak is at 256 ^{o}C. For the MPC02, the shifted surface oxygen peak is at 267 ^{o}C. Thus, it is believed that the MPC06 can offer a stronger Pt metal-ceria interaction than the MPC02 [27]. As the result, it can be clearly seen that with the stronger metal oxide interaction, the promotion of the surface oxygen reduction is more efficient.

The quantitative consumptions of hydrogen over all samples are summarised in Table 5.2 after the integration of the corresponding peaks by Gaussian method.

Table 5.2 Relative consumption of surface and bulk oxygen in ceria and Pt doped ceria particles from H_2-TPR (Figure 5.6)

	$[O]_{tot.}$ (mmol/g)	Surf oxygen from Pt/ceria interface			Surf oxygen of Ceria			Bulk oxygen		
		T1 (^oC)	[O] (mmol/g)	%	T2 (^oC)	[O] (mmol/g)	%	T3 (^oC)	[O] (mmol/g)	%
JMCE	0.681	-	-	-	511	0.394	57.90	810	0.287	42.10
PC03	0.386	-	-	-	525	0.011	2.78	819	0.375	97.21
MPC02	1.303	267	0.951	72.98	499	0.087	6.68	777	0.265	20.33
MPC06	1.139	256	0.775	68.06	492	0.11	10.09	776	0.249	21.84

In Table 5.2, the total reducible oxygen content from JMCE sample is 0.681 mmol/g, similar to the oxygen amount calculated from the nano ceria synthesized by microemulsion method (around 0.7 mmol/g, reported in Chapter 4). The total reducible oxygen content of PC03 sample is much less than JMCE, the surface oxygen is almost not detectable but the bulk oxygen increases dramatically (0.375 mmol/g comparable to 0.287 mmol/g). It is attributed to bulk ceria obtained from the aggregation during the calcination process.

It is noted that the total reducible oxygen values in the MPC02 and MPC06 are substantially higher than those of pure ceria JMCE (MPC02 gives 1.303 mmol/g and MPC06 gives 1.139 mmol/g as compared to the JMCE of 0.681 mmol/g). In the MPC02, the metal promoted surface oxygen peak at 267 ^oC is estimated to be 0.951 mmol/g. The peak at 495 ^oC from the normal ceria surface oxygen is only 0.087 mmol/g (20% lower than the JMCE surface oxygen peak). But the bulk oxygen peak of the MPC02 sample at 779 ^oC is of 0.265 mmol/g. For MPC06, the new peak at 256

^{o}C is estimated to be 0.775 mmol/g, the surface oxygen peak at 500 ^{o}C is 0.11 mmol/g and the bulk oxygen at 783 ^{o}C is 0.249 mmol/g.

Compared to the pure ceria JMCE, there is more reducible surface oxygen content, mostly in form of the metal promoted surface oxygen. It clearly means there is better oxygen storage capacity in MPC02 and MPC06 samples. It is able to conclude that using microemulsion methods to place Pt in ceria, the oxygen storage capacity of ceria is enhanced due to more efficient metal-ceria interactions. But by the wet-grinding method there is no improvement of the oxygen storage capacity due to the poor interaction between the metal and ceria. Also, the MPC02 and MPC06 samples showing the stronger metal-ceria interaction give active surface oxygen which can be reduced at much lower temperatures. So, it is concluded that with the stronger metal-ceria interaction(s), the reducibility of the surface oxygen of ceria is more enhanced.

The Raman spectroscopy technique is used to provide more information and the spectra are shown in Figure 5.7.

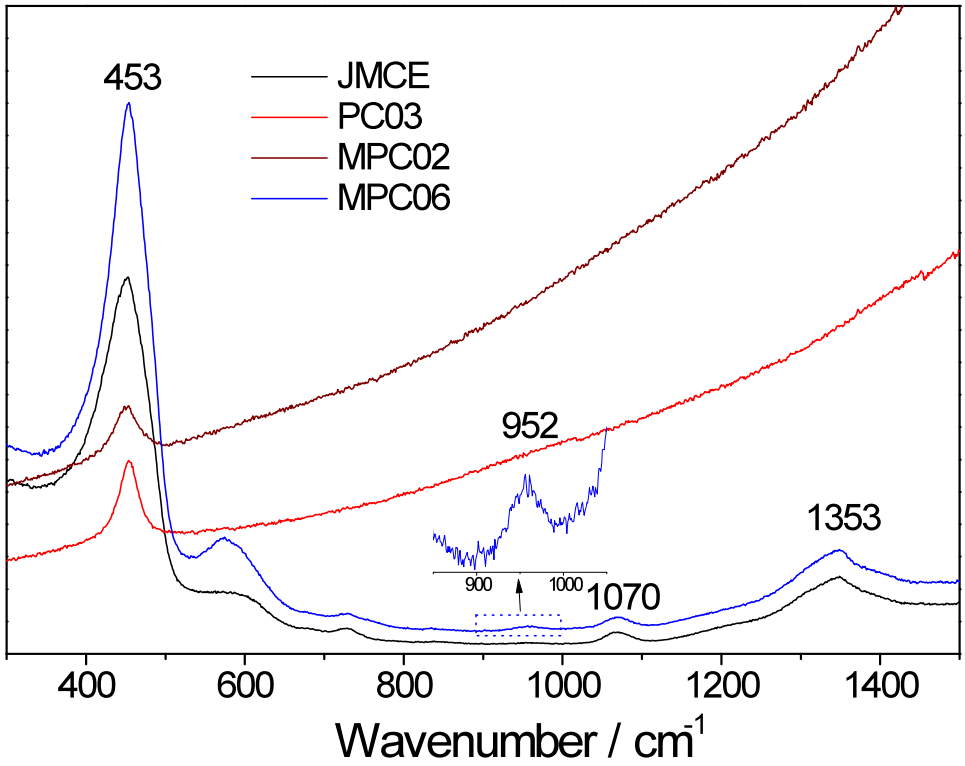

Figure 5.7 Raman spectra of the commercial ceria sample and Pt doped ceria samples prepared using different synthesis methods.

Fluorite structure metal oxides only have a single allowed Raman mode, which has F_{2g} symmetry and which can be viewed as a symmetric breathing mode of the O atoms around each cation. Since only the oxygen atoms move, the mode frequency should be nearly independent of the cation mass [30]. In the ceria, this frequency was reported between 453 and 454 cm^{-1} attributed to a symmetrical stretching mode of Ce-O8 vibrational unit. It is found in the JMCE sample (nano ceria bought from Johnson Matthey), there is a strong Raman peak at 453 cm^{-1}, which is attributed to the CeO_2 F_{2g} mode [30].

In the PC03 and MPC02, the intensity of the peak at 453 cm^{-1} is much weaker, and other peaks also disappear or buried in a broad background. It may be due to the fact

that the black Pt nanoparticles adsorb substantially the visible light region and make the Raman signal from the surface of samples much weaker.

In the MPC06, the intensity of the major peaks at 453 cm^{-1} (CeO_2 F_{2g}) and the shoulder peak at 580 cm^{-1} are however both very strong, the peaks at 1070 and 1353 cm^{-1} are also observed. It is interesting to note a new peak at 952 cm^{-1} which can be attributed to peroxide species [30].

From the Raman results, there seems to be no major structure difference between the pure ceria, JMCE and MPC06. However, from the TPR results, there was a clear shift in surface oxygen peak of the MPC06 by about 10 degree Celsius lower than the MPC02. This may account for the new Raman peak of the superoxide species observed in the MPC06.

When the core shell Pt in ceria sample was synthesized by co-microemulsion method to there is stronger metal oxide interaction compared with the sample synthesized by the normal microemulsion method (details in Chapter 2), the stronger metal ceria interaction may leads to more oxygen vacancies. Upon oxygen adsorption (air) these oxygen vacancies may supply some new surface oxygen species such as superoxide (as shown in Chapter 4) and peroxide as presently demonstrated [1, 30]. Using formic acid adsorption combined with FTIR spectroscopy can give some useful information on the type of oxygen vacancies created at the interface. Figure 5.8 shows the FTIR profiles of the formic acid adsorbed Pt modified ceria samples.

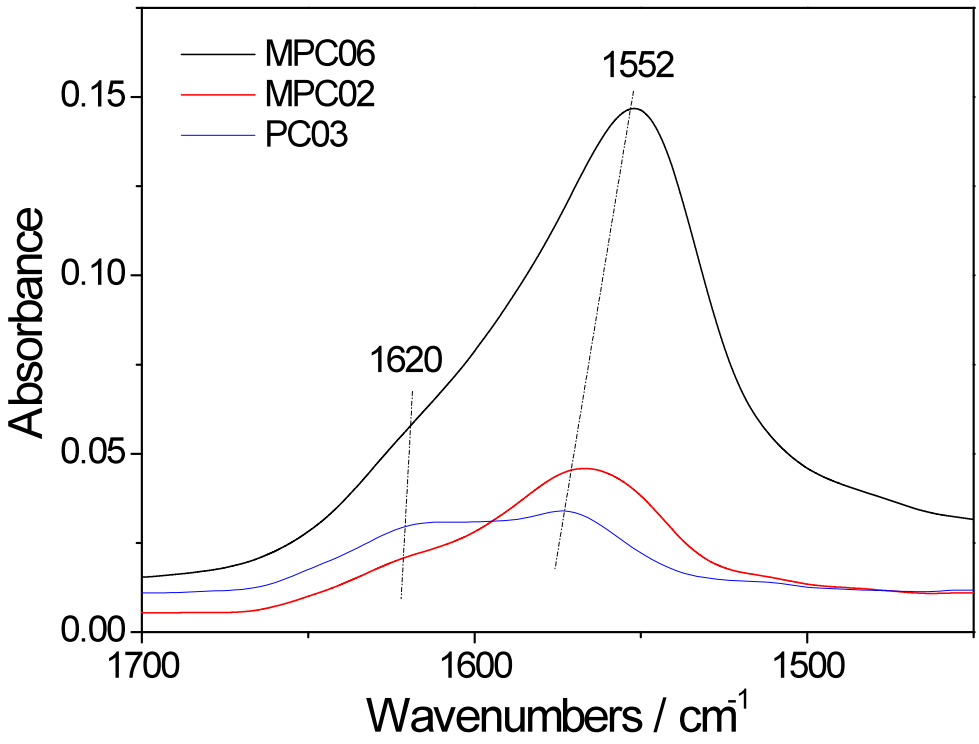

Figure 5.8 FTIR spectra of nano ceria and different Pt doped ceria samples.

It is well known that formic acid can be adsorbed on the surface of ceria to form the formate species and adsorbed hydroxyl species [31]. In our cases, there was no molecularly adsorbed formic acid via hydrogen bonding with the surface because of there was no adsorption at 1720 cm^{-1} [31].

On the other hand, from the Figure 5.8, there are two kinds of formate adsorption peaks observed by the FTIR [31]. The vibrational peak at 1552 cm^{-1} is assigned to asymmetric ν_{as}(OCO) stretching of bidentate formate. The vibration peak at 1620cm^{-1} is assigned to asymmetric ν_{as}(OCO) stretching of monodentate formate. Scheme 5.4 shows the two adsorbed formate species.

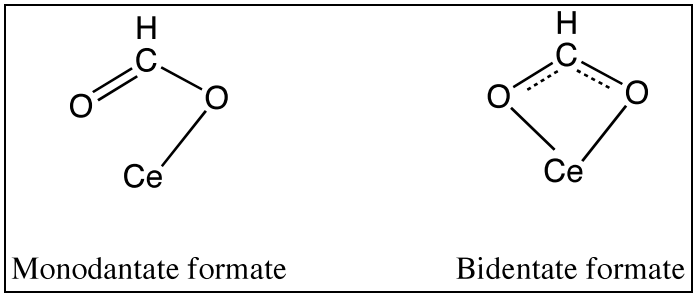

Scheme 5.4 Two possible adsorbed formate species on the surface of ceria [31]

For the JMCE sample, there is no formate adsorption peak detected. For the co-microemulsion MPC06 sample, there is only bidentate formate peak observed. For the microemulsion MPC02 sample, the bidentate adsorbed formate is the major adsorption mode but the peak intensity is much weaker than the MPC06 sample. It is interesting to note that the wet-grinding sample, PC03 (the bottom blue line), the adsorption peaks are very different from the two other samples. The monodentated formate peak becomes the dominant feature in the spectrum.

There are different oxygen vacancies previously identified on the surface of ceria, such as single surface vacancies, linear cluster vacancies and trimer surface vacancies [32]. These different types of surface oxygen vacancies are expected to give rise to different adsorbed formate species. For example, the surface oxygen vacancy clusters (two or more oxygen vacancies as neighbour) may produce bidentate formate on the surface, and the single surface vacancies will likely create monodentated formate species. For the MPC02 and MPC06, with the predominant bidentate formate adsorption peak observed, oxygen vacancies cluster may be prevalent due to enhanced concentration of oxygen vacancies. And for the PC03, there are only single, isolated oxygen vacancies formed on the surface of ceria. So, it is concluded that active oxygen vacancy clusters may be preferentially formed [2, 3] on the surface of ceria at the interface with the metal.

Since we have demonstrated that Pt is capable of improving the oxygen storage capacity of ceria by creating more surface oxygen vacancies (oxygen vacancy clusters) on ceria surface. The next question is: Will there be more superoxide species created in our samples upon air exposure as we previously demonstrated in the case of pure nanosized ceria in Chapter 4?

To answer this question, EPR was used for the further investigation to address this question. The EPR profiles of Pt modified ceria samples are shown in Figure 5.9.

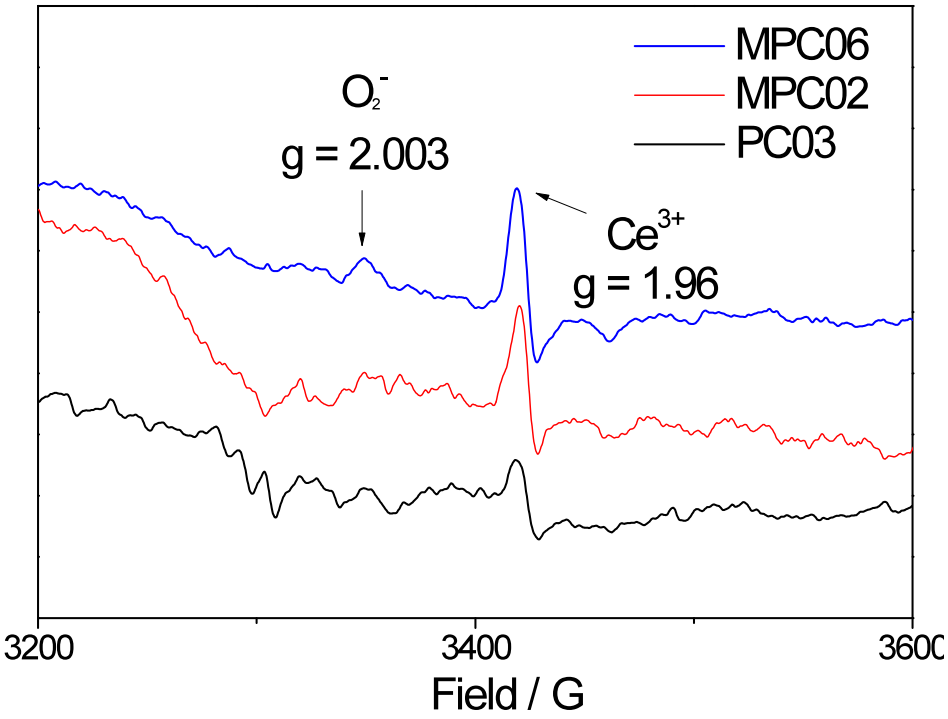

Figure 5.9 EPR spectrum of Pt doped ceria by different methods.

In Figure 5.9, besides the signal contributed to Ce^{3+} (g value = 1.96) [33], another peak with the typical value reported as O_2^- (g value =2.003) [33, 34] can be found. This spectrum is similar to the nano ceria (> 5 nm) shown in the last chapter but the relative intensity of O_2^- is lower than the pure nano ceria of equivalent size. So in the

MPC06, no surplus in the superoxide (O_2^-) is created in the presence of metal. In the MPC02 and PC03, no superoxide peak was observed.

It is concluded that the different synthesis methods can give samples with different metal ceria interactions in Pt/ceria samples. With the stronger metal support interactions, oxygen vacancy clusters may be formed on the surface of ceria from the high concentration of isolated oxygen vacancies, which activate molecular oxygen from air to give peroxide species.

5.3.3 The Effect of Metal Concentration

Another sample, MPC09 was synthesized by the same co-microemulsion method but with less of the Pt precursor as compared with the MPC06.

Figure 5.10 shows the XRD profiles of the two samples synthesized by the same co-microemulsion method: MPC09 is the sample with 0.4 at.-% Pt, and MPC06 is with 1.25 at.-% Pt in ceria.

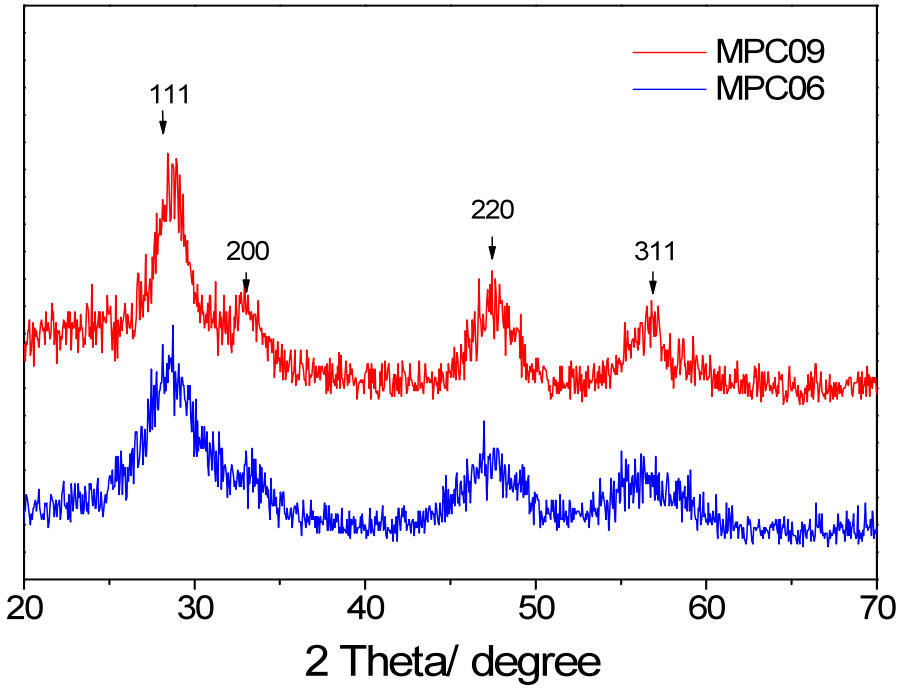

Figure 5.10 XRD profiles of two co-microemulsion modified Pt/ceria samples with different Pt loadings.

In Figure 5.10, the two samples show similar XRD profiles. The diffraction peaks of CeO_2 appear in the two samples, contributing to the 2θ degree 28.6 (111), 33.1 (200), 47.5 (220) and 56.3 (311) peaks. And there is no Pt peak observed in both

samples. From XRD results, it is clear that by doping with different amounts of the Pt precursor, there is still no significant difference in the ceria crystal structure.

Figure 5.11 shows the TPR profiles of the commercial ceria sample JMCE, MPC09 and MPC06 samples.

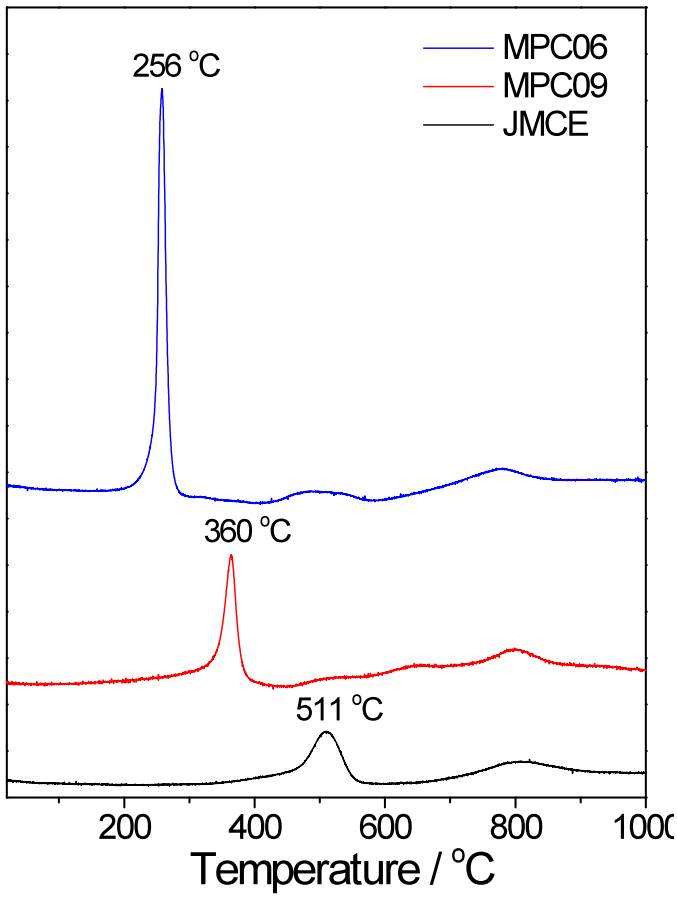

Figure 5.11 H_2-TPR profiles of JMCE and co-microemulsion modified Pt/ceria with different Pt loading amount samples.

From the Figure 5.11, it is clear that as the level of doping Pt decreases, there is a shift in surface reduction oxygen to higher temperature (MPC09). It is obvious that the metal promoted surface oxygen peaks are observed in both the MPC06 and MPC09. Comparing the TPR profile for the 0.4 at-.% Pt/ceria MPC09 sample with

that of the 1.25 at-.% Pt/ceria MPC06 sample, it can be seen that the surface oxygen peak from MPC06 sample is not only shifted to the lower temperature but is much enhanced in size. It implies that in MPC06, the activated oxygen is easier to reduce than in MP09. Table 5.3 shows the calculated quantity of the reducible oxygen of each sample after integrating the optimized peaks in TPR by Gaussian method.

Table 5.3 The oxygen amount calculated by the integration of TPR results.

	$[O]_{tot.}$ (mmol/g)	**Surf oxygen from Pt/ceria interface**			**Surf oxygen of Ceria**			**Bulk oxygen**		
		T1 (^oC)	[O] (mmol/g)	%	T2 (^oC)	[O] (mmol/g)	%	T3 (^oC)	[O] (mmol/g)	%
JMCE	0.681	-	-	-	511	0.394	57.90	810	0.287	42.10
MPC09	0.827	360	0.476	57.62	502	0.096	11.56	798	0.255	30.81
MPC06	1.139	256	0.775	68.06	492	0.11	10.09	776	0.249	21.84

In Table 5.3, the total amount of the reducible oxygen from the MPC09 is 0.827 mmol/g (0.146 mmol/g more than that of the commercial JMCE), and for the MPC06, it is 1.139 mmol/g (0.458 mmol/g more than that of the JMCE). The bulk oxygen contents from the MPC09 and MPC06 are similar to each other (a little smaller than the JMCE). The reduction temperature of the activated surface oxygen of the MPC09 is 360 ^oC (0.476 mmol/g). In contrast, 0.775 mmol/g activated surface oxygen at the reduction temperature of 256^oC is found in the MPC06. It is clear that in ceria with a higher quantity of Pt there will be some extra reducible oxygen created from the sample. It is emphasized that the extra oxygen observed from the TPR results would

not come from reduction of PtO/PtO_2 which only contributes to 1.25 at.% at the maximum.

It is also interesting to find that with the smaller amount of Pt 0.4 at.-% in the MPC09, the reduction temperature of the activated surface oxygen peak is 360 ^{o}C. But in the case of the MPC06 sample with 1.25 at.-% Pt, and the reduction temperature is 256 ^{o}C, almost 100 ^{o}C lower than the MPC09. It is known that the Pt is formed in the core, and we do not know how far the metal interaction can reach to the external ceria layer. When the Pt metal is synthesized from a lower concentration of Pt precursor, the core size is expected to be smaller, so the ceria shell should be thicker, and the influence of the metal oxide interaction could be weakened. Taking into account the fact that there is a degree of size distributions in Pt core and ceria shell, the 0.4 at.-%Pt/ceria sample is therefore expected to give on average poorer metal-ceria interactions than those of 1.25 at.-% Pt/ceria sample.

Figure 5.12 shows the Raman spectra of JMCE and the two co-microemulsion samples, MPC09 and MPC06.

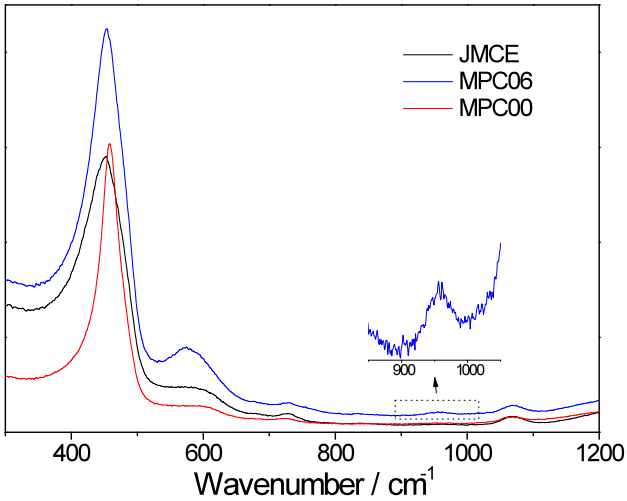

Figure 5.12 Raman spectra of commercial ceria and co-microemulsion modified Pt/ceria samples with different Pt loading amount.

In Figure 5.12, the peak at 453 cm^{-1} attributed to the CeO_2 F_{2g} mode is found in both the MPC09 and MPC06. There is a small peak at 952 cm^{-1} in MPC06, which is attributed to the formation of surface peroxide. As with the JMCE sample, the MPC09 sample shows no signal in the 952 cm^{-1} region. Combining the results of TPR, it is concluded that the smaller Pt amount used in the co-microemulsion method will not be effective in promoting surface oxygen vacancies (later forming superoxide or peroxide species upon molecular oxygen adsorption) since the metal-ceria interaction is rather short range in atomic distance. It is noted that the Raman peak at 580 cm^{-1} is assigned to peroxide species which is derived from oxygen adsorption on the oxygen vacancy in ceria [31]. It is interesting to see how this species is related to the superoxide species on pure nano ceria we identified in Chapter 4.

Figure 5.13 shows the FTIR results of the formic acid adsorption on MPC09 and MPC06, respectively.

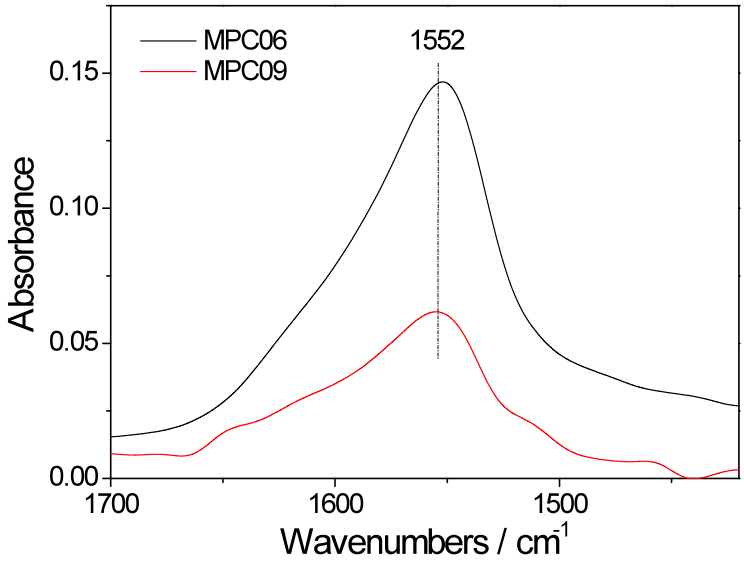

Figure 5.13 FTIR spectra of two co-microemulsion modified Pt/ceria samples of different Pt loadings.

In Figure 5.13, there is only one vibrational peak detected at 1556 cm^{-1}, which is assigned to the asymmetric ν_{as}(OCO) stretching of bidentate formate in both the MPC09 and MPC06 samples. The results indicate that oxygen vacancy cluster may be formed on the surface of co-microemulsion Pt/ceria samples. However, the peak in the MPC09 is much weaker than the MPC06 implying fewer amounts of oxygen vacancy clusters available on the surface of MPC09. The result agrees with this hypothesis.

Thus, for core shell Pt/ceria sample, using the co-microemulsion method can somehow control metal ceria interaction. It is clear that the degree of metal doping in the core will influence the degree of oxygen vacancies formed on the external ceria shell.

5.4 Conclusion

It is shown for the first time that the sol-gel prepared Ni/ceria catalyst shows a much higher selectivity for propanediol (PD) through the C-O cleavages in the glycerol hydrogenolysis reaction. It is proposed that this cleavage reaction occurs on the surface of composite catalyst with the presence of the oxygen vacancies at the interface between ceria and Ni. This clearly suggests that oxygen vacancies around the metal-ceria interface could play an important role in hydrogenolysis reaction.

Different synthesis methods are also attempted to alter the metal-ceria interaction between Pt and ceria, and XRD, EPR, HRTEM, TPR, Raman and FTIR are employed to characterize these samples. With the stronger metal-ceria interactions, it is observed that surface oxygen vacancy clusters are formed. It is also demonstrated that the amount of metal used in the core can affect the quantity of oxygen vacancies formed on ceria shell surface as the metal-ceria interaction diminishes in thicker shells.

5.5 Reference

1. A. Trovarelli, Catalysis by Ceria and Related Materials, Imperial College Press, London, 2002.
2. X. Liu, K. Zhou, L. Wang, B. Wang, Y. Li, Journal of the American Chemical Society, 131 (2009) 3140-3141.
3. J. Xu, J. Harmer, G. Li, T. Chapman, P. Collier, S. Longworth, S.C. Tsang, Chemical Communications, 46 (2010) 1887-1889.
4. M. Sugiura, M. Ozawa, A. Suda, T. Suzuki, T. Kanazawa, Bulletin of the Chemical Society Japan, 78 (2005) 752-767.
5. J. Kaspar, P. Fornasiero, N. Hickey, Catalysis Today, 77 (2003) 419-449.
6. R. Craciun, B. Shereck, R.J. Gorte, Catalysis Letters, 51 (1998), 149-153.
7. R. Farrauto, S. Hwang, L. Shore, W. Ruettinger, J. Lampert, T. Giroux, Y. Liu, O. Ilinich, Annual Review of Materials Research, 33 (2003) 1-27.
8. A. F. Ghenciu, Current Opinion in Solid State and Materials Science, 6 (2002) 389-399.
9. X. S. Liu, W. Ruettinger, X. M. Xu, R. Farrauto, Applied Catalysis B: Environmental, 56 (2005) 69-75.
10. T. Bunluesin, R. J. Gorte, G. W. Graham, Applied Catalysis B: Environmental, 15 (1998) 107-114.
11. S. Hilaire, X. Wang, T. Luo, R. J. Gorte, J. Wagner, Applied Catalysis A: General, 215 (2001) 271-276.
12. C. M. Y. Yeung, S. C. Tsang, The Journal of Physical Chemistry C, 113 (2009) 6074-6087.
13. C. M. Y. Yeung, K. M. K. Yu, Q. J. Fu, D. Thompsett, M. I. Petch, S. C. Tsang,

Journal of the American Chemical Society, 127 (2005) 18010-18011.

14. R. M. Heck, R. J. Farrauto, Applied Catalysis A: General, 221 (2001) 443-457.
15. O. Fu, H. Saltsburg, M. Flytzani-Stephanopoulos, Science 301 (2003) 935-938.
16. K. Foger, In Catalysis: Science and Technology, Vol. 6 (J. R. Anderson and M. Boudart eds.), Springer-Verlag, Berlin, 227, 1984.
17. J. A. Farmer, C. T. Campbell, Science, 329 (2010) 933-936.
18. T. Werpy, B. Peterson, Top Value added chemicals from biomass, US Department of Energy, 2004.
19. C. H. Zhou, J. N. Beltramini, Y. X. Fan, G. Q. Lu, Chemical Society Reviews, 37 (2008) 527-549.
20. C. Montassier, D. Giraud, J. Barbier, Studies in Surface Science and Catalysis, 41 (1988) 165-170.
21. C. Montassier, J. M. Dumas, P. Granger and J. Barbier, Applied Catalysis A: General, 121 (1995) 231-244.
22. C. Montassier, J. C. Ménézo, J. Moukolo, J. Naja, L. C. Hoang, J. Barbier, Journal of Molecular Catalysis, 70 (1991) 99-110.
23. D. K. Sohounloue, C. Montassier, J. Barbier, Reaction Kinetics and Catalysis Letters, 22 (1983) 391-397.
24. E. P. Maris, R. J. Davis, Journal of Catalysis, 249 (2007) 328-337.
25. K. Motokura, M. Tomita, M. Tada, Y. Iwasawa, Chemistry - A European Journal, 14 (2008) 4017-4027.
26. E. S. Vasiliadou, E. Heracleous, I. A. Vasalos, A. A. Lemonidou, Applied Catalysis B: Environmental, 92 (2009) 90-99.
27. C. M. Y. Yeung, S. C. Tsang, Journal of Molecular Catalysis A: Chemical, 322 (2010) 17-25.

28. G. R. Rao, Bulletin of Materiral Science, 22 (1999) 89-94.
29. V. K. Ivanov, F. Yu. Sharikov, O. S. Polezhaeva, Yu. D. Tret'yakov, Doklady Chemistry, 426 (2009) 101–104.
30. R. Q. Long, Y. P. Huang, H. L. Wan, Journal of Raman Spectroscopy, 28 (1997) 29-32.
31. C. Li, K. Domen, K. Maruya, T. Onishi, Journal of Catalysis, 125 (1990) 445-455.
32. F. Esch, S. Fabris, L. Zhou, T. Montini, C. Africh, P. Fornasiero, G. Comelli, R. Rosei, Science, 309 (2005) 752-755.
33. C. Oliva, G. Termignone, F. P. Vatti, L. Forni, A. V. Vishniakov, Journal of Materials Science, 31 (1996) 6333-6338.
34. J. Soria, A. Martinez-Arias, J. C. Conesa, Journal of the Chemical Society-Faraday Transactions, 91 (1995) 1669-1678.

CHAPTER SIX

CONCLUSION

It was demonstrated by our study presented in Chapter 3 that carbon formation under the harsh conditions of methane steam reforming using low water to methane ratios could be significantly attenuated by depositing ceria on the supported Ni catalyst [1]. The core-shell Ni/CeO_2 catalyst was successfully synthesized by the optimised sol-gel method [2,3] using cerium (IV) isopropoxide as the precursor. This catalyst was stable and exhibited a high level of hydrogen production with no significant carbon deposition at the laboratory scale for over 110 h, even with a water to methane ratio as low as 0.25, while the parent Ni catalyst suffered from rapid deactivation under the same conditions. Compared with the industrial conditions with the water to methane ratio 2.5 [4], this improved catalyst could reduce a huge amount of the wasted energy by cutting the use of excess steam.

The degree of carbon inhibition over the Ni catalyst depends critically on the type of deposition method used. The sol-gel method using cerium (IV) isopropoxide appeared to be the most effective method in modifying the catalyst to eliminate or severely reduce the carbon formation during the MSR reaction. Extensive catalyst characterisation indicated that an intimate contact between the Ni and ceria phases must be achieved in order to enhance the beneficial metal-metal oxide interaction. The particle size of the achieved cerium oxide might influence the resistance of the carbon formation on the catalysts as well.

The research about the size dependent oxygen storage capacity of nano-particulate cerium oxide was clearly established. Using the modified microemulsion synthesis method [5], a series of nano ceria with different particles sizes were successfully achieved. It was shown that the lattice expansion was inversely related to the size of nano ceria by a variety of characterization methods [6,7]. However no evidence was found for increasing surface Ce^{3+} and oxygen vacancies on nano ceria particles with

decreasing size; this did not agree with the proposal that the lattice expansion could be attributed to an increase in [Ce^{3+}] with a larger radius in smaller nano ceria from previous reports [8]. The lattice expansion should be attributed, primarily, to the strain of increasing surface energy at smaller size ceria. The formation of surface superoxide species dependent on particle size of ceria was also demonstrated, *for the first time*. This is undoubtedly important in selective oxidation catalysis [9, 10] and is most likely formed through the adsorption of molecular oxygen onto nano ceria at sizes below 5.3 nm. The mechanism for the superoxide formation is not yet known but could be related to a dioxygen interaction with a surface oxygen vacancy or vacancy clusters [11] on a stressed surface where quantum confinement could play a key role.

The study of the hydrogenolysis of glycerol in the presence of heterogeneous Ni catalysts was carried out. Controlling the selectivity of the glycerol hydrogenolysis was a challenging prospect due to the highly similar bond energy of C-C (154 kJ/mol) and C-O (kJ/mol) bonds in glycerol [12-14]. Over Ni catalysts, the cleavage of C-C bonds was proposed to occur majorly through a retro-aldol reaction from the intermediate chemical glyceraldehyde [15] and showed a high selectivity of ethylene glycol as a result. The sol-gel prepared partially covered ceria shell Ni/CeO_2 catalyst showed a much higher selectivity of propanediol by the C-O cleavage pathway from the glyceraldehyde dehydration [15] in the glycerol hydrogenolysis reaction. It was proposed that this reaction was happening at the metal-metal oxide interface of the catalyst aided by the oxygen vacancies on the surface of ceria. It therefore gave evidence that the oxygen vacancies were formed and that surrounding the metal in cerium oxide produced a strong metal-metal oxide interaction.

The core-shell Pt/CeO_2 catalysts with varying of the metal-metal oxide interactions were achieved by various synthetic methods [16, 17]. It was found that with a

stronger metal-metal oxide interaction more surface oxygen vacancies were formed, which led to a higher concentration of active oxygen species on the surface of the catalysts. Also, the doped metal amount was found to affect the formation of the oxygen vacancies.

How to increase the effective oxygen vacancies by tailoring the quantities and types of defect on the surface of cerium oxide is still a major challenge in the understanding and designing of improved ceria related catalysts [18, 19], and more work needs to be done in the future before catalysts can be tailored, from the ground up, to specific applications.

Reference

1. J. Xu, C.M.Y. Yeung, J. Ni, F. Meunier, M. Fowles, S.C. Tsang, Applied Catalysis, A: General, 345 (2008) 119-127.
2. K.M.S. Khalil, L.A. Elkabee, B. Murphy, Microporous and Mesoporous Materials. 78 (2005) 83-89.
3. K.M.S. Khalil, L.A. Elkabee, B. Murphy, Journal of Colloid and Interface Science. 287 (2005) 534-541.
4. A.P.E. York, T.C. Xiao, M.L.H. Green, J.B. Claridge, Catalysis Reviews, 49 (2007) 511-560.
5. T. Masui, K. Fujiwara, K. Machida, G. Adachi, T. Sakata, H. Mori, Chemistry of Materials, 9 (1997) 2197-2204.
6. X. D. Zhou, W. Huebner, Applied Physics Letters, 79 (2001) 3512-3514.
7. M.D. Hernández-Alonso, A.B. Hungría, A. Martínez-Arias, J.M. Coronado, J.C. Conesa, J. Soria, M. Fernández-García, Physical Chemistry Chemical Physics, 6 (2004) 3524-3529.
8. S. Deshpande, S. Patil, S. V. Kuchibhatla, S. Seal, Applied Physics Letters, 87 (2005) 133113.
9. A.Trovarelli, Catalysis by ceria and related materials; Imperial College Press: London, 2002.
10. M. Y. Yeung, K. M. K. Yu, Q. J. Fu, D. Thompsett, M. I. Petch, S. C. Tsang, Journal of the American Chemical Society, 127 (2005) 18010-18011.
11. F. Esch, S. Fabris, L. Zhou, T. Montini, C. Africh, P. Fornasiero, G. Comelli, R. Rosei, Science, 309 (2005) 752-755.

12. C. Montassier, D. Giraud, J. Barbier, Studies in Surface Science and Catalysis, 41 (1988) 165-170.
13. C. Montassier, J. M. Dumas, P. Granger and J. Barbier, Applied Catalysis A: General, 121 (1995) 231-244.
14. C. Montassier, J. C. Ménézo, J. Moukolo, J. Naja, L. C. Hoang, J. Barbier, Journal of Molecular Catalysis, 70 (1991) 99-110.
15. E. P. Maris, R. J. Davis, Journal of Catalysis, 249 (2007) 328-337.
16. C.M.Y. Yeung, S.C. Tsang, Journal of Molecular Catalysis A: Chemical, 322 (2010) 17-25.
17. C. M. Y. Yeung, S. C. Tsang, The Journal of Physical Chemistry C, 113 (2009) 6074-6087.
18. X. Liu, K. Zhou, L. Wang, B. Wang, Y. Li, Journal of the American Chemical Society, 131 (2009) 3140-3141.
19. J. Xu, J. Harmer, G. Li, T. Chapman, P. Collier, S. Longworth, S.C. Tsang, Chemical Communications, 46 (2010) 1887-1889.